MESOSCALE THERMO-MECHANICAL RESPONSE OF TRADITIONALLY AND ADDITIVELY MANUFACTURED ENERGETIC MATERIALS TO DYNAMIC LOADING

A Dissertation
Presented to
The Academic Faculty

by

Amirreza Keyhani

In Partial Fulfillment
of the Requirements for the Degree
Doctor of Philosophy in the
School of Mechanical Engineering

Georgia Institute of Technology
August 2020

MESOSCALE THERMO-MECHANICAL RESPONSE OF TRADITIONALLY AND ADDITIVELY MANUFACTURED ENERGETIC MATERIALS TO DYNAMIC LOADING

Approved by:

Dr. Min Zhou, Advisor
School of Mechanical Engineering
Georgia Institute of Technology

Dr. Shuman Xia
School of Mechanical Engineering
Georgia Institute of Technology

Dr. Richard Neu
School of Mechanical Engineering
Georgia Institute of Technology

Dr. Julian Rimoli
School of Aerospace Engineering
Georgia Institute of Technology

Dr. Antonia Antoniou
School of Mechanical Engineering
Georgia Institute of Technology

Date Approved: July 10, 2020

To my family

ACKNOWLEDGEMENTS

I would like to thank my advisor, Dr. Min Zhou, for guiding and supporting me on my path through graduate school. I also would like to thank the members of my thesis committee: Dr. Richard Neu, Dr. Antonia Antoniou, Dr. Shuman Xia, and Dr. Julian Rimoli for their comments and suggestions.

I would like to thank my friends and lab mates, including Dr. Seokpum Kim, Dr. Ushasi Roy, Dr. Christopher Miller, Daniel Olsen, Yaochi Wei, Jay Shin, and Chris Coffelt for their encouragement and support.

Above all, I would especially like to thank my mother, Shokouh, my father, Nasser, my sister, Nazi, and my brothers, Alireza and Hamid for their unconditional love and support.

TABLE OF CONTENTS

LIST OF TABLES

LIST OF FIGURES

LIST OF SYMBOLS AND ABBREVIATIONS

Symbols

$\hat{\boldsymbol{\tau}}$	Jaumann rate of the Kirchhoff stress
L	Elastic moduli tensor
$\boldsymbol{\sigma}$	Cauchy stress tensor
K	Bulk modulus
ε	Eulerian strain tensor
ε^D	Deviatoric component of ε
ε^H	Hydrostatic component of ε
t	Time
τ	Reduced time in generalized Maxwell model
G	Shear modulus
T_0	Reference temperature
G_∞	Steady-state shear modulus
g_i	Relative shear modulus of the i-th term
N_p	Number of terms in Prony series

τ_i^p Relaxation times

$\mathbf{F}$ Deformation gradient

$\mathbf{F}^e$ Elastic part of $\mathbf{F}$

$\mathbf{F}^p$ Plastic part of $\mathbf{F}$

$\mathbf{D}$ Rate of deformation

$\mathbf{D}^e$ Elastic part of $\mathbf{D}$

$\mathbf{D}^p$ Plastic part of $\mathbf{D}$

$\mathbf{\Omega}$ Spin tensor

$\mathbf{\Omega}^e$ Elastic part of $\mathbf{\Omega}$

$\mathbf{\Omega}^p$ Plastic part of $\mathbf{\Omega}$

E Young's Modulus

υ Poisson's ratio

$\mathbf{I}$ Second-order identity tensor

$\mathbf{I}'$ Fourth-order identity tensor

ε_0 Reference strain

$\dot{\bar{\varepsilon}}$ Equivalent plastic strain rate

β, κ	Thermal softening parameters
$\dot{\bar{\varepsilon}}_0, \dot{\bar{\varepsilon}}_m$	Reference strain rates
a, m	Rate sensitivity parameters
τ_h	Hydrostatic part of Kirchhoff stress
p	Pressure
J	Jacobian
e	Emissivity
T_s	Sample temperature
T_c	Camera's temperature reading
σ	Stefan-Boltzmann constant
L_0	Initial length of sample
L	Instantaneous length of sample
ΔL	$L - L_0$
$\bar{d}_0$	Initial size of grains
ρ	Mass density
ρ_0	Initial mass density

σ_e	Von Mises equivalent stress
σ_H	Hydrostatic stress
β	Friction angle of the material in the meridional stress plane
σ_c	Yield stress in compression
σ_t	Yield stress in tension
Γ_0	Grüneisen's gamma at reference state
E_m	Internal energy per unit mass
U_s	Shock velocity
U_p	Particle velocity
c_0, s	Constants in $U_s - U_p$ linear relationship
$\bar{\varepsilon}_D^{pl}$	Equivalent plastic strain at onset of damage
$\bar{\varepsilon}_f^{pl}$	Equivalent plastic strain at failure
δ_f	Equivalent displacement at failure
L_E	Cube-root of element volume
μ	Coefficient of friction

σ_n Normal stress

v_{rel} Relative sliding velocity

W_p Plastic dissipation

W_f Frictional dissipation

W_D Damage dissipation

Abbreviations

AM	Additive Manufacturing
AMEM	Additively Manufactured Energetic Material
APS	Advanced Photon Source
CFEM	Cohesive Finite Element Method
CODEX	Cohesive Dynamics for Explosives
DCS	Dynamic Compression Sector
DIC	Digital Image Correlation
DIW	Direct Ink Writing
EOS	Equation of State
FOV	Field of View
FPS	Frame per Second
GMM	Generalized Maxwell Model
HMX	Octahydro-1,3,5,7-tetranitro-1,3,5,7-tetrazocine
ICCD	Intensified Charge Couple Device
IR	Infrared

KBA	Kolsky Bar Apparatus
LSO	Lutetium Oxyorthosilicate
MINTED	Microscale In-situ Imaging of Dynamic Temperature and Deformation Fields
MSAC	M-estimator Sample Consensus
OHFC	Oxygen-free High Thermal Conductivity
PBX	Polymer-Bonded Explosive
PCI	Phase Contrast Imaging
SEM	Scanning Electron Microscopy
SHPB	Split-Hopkinson Pressure Bar
SURF	Sped up Robust Features
TSHB	Torsional Split-Hopkinson Bar
UV	Ultraviolet
VL	Visible Light
µCT	Micro-computing Tomography

SUMMARY

The thermo-mechanical responses of traditionally manufactured polymer-bonded explosives (PBXs) and an additively manufactured energetic material (AMEM) simulant under dynamic loading are studied. The performance of energetic materials subjected to dynamic loading significantly depends on their micro- and meso-scale structural morphology. The geometric versatility offered by additive manufacturing opens new pathways to tailor the performance of these materials. Additively manufactured energetic materials (AMEMs) have a wide range of structural characteristics with a hierarchy of length scales and process-inherent heterogeneities which are hitherto difficult to precisely control. Therefore, it is essential to understand how these features affect AMEMs' response under dynamic/shock in order to tailor these materials for applications, improve performance, and minimize uncertainties.

To analyze the thermo-mechanical response and ignition behavior of PBXs, a cohesive finite element framework is used. The framework explicitly accounts for finite-strain elastic-viscoplastic deformation, arbitrary crack initiation and propagation, contact between internal surfaces, post-contact friction, heat generation resulting from inelastic bulk deformation and friction, and heat conduction. The analyses focus on material behavior at various levels of constituent friction and plasticity, and load intensity. The time to ignition is analyzed and quantified, providing explicit expressions for the ignition probability as a function of load intensity, load duration, and constituent properties.

The AMEM simulant analyzed is unidirectionally printed using direct ink writing (DIW) of a high solid-loaded photopolymer and cured under UV-light exposure. To study the thermo-mechanical response of the AMEM simulant, quasi-static mechanical tests, intermediate strain rate Split-Hopkinson pressure bar (SHPB) experiments integrated with simultaneous high-speed visible and thermal imaging, and high strain rate x-ray phase-contrast imaging (PCI) experiments are performed. The experiments capture deformation modes and corresponding temperature signatures in the AMEM simulant. However, the effects of microstructural attributes and energy dissipation cannot be quantified experimentally due to limitations of available diagnostics. Therefore, experimentally-informed finite element computations are also performed to gain the quantification. The microstructural attributes are found to significantly affect the development of the hotspots in the AMEM simulant. The computations establish trends in and quantification of the relations between structure and response of a class of additively manufactured photopolymer-particulate composites.

CHAPTER 1. INTRODUCTION

1.1 Background and Motivation

The thermo-mechanical response of heterogeneous materials under dynamic loading is of great importance in many applications. Dynamic loading events can cause severe damage and energy dissipation, leading to the formation of temperature spikes in a wide range of materials, including, e.g., metals [1-4], polymers [5], composites [6], ceramics [7], shape memory alloys (SMAs) [8, 9], and energetic materials [10, 11]. One class of temperature spikes are referred to as hotspots, and can cause thermal softening, thermal runaway, or even the onset of chemical reactions in energetic materials [12]. Local failure and formation of temperature spikes result from several factors, such as strain localization due to heterogeneity in the microstructure, material property mismatch between constituents, and the existence of defects such as voids, cracks and inclusions. Field et al. [10, 11] provided evidence for the mechanisms contributing to the formation of hotspots. Subsequently, computational and experimental approaches have been widely used to study mechanisms responsible for heat generation in heterogeneous materials.

Specifically for energetic materials, computational studies have enhanced understanding of heating mechanisms. However, these studies are limited in terms of the resolution of fine-scale physics and require experimental data for calibration and validation. On the other hand, experiments have provided insights into underlying heating mechanisms. For example, it is known that inelasticity [13, 14], void collapse, inter-particle contact, and internal fracture and friction [15, 16] are dominant heating mechanisms in energetic materials and other heterogeneous materials. However, experiments have not

allowed full understanding and detailed quantification of the underlying mechanisms primarily due to the lack of abilities to directly measure, in time- and space-resolved manner, the thermal and mechanical fields at the microstructural level for dynamic conditions. Although several experimental studies [10, 11, 13-17] have focused on mechanisms responsible for the ignition of EM and further computational studies [18-24] have enhanced understanding of ignition, the contributions of different heating mechanisms and their evolution are not well-understood.

1.2 Additive Manufacturing of Energetic Materials: Opportunities and Challenges

Additive manufacturing (AM) involves the successive building of a 3D structure, layer by layer, to achieve the final shape. The process contrasts with traditional manufacturing methods, which generally involve material removal from a built block. Additive manufacturing technologies have led to mature processes for a wide range of materials, such as metals [25, 26], polymers [27], and energetic materials [28, 29]. Various AM methods have recently been used to 3D-print energetic materials. Electrospray deposition has been shown as a viable technique to deposit thin films of thermites [30, 31]. Studies with electrospray techniques have incorporated a polymer binder to impart mechanical integrity to energetic materials while maintaining significant reactivity [32]. Direct ink writing (DIW) methods have demonstrated the ability to deposit energetics with complex sub-millimeter features [33-35]. DIW provides an affordable, flexible way to additively produce 3D objects by extruding custom-tailored inks through a nozzle via extrusion onto a computerized translation stage under constant displacement or constant-pressure [36, 37].

Ultraviolet (UV) laser light curable photopolymers are widely used in DIW. Photopolymers are light-sensitive monomers that crosslink and solidify when exposed to light of specific wavelengths. Photopolymers provide lower viscosity for easier printing processes and fast curing reactions, which are suitable for 3D printing of energetic materials. However, the application of 3D-printed photopolymers is limited to secondary structural parts due to their poor mechanical behavior [38, 39]. DIW is capable of printing high-solids loaded precursor materials with high viscosities as demonstrated by McClain et al. [40], who printed ammonium perchlorate composites at 85% solids loading by volume with less porosity than the cast method. Additionally, the filament sizes can range from sub-micrometers to millimeters, allowing for tailored structures with fine features [41].

A consequence of the layer-by-layer build in DIW additive manufacturing, is the generation of process-inherent heterogeneities which can cause mechanical properties to differ significantly in different orientations and regions, as well as between builds [42, 43]. Mueller et al. [44] studied anisotropic detonation behavior by introducing ordered linear porosity in structured UV-cured direct-ink-written energetic materials. In addition to the anisotropy, defects are unavoidable sources of microstructural heterogeneities in AM materials, and can play an important role in determining their overall behavior. O'Grady et al. [45] determined the importance of geometry and size of defects on detonation front in DIW energetic materials subjected to impact loading.

1.3 Objectives and Thesis Outline

The main goals of this dissertation are to investigate the thermo-mechanical response of traditionally-manufactured polymer-bonded explosives (PBXs) and an additively-manufactured energetic material (AMEM) simulant as a function of their microstructure attributes and structure to enable the structure-property-performance mapping for the design of energetic materials. In essence, this dissertation addresses the following two fundamental questions:

1. For traditionally-manufactured PBXs, while it is known that viscoplasticity [13, 14], viscoelasticity, and internal fracture and friction [15, 16] all play important roles, there is still significant uncertainty as to which mechanisms dominate in different stages of deformation. At a given load intensity, how do the effects of plasticity and friction evolve? As load intensity increases or as loading transitions from non-shock to shock, does the influence of friction or plasticity increase or decrease?
2. In AMEMs, what fundamental mechanisms govern the correlation between heterogeneous structure and thermo-mechanical response? When do the spatial scale, form, and extent of heterogeneities cease to influence the thermo-mechanical responses of additively manufactured energetic materials, and what ranges are amenable to their tailoring via process control?

This dissertation consists of seven chapters. Chapter 1 provides a background on the topic of thermo-mechanical response of energetic materials, challenges and opportunities of additive manufacturing of energetic materials, and the layout of this

dissertation. Chapter 2 involves a systematic computational analysis of energy dissipation in traditionally manufactured polymer-bonded explosives (PBXs). Computations are performed using a Lagrangian cohesive finite element model (CFEM) [20, 46].

Chapter 3 reports the development of a novel capability for simultaneous time- and space-resolved recording of both fields over the same microstructure area of a sample with micron-level spatial resolutions and microsecond time resolutions. Referred to as **MINTED** (**M**icroscale **In**-situ Imaging of Dynamic **Te**mperature and **D**eformation Fields), the system cohesively integrates a high-speed visible light (VL) camera and a state-of-the-art high-speed infrared (IR) camera via a custom-designed dichroic beam splitter-lens assembly. The combined VL and IR images allow the deformation fields to be obtained through digital image correlation (DIC) and the temperature fields over the same area to be obtained through pixel-level calibration of the differing emissivities of heterogeneous constituents in microstructures. The method integrates the two cameras in a split-Hopkinson pressure bar (SHPB) or Kolsky bar apparatus. This is a general capability that can be used to study deformation, failure and heating in a range of materials, including metals, composites, ceramics, soft materials, and energetic materials.

Chapter 4 studies the mesoscale thermo-mechanical behavior of the additively manufactured energetic material (AMEM) simulant under intermediate strain rate loading. Experiments and multi-physics computations are performed to relate localized deformation, dissipation mechanisms, and temperature rises to the print structure. Simultaneous high-speed optical and infrared imaging (MINTED) is used to obtain deformation and temperature fields over the same area of samples with micrometer spatial and microsecond temporal resolutions. Loading along different directions relative to the

print structure of the material is achieved using a split-Hopkinson pressure bar (SHPB) or Kolsky bar at the average strain rate of 300 s^{-1}. An experimentally-informed Lagrangian finite element framework is developed, accounting for finite-strain elastic-plastic deformation, strain-rate effect, failure initiation and propagation, post-failure internal contact and friction, heat generation due to friction and inelastic bulk deformation, and heat conduction. Using this computational framework, Chapter 5 further quantifies the effects of microstructure attributes including anisotropy, defects, and filament size on localized deformation, energy dissipations, and temperature rises.

Chapter 6 analyzes the shock compression response of an AMEM simulant loaded under several impact conditions and orientations. X-ray phase-contrast imaging (PCI) is used to track features across the observed shock front and quantify the interior deformation fields via digital image correlation (DIC) analyses.

Lastly, Chapter 7 summaries the methodology and the results presented in Chapters 2-6 and provides recommendations for future work.

CHAPTER 2. ENERGY DISSIPATION IN POLYMER-BONDED EXPLOSIVES

This chapter is based on the work published in Ref. [47].

2.1 Introduction

The ignition of energetic materials (EM) under dynamic loading is mainly controlled by localized temperature spikes known as hotspots. Hotspots occur due to several dissipation mechanisms, including viscoplasticity, viscoelasticity, and internal friction along crack surfaces. To analyze the contributions of these mechanisms, this chapter quantifies the ignition probability, energy dissipation, damage evolution, and hotspot characteristics of polymer-bonded explosives (PBXs) with various levels of constituent plasticity of the energetic phase and internal crack face friction. Using PBX9501 consisting of HMX (Octahydro-1,3,5,7-Tetranitro-1,2,3,5-Tetrazocine) and Estane as a reference material, this chapter analyzes variants of this material with several values of the yield stress of the energetic phase and coefficients of internal crack face friction, while other parameters are kept unchanged.

The contributions of dissipation mechanisms to the ignition of EM are heavily affected by material heterogeneity, constituent properties, bonding between constituents, defects, and loading (e.g., impact velocity). A systematic computational study is performed to quantify the contributions of some of the dominant dissipation mechanisms, including fracture, friction, and plastic deformation in a polymer-bounded explosive (PBX) system. The analysis focuses on heat generation in microstructures, damage evolution, and hotspot

characteristics. In particular, the size, temperature, location, and rate of development of hotspots are of interest. The framework developed by Barua et al. [19-21] is used, so factors considered include finite-strain elastic-viscoplastic deformation of grains, viscoelastic deformation of the binder, arbitrary crack initiation and propagation in grains and the binder, debonding between grains and the binder, contact between internal surfaces, friction and frictional heating along internal surfaces, heat generation from inelastic bulk deformation, and the conduction of heat.

The materials are made up of HMX (Octahydro-1,3,5,7-tetranitro-1,3,5,7-tetrazocine) energetic grains and Estane polymer binder. The parametric study involves systematically varying the yield stress of the HMX phase and the coefficients of friction for HMX grains, the Estane binder, and HMX/Estane interfaces. The impact loading is effected by imposing piston velocities between 200 and 1,200 m/s. To determine the ignition status of the material or the "go" or "no-go" state, a criterion based on a criticality threshold obtained from chemical kinetics calculations is used [12]. This criterion, which focuses on the hotspot size and the temperature state, determines criticality. For the PBX materials with various levels of HMX plasticity and material friction, this chapter quantifies the probability of ignition as a function of the time duration of loading, the evolution of dissipation due to viscoplasticity and friction, the density of cracks, and the locations of cracks. Finally, the computationally predicted ignition sensitivity and threshold are expressed in a load intensity-load duration relation, providing a form for comparison with experimentally measurable quantities. Details of the overall framework and approach can be found in recent publications [19-21] and therefore are not repeated here.

2.2 Framework of Analysis

2.2.1 Material and Microstructure

Microstructures used consist of HMX energetic grains and Estane binder, mimicking the attributes of PBX9501. Since simulations of PBX microstructures generated using the Voronoi tessellation yield more realistic results than idealized circular shapes of grains [48], a set of twenty statistically similar microstructure instantiations is generated using the Voronoi tessellation method [19, 48] and this set is used for all combinations of loading (piston velocity) and constituent properties. Although PBX9501 theoretically is made up of ~95% HMX and ~5% binder by volume, binder volume fractions in real samples of this material are actually 23%-26% [49, 50]. This is due to the so-called "dirty binder" effect. Basically, very small HMX particles are absorbed in the binder during preparation, leaving the HMX grains with volume fractions on the order of approximately 74-77%. Therefore, microstructures with an HMX grain volume fraction of 70% and a binder volume fraction of 30% are computationally generated. The average grain size of microstructures is $224.7\ \mu m$. Figure 1(a) shows five out of the twenty microstructures in the sample set. The random variations in microstructure morphology among the samples can be clearly seen. Figure 1(b) shows the size distribution of the HMX grains in the microstructure set, the error bars indicate the range of variations among the samples in the set.

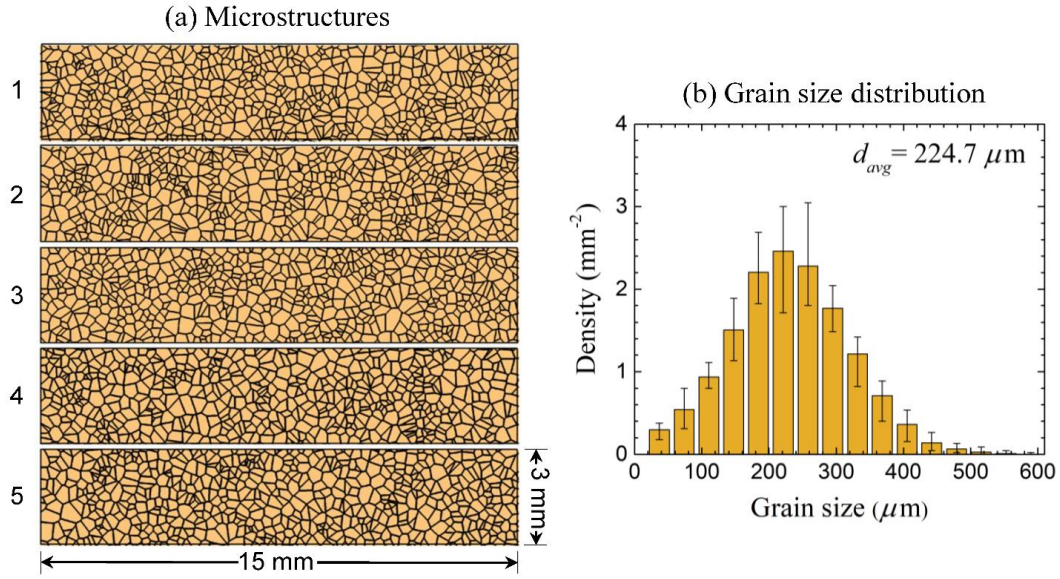

Figure 1 – (a) Five out of twenty computationally generated microstructures with a grain volume fraction of 70%, and (b) size distributions of HMX grains.

In this chapter, the reference material is PBX9501 with viscoplastic HMX grains with the yield stress value of $\sigma_0 = 260$ MPa. The coefficients of friction for crack faces in the HMX grains, Estane binder, and HMX/Estane interfaces are $\mu = 0.5$. Using these as baseline reference material properties, variants of this material with other four levels of yield stress for HMX grains and two levels of coefficient of internal crack face friction are analyzed. For sample sets with HMX grain yield stress values lower than 195 MPa, more than 25% of the microstructures do not reach criticality in the analysis timeframe of 5.5 μs (see Section 2.3.5). Therefore, $\sigma_0 = 195$ MPa is selected as the minimum value of yield stress analyzed. On the other hand, samples with yield stress values higher than 520 MPa behave similar to samples with hyperelastic HMX grains; therefore, $\sigma_0 = 520$ MPa is chosen as the maximum value of yield stress analyzed. With these maximum and minimum values for the yield stress, this chapter analyzes the variants of the reference material

PBX9501 $(\sigma_0 = 260$ MPa, $\mu = 0.5)$ [51] using hyperelastic and viscoplastic models for the HMX grains, the latter of which involves yield stress values of 195, 390, and 520 MPa. For the reference material, another two sample sets with coefficient of friction values of $\mu = 0.25$ and $\mu = 0.75$ are also analyzed. The range of 0.25-0.75 is chosen for the coefficient of friction based on the work of Green et al. [52] who experimentally estimated the magnitude of the coefficient of friction for an HMX based PBX to be between 0.3-0.7. Other studies also showed that the coefficient of friction levels in the considered range of 0.25-0.75. For example, the coefficient of friction for PBX9501 is between 0.35-0.5, according to Dickson et al. [53]. In total, seven material property sets are analyzed. In the following figures, the results corresponding to those of the viscoplastic model for HMX grains are referred to by the value of the yield stress (σ_0), and the results corresponding to viscoplastic HMX grains with $\sigma_0 = 260$ MPa but different levels of constituent friction are referred by the value of the coefficient of friction (μ).

2.2.2 Material Behavior

The Lagrangian cohesive finite element framework [20] used entails explicit account of microstructure, constitutive behavior, and interfacial response. While it has the advantage of tracking fracture and internal friction, the Lagrangian CFEM framework is not as attractive as Eulerian methods [54-59] for explicit resolution of voids.

2.2.3 Estane Binder Constitutive Model

The constitutive response of the Estane binder is modeled via viscoelastic constitutive relations based on the generalized Maxwell model (GMM) [60],

$$\boldsymbol{\sigma}(t) = \int_0^t 2G(\tau - \tau') \frac{\partial \boldsymbol{\varepsilon}^D}{\partial \tau'} d\tau' + \int_0^t K(\tau - \tau') \frac{\partial \boldsymbol{\varepsilon}^H}{\partial \tau'} d\tau'. \tag{1}$$

Here, $\boldsymbol{\sigma}$ is the Cauchy stress, constant K is the bulk modulus, $\boldsymbol{\varepsilon}^D$ and $\boldsymbol{\varepsilon}^H$ are the deviatoric and hydrostatic components of the Eulerian strain tensor, and t and τ are the physical and reduced times, respectively. The following Prony series is used to account for variations of the shear modulus G with the reduced time τ,

$$G(\tau) = G_\infty + \sum_{i=1}^{N_p} G_i e^{-\frac{\tau}{\tau_i^p}} = G_0 \left(g_\infty + \sum_{i=1}^{N_p} g_i e^{-\frac{\tau}{\tau_i^p}} \right), \tag{2}$$

where $G_0 = G_\infty + \sum_{i=1}^{N_p} G_i$ is the instantaneous shear modulus at reference temperature T_0, G_∞ is the steady-state shear modulus, and $g_i = G_i / G_0$ is the relative modulus of the i-th term. N_p is the number of terms in the Prony series and τ_i^p are the relaxation times. Reference [20] provides the parameters and calibration techniques used for modelling the Estane binder.

2.2.4 Constitutive Model for HMX Grains

A brief review of constitutive relations for HMX grains is presented below, and more details can be found in Refs. [20] and [61]. The basic kinematic assumption for the elastic-plastic deformation is

$$\mathbf{F} = \mathbf{F}^e \cdot \mathbf{F}^p, \tag{3}$$

where $\mathbf{F}^e$ and $\mathbf{F}^p$ are the elastic and plastic parts of the deformation gradient $\mathbf{F}$, respectively. The rate of deformation, $\mathbf{D}$, and the spin tensor, $\mathbf{\Omega}$, can be decomposed into elastic and plastic parts according to

$$\begin{aligned} \mathbf{D} &= \mathbf{D}^e + \mathbf{D}^p + \mathbf{D}^t, \text{ and} \\ \mathbf{\Omega} &= \mathbf{\Omega}^e + \mathbf{\Omega}^p. \end{aligned} \tag{4}$$

Thermo-elastic coupling is ignored under the assumption of small elastic strains and independence of the elastic moduli on temperature. Consequently, the Jaumann rate of the Kirchhoff stress, $\hat{\boldsymbol{\tau}}$, can be cast in the form of

$$\hat{\boldsymbol{\tau}} = \mathbf{L} : \left(\mathbf{D} - \mathbf{D}^p \right), \tag{5}$$

where $\mathbf{L}$ refers to the tensor of elastic moduli

$$\mathbf{L} = \frac{E}{1+\upsilon} \left[\mathbf{I}' + \frac{\upsilon}{1-2\upsilon} \mathbf{I} \otimes \mathbf{I} \right], \tag{6}$$

in which "$\otimes$" denotes the tensor product of two vectors, E and υ denote the Young's modulus and the Poisson's ratio, and $\mathbf{I}$ and $\mathbf{I}'$ refer to second- and fourth-order identity tensors, respectively. For an isotropically hardening, viscoplastic solid

$$\mathbf{D}^p = \frac{3\dot{\bar{\varepsilon}}}{2\bar{\sigma}} \boldsymbol{\tau}', \tag{7}$$

where $\dot{\bar{\varepsilon}}$ is the equivalent plastic strain rate and

$$\boldsymbol{\tau}' = \boldsymbol{\tau} - \frac{1}{3}(\boldsymbol{\tau} : \mathbf{I})\mathbf{I},\ \bar{\sigma}^2 = \frac{3}{2}\boldsymbol{\tau}' : \boldsymbol{\tau}'. \tag{8}$$

Here, $\boldsymbol{\tau}'$ and $\bar{\sigma}$ represent the deviatoric portion of the Kirchhoff stress and the Mises equivalent stress, respectively. The equivalent plastic strain rate $\dot{\bar{\varepsilon}}$ is expressed in the form of

$$\left.\begin{aligned}
&\dot{\bar{\varepsilon}} = \frac{\dot{\bar{\varepsilon}}_1 \dot{\bar{\varepsilon}}_2}{\dot{\bar{\varepsilon}}_1 + \dot{\bar{\varepsilon}}_2}, \\
&\dot{\bar{\varepsilon}}_1 = \dot{\bar{\varepsilon}}_0 \left[\frac{\bar{\sigma}}{g(\bar{\varepsilon}, T)}\right]^m, \\
&\dot{\bar{\varepsilon}}_2 = \dot{\bar{\varepsilon}}_m \exp\left[-a\, g(\bar{\varepsilon}, T)\right], \\
&g(\bar{\varepsilon}, T) = \sigma_0 \left(1 + \frac{\bar{\varepsilon}}{\varepsilon_0}\right)^N \left\{1 - \beta\left[\left(\frac{T}{T_0}\right)^\kappa - 1\right]\right\}.
\end{aligned}\right\} \tag{9}$$

In the above relations, $\dot{\bar{\varepsilon}}_0$ and $\dot{\bar{\varepsilon}}_m$ are reference strain rates, *a* and *m* are rate sensitivity parameters for strain rates above 5×10^4 s^{-1} and below 10^3 s^{-1}, respectively, and $\bar{\varepsilon} = \int_0^t \dot{\bar{\varepsilon}}\, dt$ denotes the equivalent plastic strain. Function $g(\bar{\varepsilon}, T)$ describes the quasi-static stress-strain behavior at ambient temperature, where σ_0 refers to the quasi-static yield stress, ε_0 and T_0 present the reference strain and the reference temperature, respectively, *N* denotes the strain hardening exponent, and β and κ are thermal softening parameters. Table 1 provides the values of the parameters for HMX. Reference [61] provides more details about the strain and strain-rate dependence.

Table 1 – Parameters in the viscoplastic constitutive model of HMX.

σ_0 (MPa)	ε_0	N	T_0 (K)	β
260	5.88×10^{-4}	0.0	293	0.0
$\dot{\bar{\varepsilon}}_0$ (s^{-1})	m	$\dot{\bar{\varepsilon}}_m$ (s^{-1})	a ($1/MPa$)	κ
1×10^{-4}	100.0	8.0×10^{12}	22.5	0.0

The third-order Birch–Murnaghan isothermal equation of state (B-M EOS) is used to describe the volumetric behavior, i.e.,

$$\tau_h = -\frac{3}{2}K_0 J\left(J^{-\frac{7}{3}} - J^{-\frac{5}{3}}\right)\left[1+\frac{3}{4}\left(K_0' - 4\right)\left(J^{-\frac{2}{3}} - 1\right)\right], \tag{10}$$

where $\tau_h = \tau_{ii}/3 = \left(\tau_{11}+\tau_{22}+\tau_{33}\right)/3$ is the hydrostatic part of the Kirchhoff stress ($p = -\tau_h$ is the pressure), K_0 denotes the bulk modulus, and $K_0' = \left(\partial K_0/\partial P\right)_{P=0}$. $J = \det(\mathbf{F})$ is the Jacobian. According to Landerville et al. [62], $K_0 = 16.71\,GPa$ and $K_0' = 7.79$.

2.2.5 Cohesive-frictional Interface Constitutive Model

The cohesive finite element method (CFEM) explicitly accounts for arbitrary scenarios of fracture in the samples. In this framework, the cohesive elements inserted between triangular bulk elements follow a bilinear traction-separation law illustrated in Figure 2. Each node of a bulk element is shared by cohesive elements connected to the element, and each edge of a bulk element is connected to an adjacent bulk element edge

through a cohesive element. Before the critical separation of δ_0, separations of a cohesive surface pair are completely recoverable, and partial damage occurs beyond this critical point. Complete separation with no further cohesive strength occurs if the separation surpasses δ_c [63]. Table 2 lists the cohesive parameter values for the interface types in the material considered. At each time step, the entire microstructure is scanned to identify potential interpenetration of all possible contact pairs. A penalty force algorithm is used to strongly discourage/prevent interpenetration and maintain proper contact. Reference [61] provides in depth descriptions of the multi-step contact algorithm. To evaluate frictional heating along and determine the stick-slip states of the sliding surfaces, the Coulomb friction law is used. Table 3 lists the friction coefficients for the three interface types in the material.

Table 2 – Cohesive parameters.

Interface type	$\delta_0(\mu m)$	$\delta_c(\mu m)$	$S_{max}(MPa)$
Estane-Estane	0.001	10	38.4
HMX-HMX	0.01	5	101
HMX-Estane	0.049	4.62	35

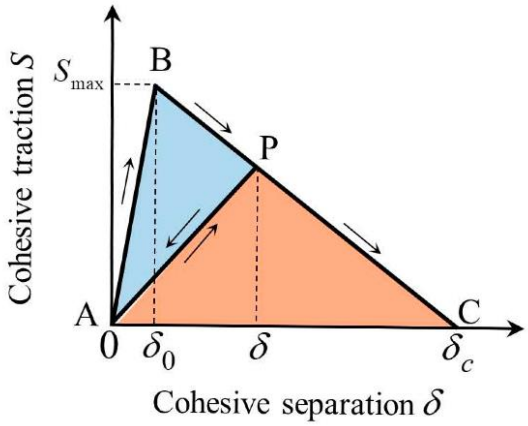

Figure 2 – Bilinear traction-separation law for cohesive elements.

Table 3 – Coefficients of friction for PBX9501 and two variants.

	HMX	Estane	HMX-Estane
PBX9501	0.5	0.5	0.5
$\mu = 0.25$	0.25	0.25	0.25
$\mu = 0.75$	0.75	0.75	0.75

2.2.6 Heat Conduction

Dissipation due to inelastic bulk deformation (viscoplastic or viscoelastic work) and friction along internal crack faces is converted to heat, resulting in temperature increases. Heat conduction is considered via

$$\rho c_v \frac{\partial T}{\partial t} = k\nabla^2 T + \eta \dot{W}^{p} + \dot{W}^{ve} + \dot{W}^{fric}, \tag{11}$$

Where k and c_v refer to thermal conductivity and specific heat, and T and t present temperature and time, respectively. The fraction of plastic work turned into heat, η, is equal to 0.9. $\dot{W}_p$ and $\dot{W}_f$ denote the rates of plastic work and frictional dissipation per unit volume, respectively. The frictional heating rate over volume ΔV with the coefficient of friction μ and surface ΔS is

$$\dot{W}_f = \frac{1}{\Delta V} \int_{\Delta S} \mu \sigma_n v_{rel} \, dS, \tag{12}$$

where σ_n and v_{rel} are the normal stress between the surface pair in contact and the relative sliding velocity, respectively.

2.2.7 Loading Configuration

At the onset of loading, the samples possess a uniform temperature of T = 300 K and are not damaged or loaded. Impact loading is effected by applying a specified boundary velocity at the left edge of the microstructures [see Figure 3(a)], which is linearly increased from zero to the maximums of 200, 400, 600, 800, 1000, and 1200 m/s with a prescribed linear ramp velocity over the initial 10 ns of loading $(0 \le t \le 10 \text{ ns})$, as shown in Figure 3(b). Vertical motions of the top and bottom boundaries of microstructures are constrained, approximating the planner impact loading under the conditions of macroscopically uniaxial strain. The length of all samples is 15 mm and it takes about $5.5\ \mu s$ for the longitudinal wave to propagate over the entire sample.

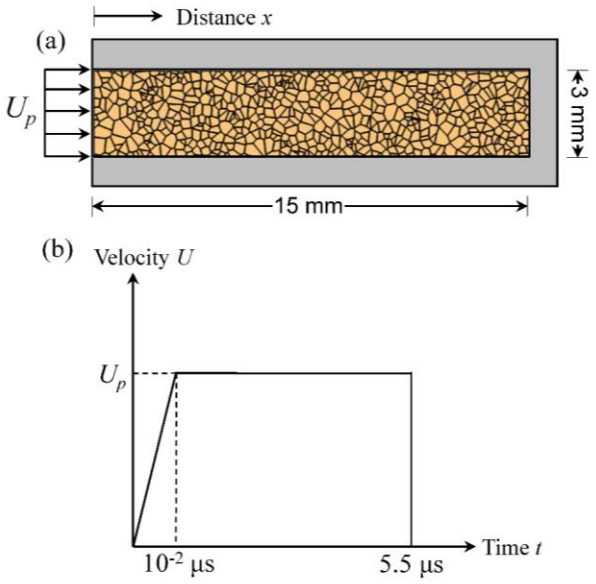

Figure 3 – (a) Loading configuration and boundary conditions considered for simulations, and (b) load history applied on the left edge of the sample.

2.2.8 Ignition Criterion

To determine the initiation of the HMX phase of PBX samples, a hotspot size-temperature ignition criterion is used [19]. Specifically, a hotspot at or above temperature T possesses sufficient energy for thermal runway (the onset of irreversible chemical decomposition) if its diameter $\left[\text{i.e., } d\left(T\right)\right]$ is equal to or greater than a certain value $\left[\text{i.e., } d_c\left(T\right)\right]$,

$$d\left(T\right) \geq d_c\left(T\right). \tag{13}$$

To identify the critical size-temperature condition of hotspots [right-hand side of Eq. (13)], the work of Tarver et al. [12] is used. This criterion is based on chemical kinetics calculations accounting for multi-step reaction mechanisms and the pressure and temperature dependence of reactants and products. According to the work of Barua et al.

[19], a specimen is assumed to proceed to ignition if two or more hotspots in a 3 mm square reach 90% of the critical size-temperature threshold calculated by Tarver et al. [12]. Reference [19] provides more details about this initiation criterion.

2.2.9 Statistical Model

The time to criticality of each sample is determined when sufficient critical hotspots according to the ignition criterion described in Section 2.4 emerge in the sample. For statistical analysis of the initiation time for the whole ensemble (the set of microstructure instantiations) at a given loading velocity, the work of Barua et al. [19] is used. Using Terao's model [64], Barua et al. [19] established a physical foundation for the Weibull distribution interpretation of the probability of time to criticality. In the used model [19], the time to criticality (t_c) is estimated as a cumulative probability distribution and fitted to the Weibull distribution [64] in the form of

$$P(t) = 1 - e^{-\Phi(t)}, \quad \Phi(t) = \begin{cases} 0 & t < t_0 \\ \left(\dfrac{t - t_0}{\tau} \right)^m & t \geq t_0 \end{cases} \tag{14}$$

where t, t_0, and τ are the time to criticality, the minimal time to criticality below which the probability of ignition is zero, and a time-scaling parameter that affects the slope of the distribution curve, respectively. m is a shape parameter and equal to 2 when stress wave propagation does not involve reflection from boundaries of a sample caused by loading conditions [19].

2.3 Results and Discussion

The ignition probability, the dissipation mechanisms, the damage evolution, and the hotspot characteristics of PBX9501 and its six variants under piston velocities from 200 m/s to 1,200 m/s are quantified. CFEM calculations are carried out to obtain the temperature field of samples subject to loading under the conditions discussed in Section 2.2.7. Next, the temperature fields are scanned to detect critical hotspots according to Section 2.2.8. Then, the ignition of samples is determined by finding sufficient critical hotspots, and energy dissipation resulting from the most dominant physical mechanisms and the damage evolution in the microstructures are calculated. Finally, for relative comparison of ignition sensitivity, the results are fitted to a load intensity-load duration relation over the entire range of loading space and material properties.

2.3.1 Axial Stress

The profiles of axial stress (compressive) in a microstructure subjected to a piston velocity of 400 m/s at $t = 0.4\,\mu s$ for PBX9501 and all its variants are compared. Figure 4 shows that lower levels of HMX plasticity causes decreases in the average longitudinal stress. In a homogeneous elastic-plastic solid undergoing plane strain loading, the stress-strain curve follows the constrained or P-wave modulus from the unloaded state to the onset of yielding and then follows the instantaneous bulk modulus. For a given material, the instantaneous bulk modulus is always lower than the constrained modulus, indicating that the stress in an elastic material should never be exceeded by that in an elastic-plastic material. However, Figure 4 shows the opposite trend, as a result of damage (fracture) induced by the loading event. For higher levels of constituent plasticity, the damage

induced is relatively small since plastic deformation reduces the stress levels in the microstructures. However, as stress level increases, the microstructures containing HMX with lower levels of constituent plasticity (higher yield stress levels) show significantly more damage than the microstructures with higher levels of HMX constituent plasticity (lower yield stress levels), causing the axial stress to decrease, as shown in Figure 4.

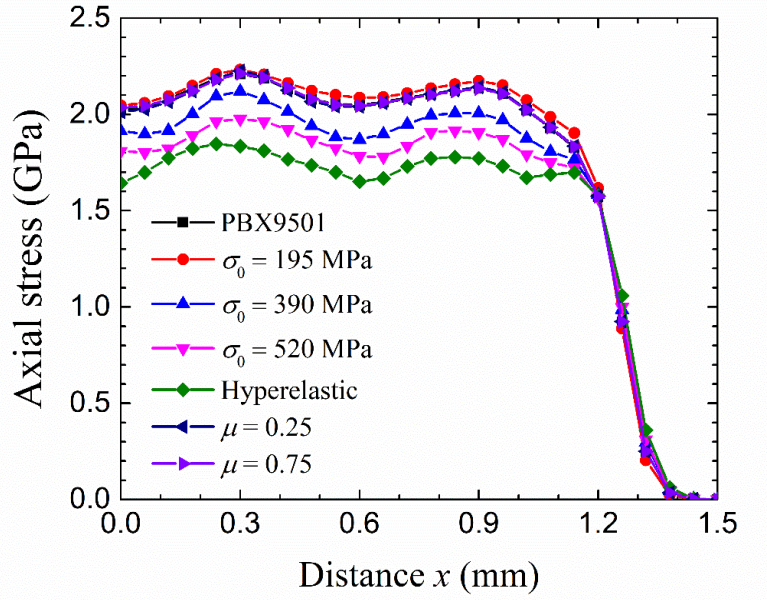

Figure 4 – Profiles of average axial stress at t = 0.4 µs for a microstructure subjected to a piston velocity of 400 m/s.

2.3.2 Temperature Fields and Hotspot Characteristics

Variations in microstructure morphology and the levels of constituent plasticity and friction provide perturbations to thermo-mechanical processes, causing temperature distributions to differ. Specifically, Figure 5 depicts the temperature field of a microstructure subjected to loading at 400 m/s for PBX9501 and its six variants at $t = 0.4\,\mu s$. A comparison of Figures 5(a-e) reveals that in samples with lower levels of constituent plasticity, the temperature distribution is more localized, leading to more

hotspots closer to criticality. A higher level of constituent plasticity results in a lower level of fracture (see Section 2.3.1), leading to less fracture and friction. Therefore, plasticity inhibits localized heating by friction, resulting in relatively more uniform temperature fields. Figures 5(f-g) show the temperature fields of the same microstructure but with different levels of internal friction. Unlike variations in the level of constituent plasticity, variations in the coefficient of friction affect primarily the peak temperatures. Fracture and subsequent frictional sliding occur primarily near the binder-grain interfaces. As a result, the peak temperatures occur near the grain-binder boundaries (see Figure 5). For the criticality analysis in Sections 2.3.5 and 2.3.6, only the temperature fields in the HMX grains are taken into account since HMX is the energetic phase. The effects of constituent variations on average and peak temperatures are shown in Figures 6(a) and 6(b), respectively. Variations in constituent friction affect peak temperatures more than the average temperatures. In addition, lower levels of constituent plasticity correspond to higher peak temperatures, as shown in Figure 6(b). The average temperature is higher in specimens with lower levels of constituent plasticity except in the region in the vicinity of the wave front since widespread plastic heating begins even in the wave front but the frictional heating does not begin until the wave front has passed through the region and caused fracture. Once the stress wave has passed through a region, the heating in specimens with lower levels of constituent plasticity begins to outpace the heating of specimens with higher levels of constituent plasticity.

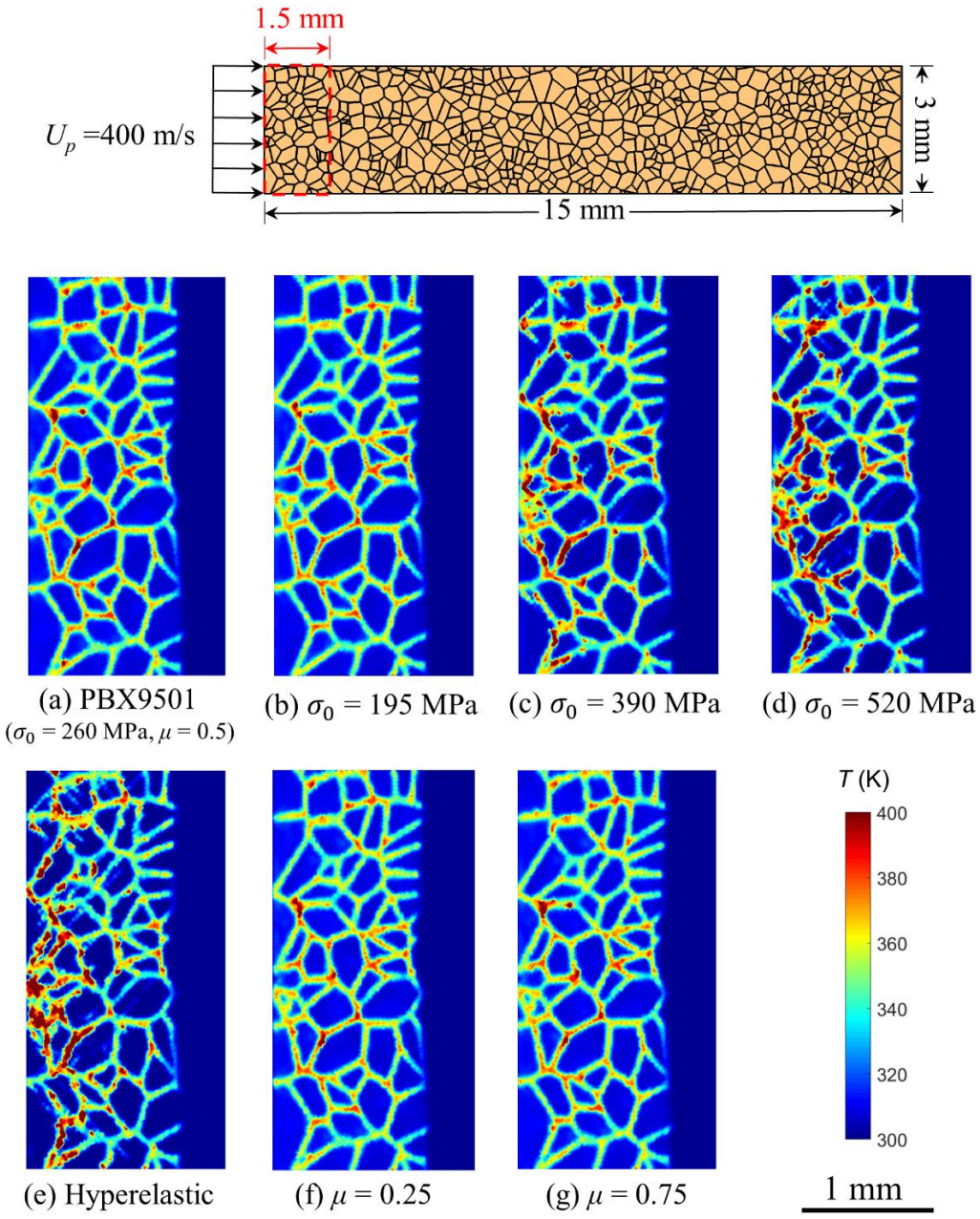

Figure 5 – Temperature fields and hotspot locations for all material cases under a loading velocity of 400 m/s at $t = 0.4\,\mu s$; (a) PBX9501, (b), (c), and (d) HMX grains with yield stress levels of 195, 390, and 520 MPa, respectively, (e) hyperelastic HMX grains, and (f) and (g) HMX grains with a yield stress level of 260 MPa and coefficients of friction 0.25 and 0.75, respectively. The peak temperatures occur near the boundaries between the binder and the grains.

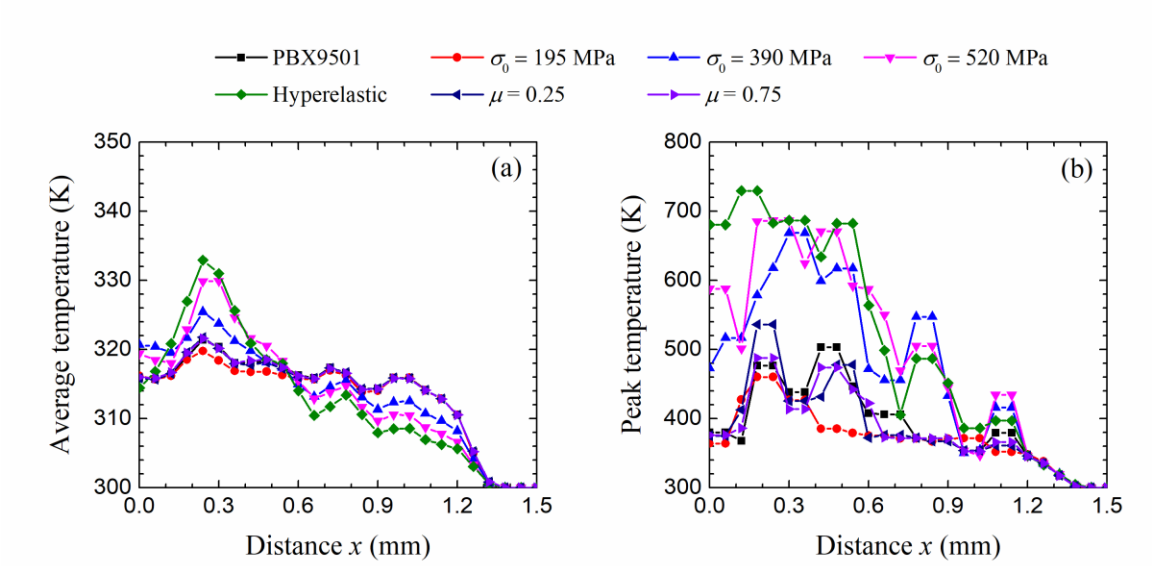

Figure 6 – (a) Profiles of average temperature and (b) profiles of peak temperature corresponding to the same microstructure in Figures 3 and 4. These figures show the temperature profiles prior to criticality of the samples.

The changes in temperature fields as a result of variations in constituent properties affect hotspots characteristics, which determine the ignition status of the material or the "go" or "no-go" state. Figures 7(a-c) use the *R*-value (see Ref. [19]) to quantify the overall hotspot conditions in samples under piston velocities of 200 m/s, 400 m/s, and 600 m/s, respectively. The *R*-value is the ratio between the temperature of a hotspot to the temperature of a critical hotspot of the same size. A hotspot with a value of *R*=1 is said to have reached criticality, and a hotspot of *R*=0 is still at an initial temperature of 300 K. Here, hotspots with a temperature equal to or above 305 K are considered in the analyses. Figures 7(a-b) show the *R* values of a microstructure at 200 m/s at $t = 3$ μs and at 400 m/s at $t = 0.4$ μs, respectively. At any given *R* value, the number of hotspots is higher when constituent plasticity is lower or constituent friction is higher. Similarly, Figure 7(c) shows the *R* curves for this microstructure at 600 m/s at $t = 0.2$ μs. Here, the number of hotspots

close to criticality $(R \geq 0.8)$ is higher at lower levels of constituent plasticity or higher levels constituent friction, leading to a higher propensity for ignition.

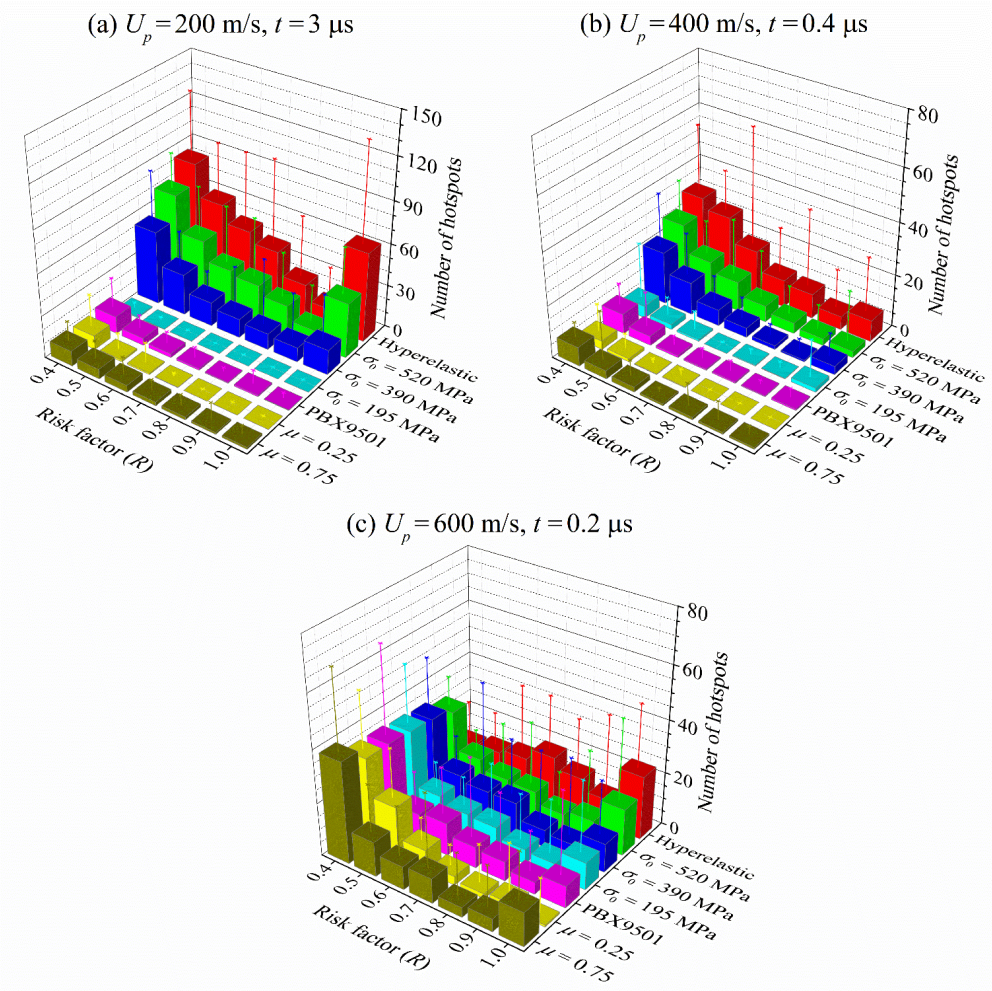

Figure 7 – Comparison of *R* curves for all material cases; (a) *R* curves for a microstructure under a loading velocity of 200 m/s at $t = 3$ μs, (b) *R* curves for a microstructure under a loading velocity of 400 m/s at $t = 0.4$ μs, and (c) *R* curves for a microstructure under a loading velocity of 600 m/s at $t = 0.2$ μs.

2.3.3 Energy Analysis

Figure 8 shows the total input work (W) at the time of ignition. The error bars indicate the degree of variation among the microstructures in each sample set. Samples

with higher levels plasticity (lower yield stress levels) or lower levels of friction (lower coefficients of friction) require higher overall input work to ignite, which means they are less sensitive to ignition. In addition, at higher piston velocities, the difference in critical input work among all cases tends to be lower in general. Specifically, at 200 m/s, the variation in the input work among all cases is 79.6% while at 1,200 m/s, the variation is 24.3%. These trends reflect the influences of several competing factors. Specifically, the load intensity affects the work input rate, dissipation rates, the speed at which the stress/shock wave propagates, and thermal conduction in different ways due to the non-linear nature of the material behavior and the underlying thermal-mechanical processes.

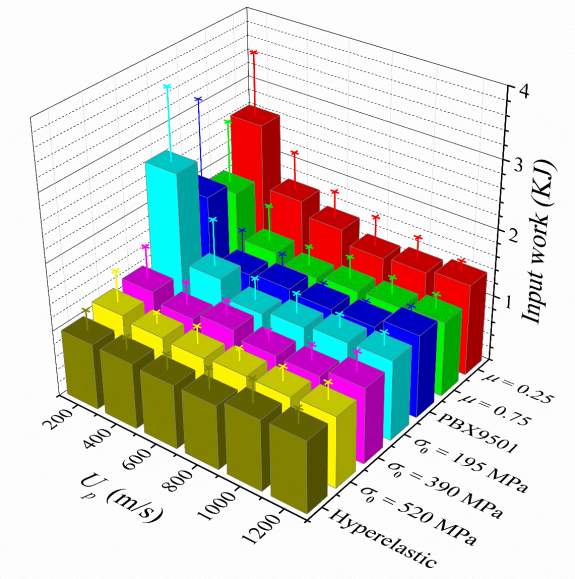

Figure 8 – Comparison of the required input work for ignition for all material cases over the range of piston velocities of 200-1,200 m/s.

Figures 9(a-f) show the evolution of two major mechanisms of energy dissipation in energetic materials (viscoplasticity and friction) for all sample sets under piston velocities of 200-600 m/s. Frictional dissipation increases when the amount of plastic deformation of energetic grains decreases as the result of higher yield strength levels,

reflecting the fact that fracture and consequent interfacial sliding account for a larger portion of the overall deformation as bulk plasticity decreases. In addition, frictional dissipations are negligible at early stages of deformation and then rapidly increase as the amount of cracks grows under loading [see Figures 9(a, c, and e)]. Viscoplastic dissipation, however, increase linearly from the beginning of loading [see Figures 9(b, d, and f)].

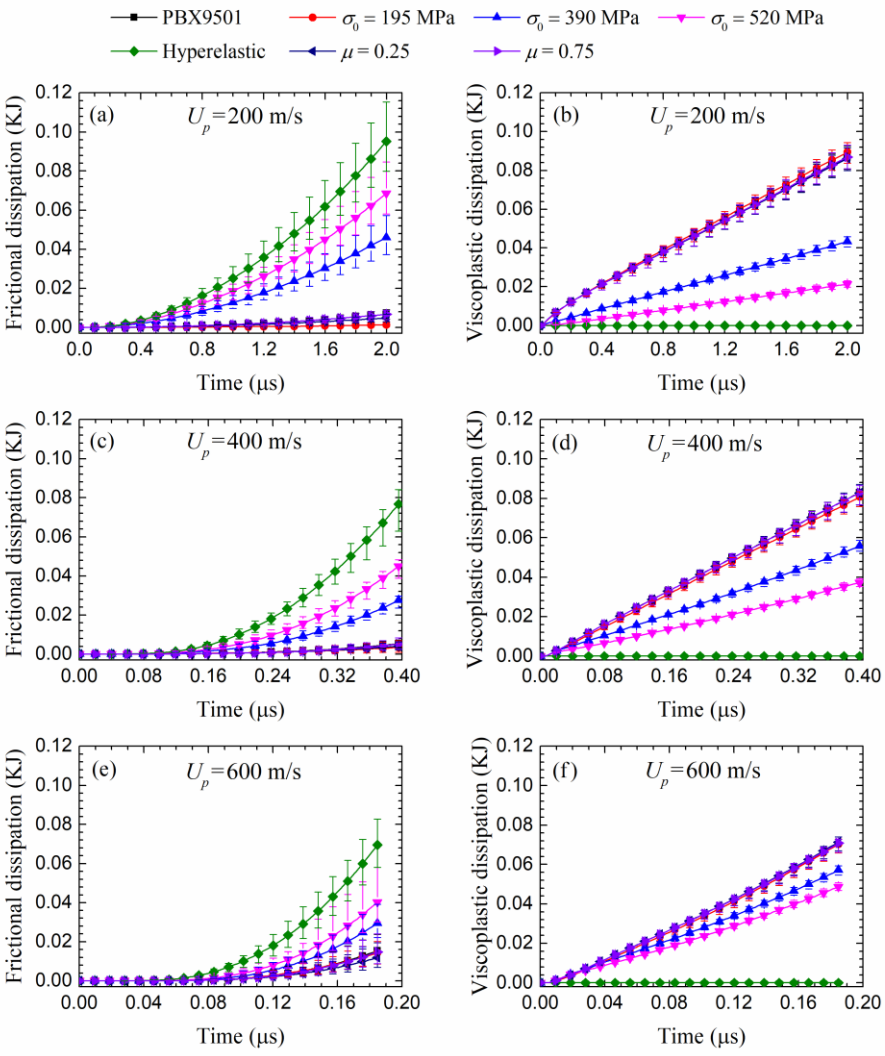

Figure 9 – Evolution of frictional dissipation and viscoplastic dissipation as a function of time for all cases; (a), (c), and (e) frictional dissipation for piston velocities of 200 m/s, 400 m/s, and 600 m/s, respectively, and (b), (d), and (f) viscoplastic dissipation for piston velocities of 200 m/s, 400 m/s, and 600 m/s, respectively.

Dissipations from friction, viscoelasticity, and 90% of viscoplasticity [$\eta = 0.9$ in Eq. (11)] turn into heat, contributing to the formation of hotspots. The amount of dissipation in samples at criticality is affected by the level of constituent plasticity and friction, load intensity, microstructure, and time to ignition. Figures 10(a) and 10(b) show the fraction of the input work dissipated by viscoplastic dissipation $\left(W_p/W\right)$, and frictional dissipation $\left(W_f/W\right)$ in all sample sets at the time of ignition, respectively. For hyperelastic HMX grains, W_p/W vanishes since the microstructural constituents do not undergo plastic deformation. Clearly, at any given load intensity, plastic dissipation decreases when the yield stress increases. The rise and fall in the trend of W_p/W versus piston velocity results from the competition between the intensity of loading and the time to ignition. At higher loading velocities, the rate of plastic deformation increases while the total time of deformation decreases since the samples reach criticality faster. The maximum values of W_p/W for $195\ \text{MPa} \le \sigma_0 \le 390\ \text{MPa}$ and $\sigma_0 = 520\ \text{MPa}$ occur under load velocities of 400 m/s and 600 m/s, respectively. For all levels of yield strength, W_p/W converges to approximately 2%, when the piston velocity exceeds 1,000 m/s. As the piston velocity increases from 200 m/s to 1,200 m/s, the fraction of the input work dissipated by friction $\left(W_f/W\right)$ fluctuates between 0.4% and 2% for samples consisting of viscoplastic grains with $195\ \text{MPa} \le \sigma_0 \le 260\ \text{MPa}$ while monotonically decreases for the $\sigma_0 \ge 390\ \text{MPa}$ and hyperelastic cases. The maximum frictional dissipation occurs in samples with hyperelastic HMX grains and for these samples, W_f/W decreases from 9.1% to 0.92% as the load velocity increases from 200 m/s to 1,200 m/s.

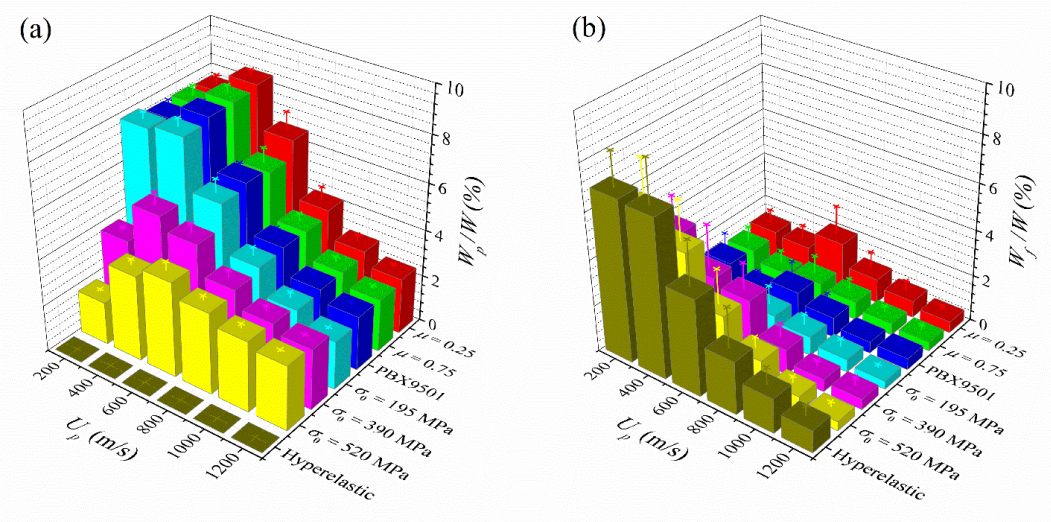

Figure 10 – Fraction of input work dissipated due to plastic deformation of HMX grains, and (b) fraction of input work dissipated due to friction at the time of ignition.

For PBX9501, while overall viscoplastic heating at the whole microstructure level is 4.2-10.9 times (depending on the load intensity and the microstructure morphology) frictional heating, the contributions to the development of hotspots (which are responsible for ignition, not the overall average temperature) are different. To see this, the local heat generations in hotspots is analyzed. Figure 11 shows the densities of viscoplastic heating and frictional heating (heat per unit volume of hotspots) in all hotspots with $R \geq 0.6$ at t_{50} for 200, 800, and 1200 m/s. The data is for the 20 random microstructure instantiations in the sample set, so both the averages and the ranges of variation among the 20 samples are shown. At 200 m/s, although overall in the samples viscoplastic heating is 5.2 times frictional heating (Figure 10), frictional heating dominates and accounts for 76.1% of the heating inside the hotspots [Figure 11(a)]. As the load intensity increases, the contribution of friction decreases and the contribution of plasticity increases. Specifically at 800 m/s, friction and plasticity each accounts for ~50% of the heating in the hotspots [Figure 11(b)]. At 1,200 m/s, the contribution of friction decreases to ~29.5% and the contribution of

viscoplasticity increases to ~70.5% [Figure 11(c)]. The trend is generally consistent with that in Figure 9. The new insight here is that friction plays an important role in the development of hotspots which are responsible for the ignition and detonation of PBX, even up to the piston velocity of 1,200 m/s. As the trend implies, it is possible that, at much higher load intensities, the effect of friction diminishes.

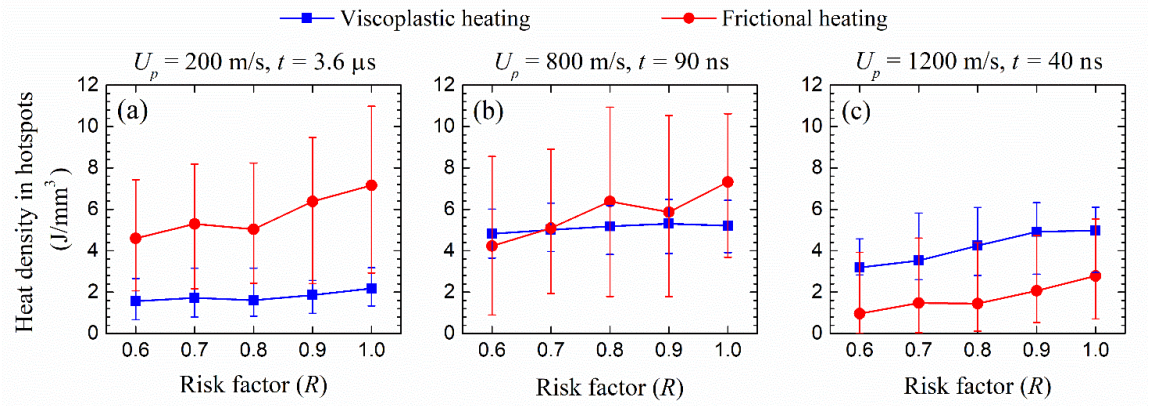

Figure 11 – Comparison of viscoplastic and frictional heating per unit volume in all hotspots with risk factors of $R \geq 0.6$ in PBX9501 samples; (a) $U_p = 200$ m/s, $t = 3.6$ μs, (b) $U_p = 800$ m/s, $t = 90$ ns, and (c) $U_p = 1200$ m/s, $t = 40$ ns.

Figures 12(a) and 12(b) show the total amount of heat generated in the samples (H) and the fraction of input work converted to heat at the time of ignition (H/W), respectively. Even though samples with higher levels of constituent plasticity or lower levels of constituent friction are less sensitive to ignition, these samples undergo more heating up to the time of ignition. The dissipation resulting from bulk viscoplasticity spreads more widely in the material (less localized), resulting in a more uniform temperature field. A sample with a more uniform temperature field is less likely to ignite, as it has fewer and cooler hotspots (see Section 2.3.2). In addition, although the total amount of dissipation is lower at higher velocities, the dissipation is more localized and

concentrated in smaller areas of the materials, leading to ignition. Specifically, the increase in the loading velocity from 200 m/s to 1,200 m/s causes the amount of heat generated to decrease from 543.6 J to 114.1 J for PBX9501. The fraction of input work turned into heat at the time of ignition (H/W) is approximately equal for all cases at a given load intensity level. H/W decreases at higher levels of load intensity since the total amount of dissipation at the time of ignition decreases as a result of shorter durations of deformation prior to the onset of ignition. In particular, an increase in the load velocity from 200 m/s to 1,200 m/s causes H/W to decrease approximately from 25.8% to 8.8% for all sample sets. At a given load intensity level, the discrepancy in H/W among all the material variants is 2.2-4.1%.

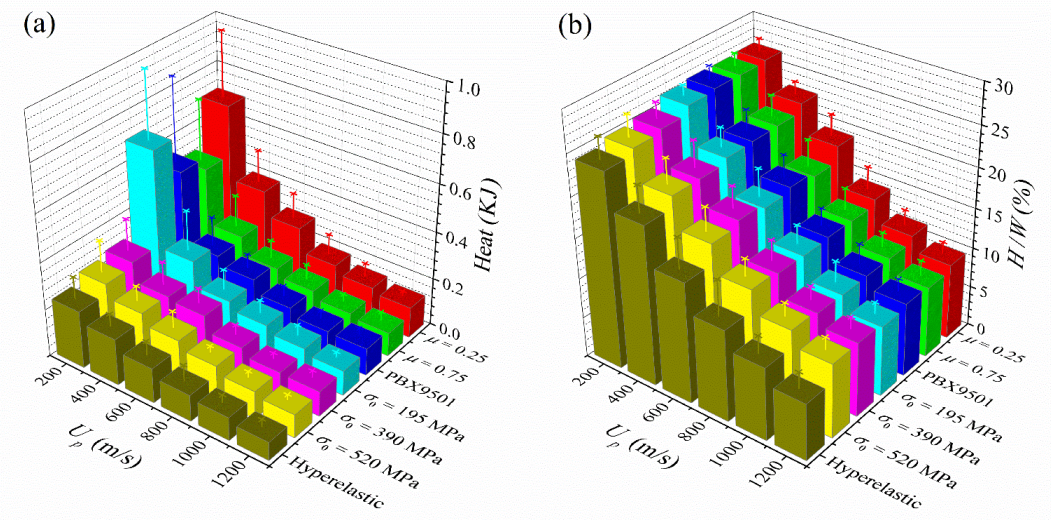

Figure 12 – (a) The amount of heat generated, and (b) the fraction of input work converted to heat, at the time of ignition for all cases over the range of piston velocities of 200-1,200 m/s.

2.3.4 Crack Density and Distribution

This study assumes that samples are initially defect-free (no voids, no cracks) and that cracks result from loading. The analysis accounts for fracture along all possible types of sites including inside the HMX grains, inside the matrix, and the grain-matrix interfaces. Figures 13(a-f) show the crack density, or crack area per unit volume of the material, at approximately median time to ignition $\left(t_{50}\right)$ for all sample sets over the range of piston velocity of 200-1,200 m/s. The density of cracks is higher when the level of constituent plasticity is lower (yield stress higher), illustrating the competition between plastic deformation and fracture (see Section 2.3.1). Since cracks lead to frictional dissipation, the trend for crack density is similar to that for frictional dissipation $\left(W_f / W\right)$. The density of cracks in the binder is negligible due to the fact that the volume fraction of the binder is less than that in the grains and the binder is softer.

The crack densities at HMX/Estane interfaces (grain boundaries) are higher than those in the HMX grains at a piston velocity of 200 m/s while fracture sites in the grains outnumber those at the interfaces at piston velocities above 400 m/s. At higher piston velocities, the variations of the crack density at boundaries among cases decrease since most of grain/matrix sites affected by the stress wave are fractured and further energy dissipation by fracture mostly is accommodated by the grains. These trends are qualitatively consistent with experimental results for PBX9501 reported in the literature. For example, under quasi-static conditions, grain fracture is relatively insignificant and debonding of grains from the binder is the dominant fracture mode, except for pre-damaged

HMX grains [65]. At high-strain rates (for example, 2000 s^{-1}), however, PBX9501 fails via predominantly transgranular fracture of the HMX grains [66].

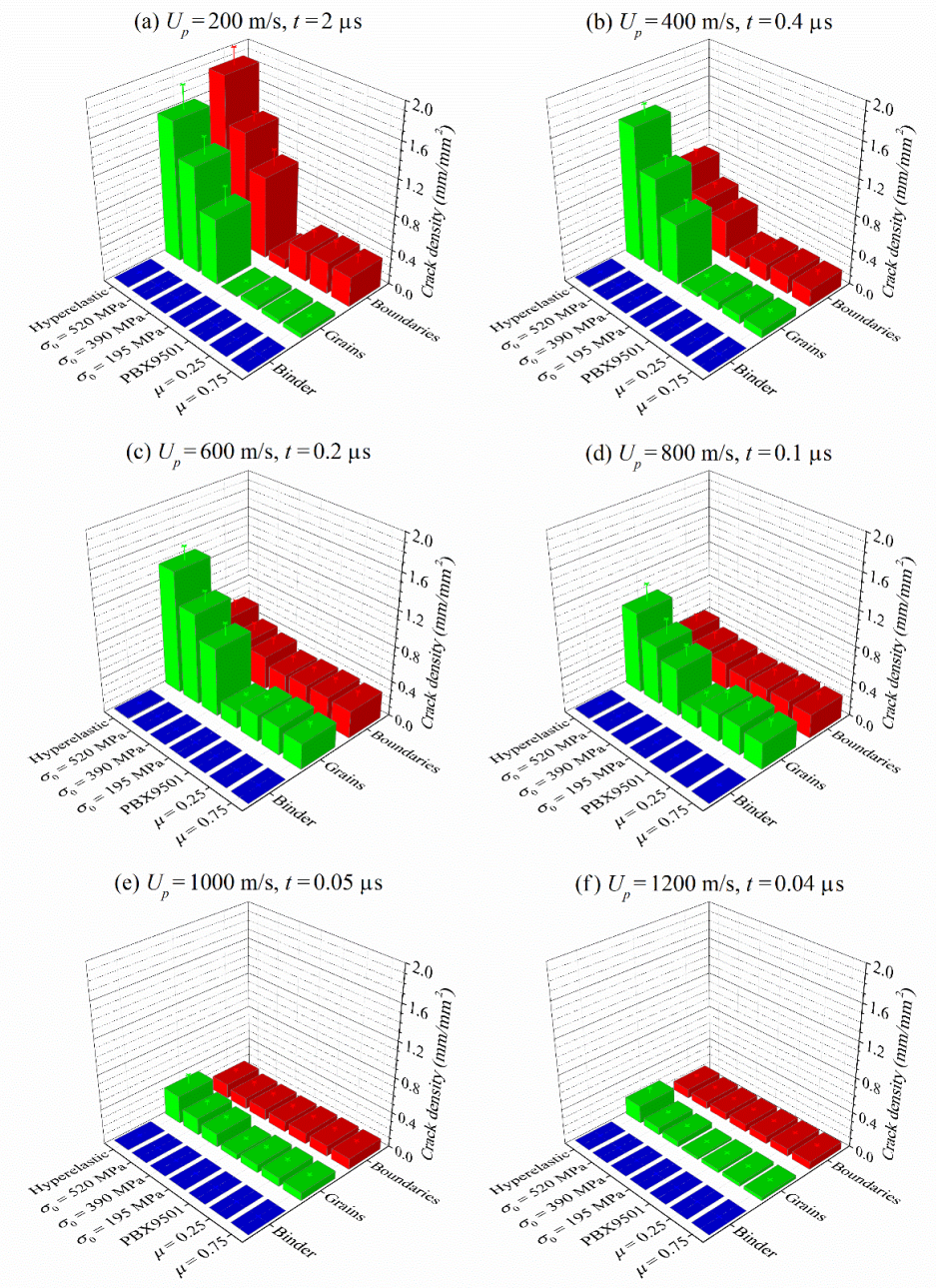

Figure 13 – Densities of cracks at the binder, grains, grain/binder boundaries; (a) U_p = 200 m/s, t = 2 μs, (b) U_p = 400 m/s, t = 0.4 μs, (c) U_p = 600 m/s, t = 0.2 μs, (d) U_p = 800 m/s, t = 0.1 μs, (e) U_p = 1000 m/s, t = 0.05 μs, and (f) U_p = 1200 m/s, t = 0.04 μs.

2.3.5 Probability Distribution of the Time to Criticality

The probability distribution curves for ignition are constructed based on the "go" / "no-go" analysis [19]. To account for the microstructural stochasticity involved in a material's ignition response, the "go" / "no-go" analysis is performed on twenty statistically similar samples for each of combination of constituent plasticity and internal friction level considered. Figures 14(a-c) show probability distributions of the time to criticality t_c for microstructures with the four levels of constituent plasticity of energetic grains at piston velocities of 200 m/s, 400 m/s, and 600 m/s. In these figures, the symbols represent calculated results and the solid lines represent the corresponding fits to the Weibull distribution. The least square regression method is used to calculate the two parameters in the Weibull distribution, t_0 and τ. For a piston velocity of 200 m/s and a HMX yield stress of $\sigma_0 = 195$ MPa, five out of the twenty microstructures in the sample set did not reach criticality within 5.5 μs. The Weibull function is fitted to the data for samples that ignite within 5.5 μs. The value of the parameters for the Weibull distribution function and the median time to ignition (t_{50}) for each simulation set are listed in Table 4.

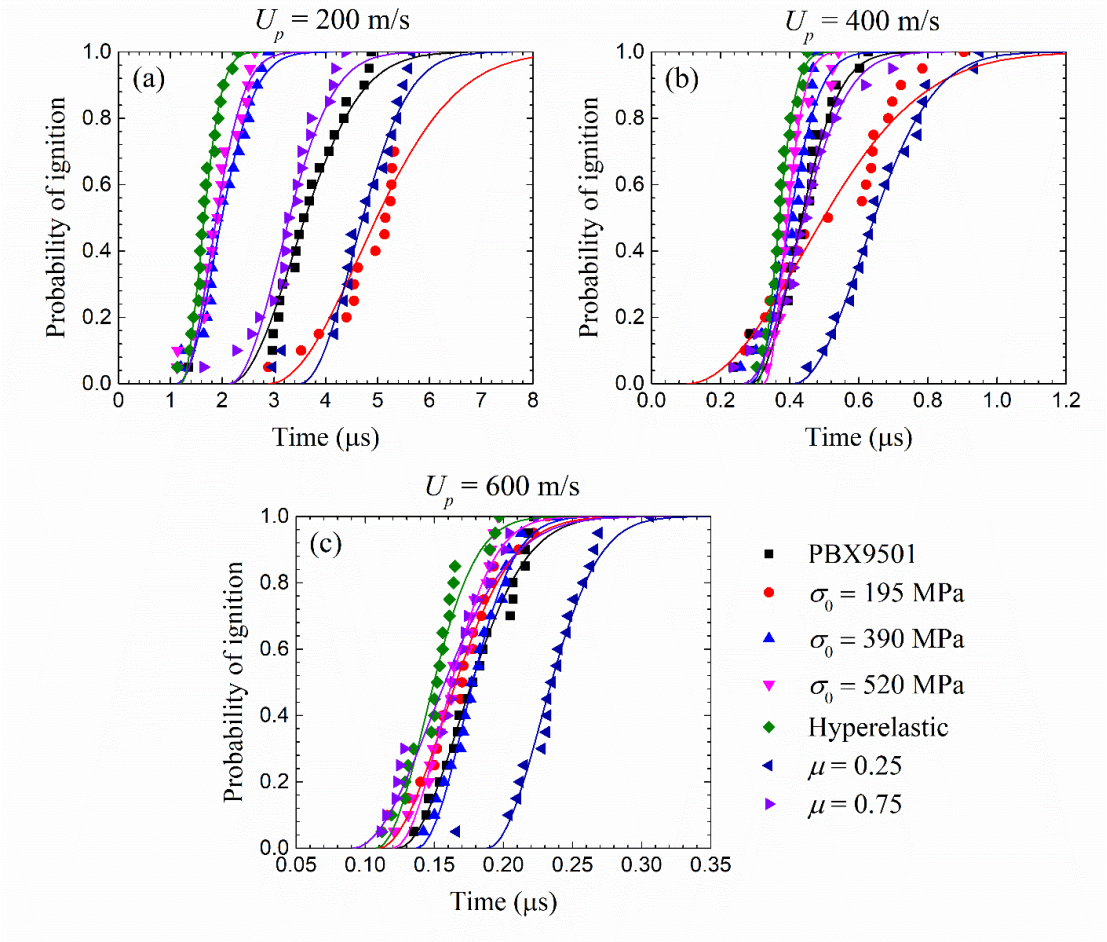

Figure 14 – Distribution of the ignition probability (symbols) and the corresponding Weibull fit (solid lines); (a) piston velocity of 200 m/s, (b) piston velocity of 400 m/s, and (c) piston velocity of 600 m/s.

Table 4 – Parameters for the adjusted time Weibull distributions.

			200 m/s	400 m/s	600 m/s	800 m/s	1000 m/s	1200 m/s
PBX 9501	$\sigma_0 = 260$ MPa $\mu = 0.5$	t_0 (μs)	2.13	0.29	0.12	0.07	0.04	0.03
		t_{50} (μs)	3.6	0.43	0.18	0.09	0.06	0.04
		τ (10^{-6})	1.77	0.17	0.07	0.02	0.02	0.01
Levels of HMX plasticity	$\sigma_0 = 195$ MPa	t_0 (μs)	2.89	0.1	0.11	0.06	0.04	0.03
		t_{50} (μs)	4.98	0.5	0.17	0.09	0.06	0.04
		τ (10^{-6})	2.51	0.47	0.07	0.03	0.02	0.01
	$\sigma_0 = 390$ MPa	t_0 (μs)	1.13	0.28	0.14	0.07	0.04	0.03
		t_{50} (μs)	1.99	0.4	0.18	0.09	0.05	0.04
		τ (10^{-6})	1.03	0.14	0.05	0.02	0.01	0.01
	$\sigma_0 = 520$ MPa	t_0 (μs)	1.16	0.32	0.12	0.07	0.04	0.03
		t_{50} (μs)	1.89	0.39	0.16	0.09	0.05	0.04
		τ (10^{-6})	0.87	0.08	0.05	0.02	0.01	0.01
	Hyperelastic	t_0 (μs)	1.2	0.3	0.11	0.06	0.04	0.03
		t_{50} (μs)	1.65	0.37	0.15	0.08	0.06	0.04
		τ (10^{-6})	0.55	0.08	0.05	0.03	0.01	0.01
Coefficients of friction	0.25	t_0 (μs)	3.5	0.41	0.19	0.08	0.05	0.04
		t_{50} (μs)	4.71	0.64	0.23	0.11	0.07	0.05
		τ (10^{-6})	1.45	0.28	0.06	0.03	0.02	0.01
	0.75	t_0 (μs)	2.13	0.27	0.09	0.07	0.04	0.03
		t_{50} (μs)	3.29	0.44	0.16	0.09	0.05	0.04
		τ (10^{-6})	1.39	0.21	0.08	0.03	0.02	0.01

Results show that lower levels of constituent plasticity (higher yield strength) or higher levels of constituent friction make microstructures less sensitive to ignition (delayed ignition). In general, samples with longer time to criticality are regarded as "less sensitive." These results are in agreement with the findings in Section 2.3.2, where the hotspot analysis revealed that lower levels of constituent plasticity or higher levels of constituent friction increase the numbers or the risk factors of hotspots. Figure 15 shows the median time to

ignition (t_{50}) as a function of loading velocity. The decrease in t_{50} at higher loading velocities indicates higher likelihood for ignition. The differences in the time to criticality among samples in a set and the mean time to criticality (t_{50}) decrease as the piston velocity increases. Furthermore, the difference in t_{50} for cases with different yield stress levels also decreases as the velocity (load intensity) increases. Specifically, the maximum difference in the median time to ignition (t_{50}) for a piston velocity of 200 m/s is 85.8% and decreases to below 7% as the piston velocity reaches 1,200 m/s, as shown in Figure 15. In addition, the variation in the time to criticality among the microstructures decreases as plasticity decreases. In Eq. 14, τ affects the overall slope (and spread) of the probability distribution curve for ignition. At each loading velocity, as the level of constituent plasticity increases, τ increases, indicating a wider spread of the probability distribution.

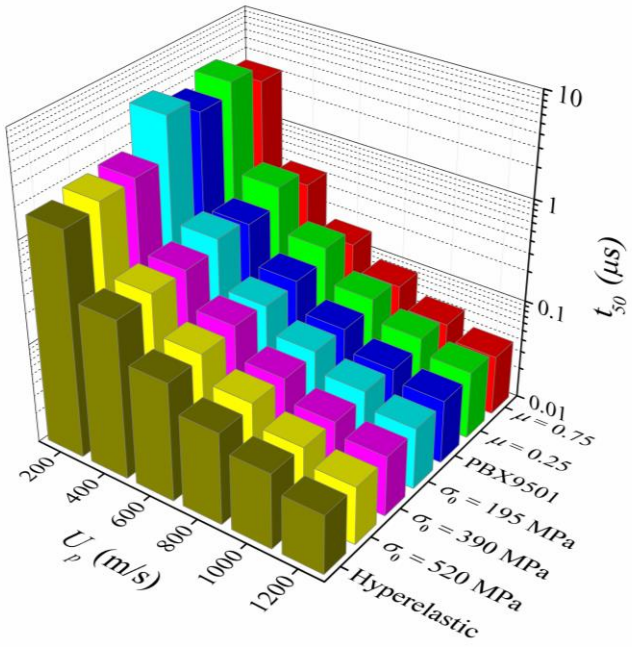

Figure 15 – Median time to ignition as a function of load intensity and levels of constituent plasticity and friction.

2.3.6 Ignition Threshold

For relative comparison of ignition sensitivity, the results are fitted to a load intensity-load duration relation of the form

$$P^2 \, t_{50} = C, \tag{15}$$

where P is the average longitudinal stress at the loading site, t_{50} is the median time to criticality, and C is a material-dependent fitting constant. A higher value for C indicates lower ignition sensitivity. Figure 16 shows the average longitudinal stress versus the mean time to criticality for all load levels and sample sets. The results for all material variants are then fit to determine the value of C that best represents the data. The values of C for all material variants are listed in Table 5. This approach provides a convenient method for the relative comparison of sensitivity. In Figure 16, any event lying to the left of a line has an ignition probability lower than 50% and any event falling to the right of the line has an ignition probability of higher than 50%. Therefore, a more sensitive sample set lays farther to the left in the $P - t_{50}$ space. The results are in agreement with the earlier ignition probability analyses indicating that the specimens with higher levels of constituent plasticity or lower levels of friction are less sensitive.

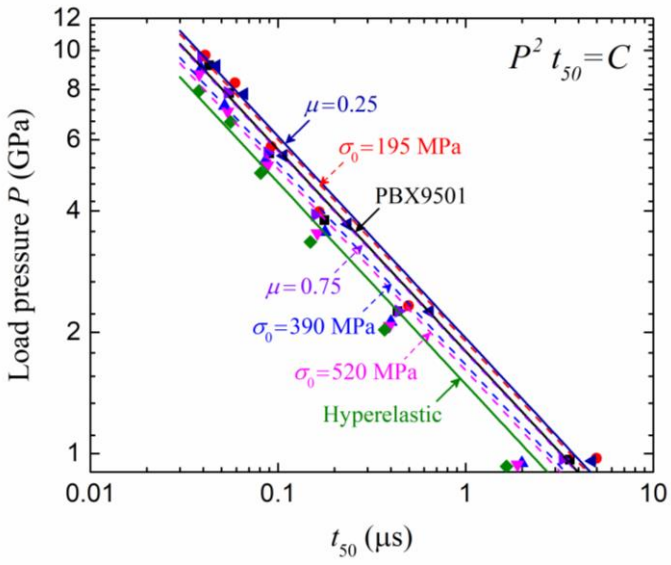

Figure 16 – Comparison of 50% ignition thresholds for PBX9501 and its six variants.

Table 5 – Parameter C in the load intensity-load duration ignition threshold $\left(P^2 t_{50} = C\right)$ for PBX9501 and its six variants.

		Levels of HMX plasticity (σ_0)				Coefficients of friction (μ)	
	PBX9501	195 MPa	390 MPa	520 MPa	Hyperelastic	0.25	0.75
C $\left(10^{12}\ \text{Pa}^2.\text{s}\right)$	3.225	3.608	2.759	2.588	2.212	3.748	3.174

2.4 Summary

The need to understand and quantify the relative importance of the contributions of plasticity and internal friction to dissipation and heating in polymer-bonded explosives (PBXs) motivates this study. To achieve the objective, a Lagrangian cohesive finite element framework is used to analyze the thermo-mechanical response and ignition behavior of PBX9501 and its variants. The analyses focus on material behavior at various

levels of constituent friction, HMX grain plasticity, and load intensity. To this effect, hyperelastic and viscoplastic constitutive models are used. Statistically similar microstructure samples are computationally generated and subjected to monotonic loading with piston velocities of 200-1,200 m/s. The ignition probability, the dissipation mechanisms, the damage evolution, and the hotspot characteristics are quantified and analyzed. The results are compared with available experimental results for PBX9501.

The results show that plastic deformation of the energetic grains of the heterogeneous PBXs significantly influence their response and ignition behavior. Despite more overall heat generation, a higher level of constituent plasticity results in a decreased sensitivity to ignition as it reduces peak temperatures and the number or the risk factor of hotspots. This reduction in localized heating results from significant reduction in the density of fracture sites. Fracture and subsequent crack face friction significantly affect heat generation by facilitating and enabling inelastic deformation and, more importantly, localized frictional heating along crack faces. Energy dissipation from plastic deformation spreads more widely in the material and is less localized. In contrast, dissipation and heating due to friction are more localized and play an important role in the development of hotspots, even up to piston velocities of 1,200 m/s.

The time to ignition is analyzed and quantified using the Weibull distribution function, providing explicit expressions for the ignition probability as a function of load intensity and HMX yield strength. The 50% ignition thresholds obtained are analyzed and presented in a load-intensity-load duration relation $\left(P^2 t_{50} = C\right)$. The analysis reveals that samples with higher levels of constituent plasticity or lower levels of constituent friction are less sensitive. Finally, it is worthwhile to put the analyses reported here in perspective:

obviously, plasticity and fracture/internal friction both can play important roles in the ignition of energetic materials, such that neither should be ignored for the conditions analyzed here (piston velocities up to and somewhat higher than 1,200 m/s) and for realistic PBXs. In the idealized limit case of a fully ductile energetic material incapable of fracture (likely does not exist in reality), plasticity would be the sole heating mechanism leading to ignition. On the other hand in the idealized limit case of a fully brittle energetic material (again likely does not exist in reality), fracture and friction would be the heating mechanisms for ignition. Real materials, like what is modeled here, are in between the two limits and have behaviors that reflect the competition and interplay among the heating mechanisms, microstructure, and loading. This chapter provides insights into dissipation mechanisms leading to ignition that can be used to sensitize or desensitize polymer-bonded explosives.

CHAPTER 3. NOVEL CAPABILITY FOR MICROSCALE IN-SITU IMAGING OF TEMPERATURE AND DEFORMATION FIELDS UNDER DYNAMIC LOADING

This chapter is based on the work published in Ref. [67].

3.1 Introduction

The experimental study of the thermo-mechanical response of such heterogeneous materials at the microstructure level under dynamic loading has been especially challenging due to limitations of existing techniques for deformation and temperature measurements at high speeds and high spatial resolutions over the same area of a sample. As a result, dynamic experiments have been limited to either mechanical deformation or thermal responses. Specifically, these experiments have been based on indirect/implied correlations between deformation mechanisms and thermal responses [11, 15, 68], without quantitative measurements that can directly relate the mechanical and thermal events.

For time-resolved temperature measurements in dynamic experiments, researchers have used several approaches including embedded electrical sensors [69, 70], optical pyrometry [71], Raman spectroscopy [72], Neutron resonance spectroscopy [73], and reflectance thermometry [74, 75]. All of these approaches have some advantages and disadvantages. For example, embedded electrical sensors can measure the temperature of a sample with high accuracy and is independent of the sample properties. However, thick sensors do not equilibrate with the sample quickly enough and thin sensors may break before or during experiments, as a result, the technique cannot be used for highly dynamic

events. This challenge can be avoided by using non-contact approaches including optical pyrometry and Raman spectroscopy. However, these non-contact approaches so far offer bulk average measures, require the knowledge of the sample properties such as radiance and emissivity, and do not offer high spatial resolutions. The reflectance thermometry approach uses light reflected from the sample rather than radiation emitted by the sample, which does not require knowledge of the properties of the sample but again requires the adherence of an extrinsic material on the sample and depends on thermal equilibration between the sample and the extrinsic material film [74, 75]. None of these methods allow simultaneous recording of both deformation and temperature fields over an area of a sample's microstructure.

The work by Coffey and Jacobs [76] was an early attempt to estimate the temperature achieved during deformation in impact experiments. The technique uses heat-sensitive films which darken upon exposure to heat. Since darkening levels of the heat-sensitive films depend on both temperature and time, the time of deformation must be known to estimate temperature levels based on calibration curves. Later, heat-sensitive films along with high-speed photography were used to study primary failure mechanisms in polymer bounded explosives (PBXs) at the macroscale [10]. However, this technique cannot reveal the underlying mechanisms at micron levels. In the 1980s and 1990s, advances in infrared detectors made it possible to measure temperature in real time with microscale spatial resolutions. For example, Marchand and Duffy [2], Zehnder and Rosakis [77] and Zhou et al. [3, 78] used an integrated system of infrared thermal detectors to measure temperature variations along lines across cracks and shear bands in metals. High-

speed photography was also used to study the associated mechanical processes, but at different (larger) size scales.

Measuring temperatures of a material with thermocouples, spot pyrometers, heat sensitive films, or infrared temperature detectors along lines or over small areas has provided useful information and insight. The measurements, to various degrees, are averaged over space and time, or only available over small domains. For example, Costin et al. [79] used only one infrared detector and homogenized the temperature over a spot size of 1 mm. Later, Hartley et al. [1] used a linear array of infrared detectors and measured the temperature over a spot size of $20\ \mu m$. Similarly, Merchand and Duffy [2], and Zhou et al. [3, 78] used linear arrays of 12-16 infrared detectors with spot sizes of $35-100\ \mu m$. In the first spatial temperature measurement effort, Guduru et al. [4] developed and used a spatial array of 8×8 infrared detectors, with each detector measuring the average temperature over an area of $110\times110\ \mu m$. These methods are quite advanced and are still in further development. However, so far the spatial or temporal resolutions certainly show need for significant improvement before full characterization of events at the microstructure level at high loading rates are possible. In particular, for heterogeneous materials, the differing emissivities of multiple constituents must be accounted for in order for correct temperatures to be obtained. This task requires an independent image of the evolving material microstructure that is in addition to the IR image as deformation occurs. Existing capabilities do not offer such independent images.

For quasi-static conditions, infrared (IR) cameras have been used along with visible light (VL) cameras for simultaneous temperature and deformation measurements. For example, an experimental environment consist of VL and IR cameras was used to measure temperature and deformation fields during glass forming [80]. The VL and IR imaging was not at normal incidence since the cameras have different angles of view. Further, the measurement was macroscopic and not microscopic. A dichroic mirror was used to separate VL and IR emissions from the sample surface to achieve imaging at normal angle [81, 82] in a setup for quasi-static conditions with a maximum stain rate of 5×10^{-3} s^{-1}. High-speed infrared cameras have recently developed to a point where capturing time- and space-resolved measurements over areas on the order of millimeters is now possible, at resolutions of microns and microseconds. Although the IR imaging capabilities are still not on par with visible spectrum imaging, simultaneous measurements for deformations rates on the order of 10^3 s^{-1} typical of Kolsky bar (or split-Hopkinson bars) can be achieved.

The split-Hopkinson pressure bar (SHPB) or Kolsky bar apparatus (KBA) is a well-established experimental technique for characterizing materials and structures under dynamic loads. The SHPB apparatus was established by Hopkinson [83], with further developments by Kolsky [84]. Since its advent, it has been improved and extended for a wide range of applications such as dynamic compression and tension tests [85, 86], torsion tests (torsional split-Hopkinson bar or TSHB) [87, 88], the Brazilian test [89, 90], fracture toughness measurements [91-93], wave separation and dispersion tests [94-96], dynamic loading experiments on geotechnical materials [97] and soft materials [98], and other high strain rate experiments [99]. The SHPB apparatus or the KBA provides stress-strain, strain-time, and strain rate-time relations [100], which can be used to validate constitutive

relations of materials at high strain rates [101]. The SHPB apparatus also has been used along with infrared detectors to analyze the overall thermo-mechanical response of materials [5, 6]. The classic devices allow for only macro-scale analyses of dynamic response of materials. For meso-scale analyses of deformation in materials, the SHPB apparatus has been used along with high-speed photography [68, 90, 101, 102] and high-speed x-ray imaging [103].

This chapter reports the development of a novel capability for simultaneous, time-resolved and space-resolved recording of both the temperature field and the deformation field over the same microstructure area of a sample with micron-level spatial resolutions and microsecond temporal resolutions. Referred to as MINTED (**M**icroscale **In**-situ Imaging of Dynamic **Te**mperature and **D**eformation Fields), the system cohesively integrates a high-speed visible light (VL) camera and a state-of-the-art high-speed infrared (IR) camera via a custom-designed dichroic beam splitter-lens assembly. The combined VL and IR images allow the deformation fields to be obtained through digital image correlation (DIC) and the temperature fields over the same area to be obtained through pixel-level calibration of the differing emissivities of heterogeneous constituents in microstructures. Experiments are conducted on granular sucrose which is widely used as a simulant of energetic crystals [104] in a KBA or SHPB environment, yielding both microstructure level fields along with overall material response. The strain and temperature provide detailed first-time insight into the processes of fracture, friction, shear localization, and hotspot development in the microstructures. In particular, the correlation between hotspots, microstructure, and local deformation mechanisms is analyzed.

3.2 Experimental Layout

The overall configuration of the MINTED system in a SHPB environment is illustrated in Figure 17. To simultaneously capture deformation and temperature fields, the visible (VL) and infrared (IR) parts of the emission spectrum from the sample pass through a sapphire window and are separated by a dichroic beam splitter. VL is reflected and IR is transmitted. The VL reflection efficiency of the dichroic beam splitter and the IR transmission efficiency are both greater than 85%. The VL camera is mounted vertically, while the IR camera is mounted horizontally, directly facing the sample surface. The sample is encased in a specimen holder, as discussed later. The IR emission passes through a set of custom-designed correction lenses to correct wave-front distortions induced by the non-normal incidence of the IR beam at the beam splitter which has a finite thickness. The IR and VL cameras are synchronized in time and calibrated in spatial positions (see below), consequently, the VL and IR images can be coordinated for the extraction of the deformation and temperature fields. A triggering system is designed and built to operate the two cameras simultaneously. Two sets of sensors are placed close to the incident bar to detect the motion of the bar and trigger the cameras and other devices via a control box. The control box also activates electric solenoid valves to run an air gun to start the experiment and secure the loading mechanism. Illustrations and pictures of the experimental setup are shown in Figures 17 and 18, respectively.

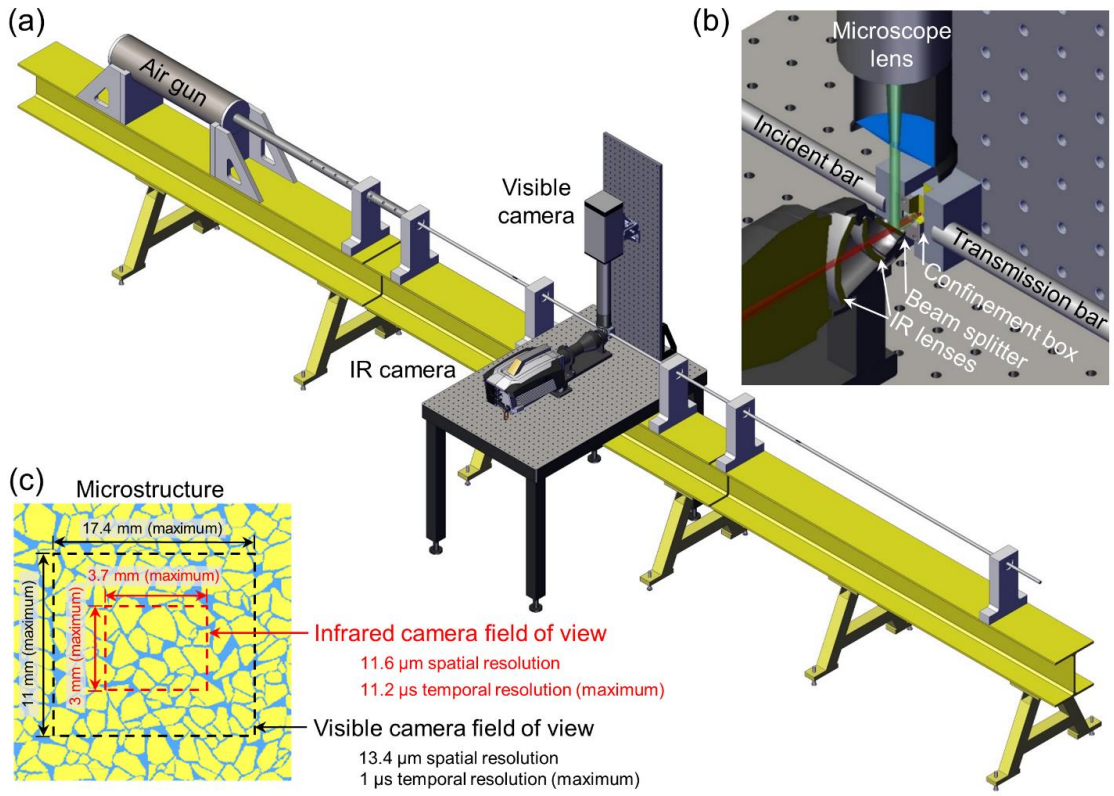

Figure 17 – Experimental setup for simultaneous high-speed infrared (IR) and visible (VL) imaging of microscale temperature and deformation fields under dynamic conditions; (a) configuration of the split-Hopkinson bar apparatus and visible and infrared cameras, (b) relative positions of the confinement box, the dichroic beam splitter, the visible microscope lens, and the infrared lens assembly, and (c) relative positions of visible and infrared fields of view.

3.2.1 High-speed Photography of Deformation Fields

A Phantom v2512 camera, which can operate at 25,700 fps at 1-megapixel (MP) resolution and 1,000,000 frames per second (fps) at 128×32 pixels, is used to record the VL images. An Infinity K1 long-distance microscope lens is used along with the VL camera to zoom in far enough to capture high-resolution micro-scale images. The VL lens magnification factor is 2.09 and the working distance is 145 mm. The IR camera operates with an 13.4 µm spatial resolution.

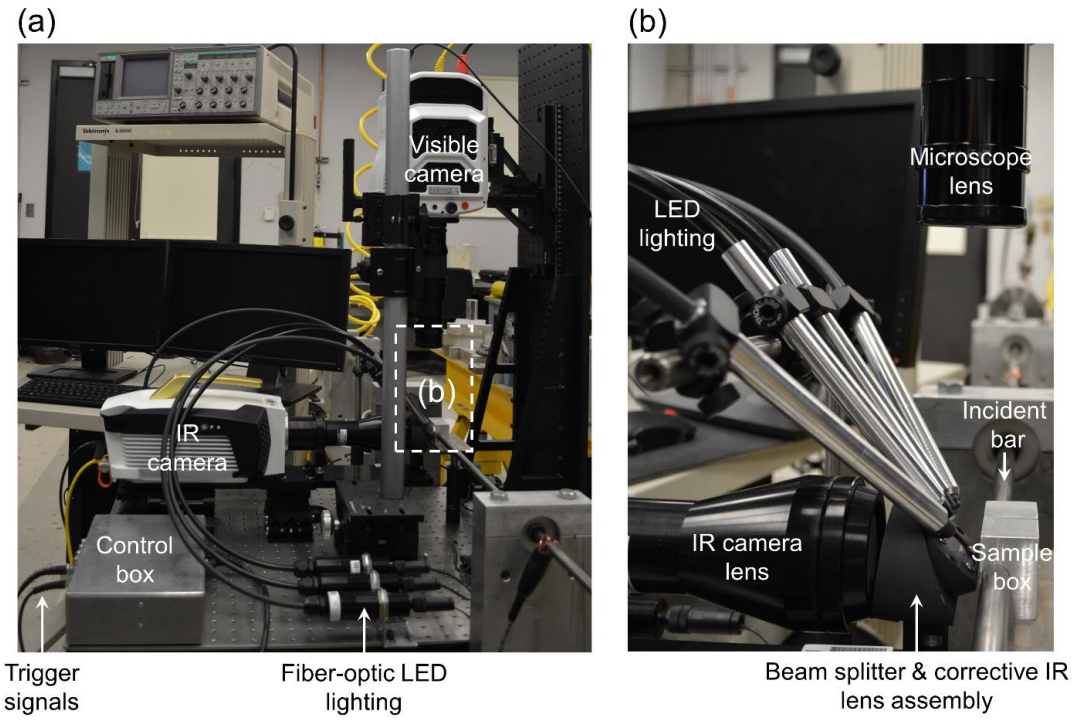

Figure 18 – Pictures of the MINTED experimental system; (a) overall view of the components, and (b) close-up view of the dichroic beam splitter, the VL and IR lenses, and LED lighting.

Selecting a proper illumination light source for high-speed imaging in this experimental layout is challenging. A sufficiently bright light source is necessary at framing rates around 100,000 fps; however, due to the high level of heat generation by a powerful light source, temperature measurements are likely to be affected. In addition, the custom-designed dichroic beam splitter-lens assembly is very close to the specimen confinement box and the sample (less than 5 mm), leaving only a very tight space for an illuminating light source. To overcome these challenges, four LED light sources along with fiber optics are used. The LED light sources are placed far from the sample, and the light is projected onto the sample through optical fibers, as shown in Figure 18. This configuration minimizes heating relative to other light sources, such as halogen lights, and permits proper placement within the tight space of the experimental setup. Figure 19 quantifies the temperature interference of three available lighting options including fiber-optic halogens, LED panels, and fiber-optic LEDs, the latter of which has the least effect

on the sample temperature. Since the system of integrated VL and IR cameras can also be used for quasi-static experiments, the temperature interference analysis of the illumination is carried out over a relatively long period of 10 minutes (Figure 19). The fiber-optic LEDs used result in a 0.2 K increase in the temperature of the sample after 10 minutes. However, for the experiments conducted, the illuminating lights are activated for only a few milliseconds; therefore, the resulting effect on temperature measurements is essentially undetectable.

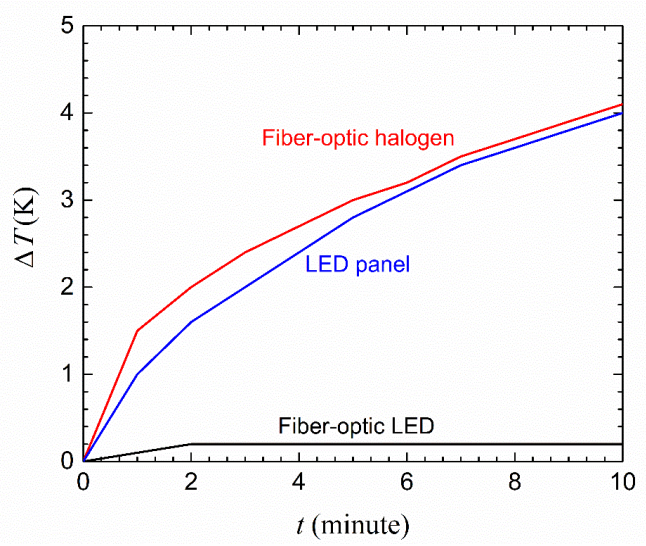

Figure 19 – Comparison of the temperature increases in a sample as a result of different lighting schemes, LED is chosen due to its negligible effect.

3.2.2 High-speed Temperature Measurements

A Telops M2k high-speed thermal imaging camera (Telops Inc., Quebec, Canada) is used to record the IR images. This camera operates at 2,000 fps with a spatial resolution of 320×256 pixels and 90,000 fps with a spatial resolution of 64×4 pixels. An IR microscope lens with the magnification factor of 2 and the working distance of 50 mm is used. The IR camera operates with an 11.6 µm spatial resolution. The IR camera is calibrated along with the IR microscope lens, the corrective IR lenses, the dichroic beam splitter, and the sapphire window. At these settings, the accuracy of the temperature

measurements is 0.5 K according to calibration data. Since the IR camera is calibrated to blackbody emission, the camera reading must be re-interpreted using the emissivity of the sample's constituents in order to arrive at the correct temperature field for real samples. The emissivity of the sample material (sucrose) is determined to be ~0.97 by calibrating the camera reading to the initial (known) temperature of the sample. The calibration is based on the Stefan-Boltzmann law in the form of

$$E = e\,\sigma T_s^4, \tag{16}$$

where E is the power flux recorded by the IR camera, e is the emissivity of the particular material constituent at a particular pixel of an image, σ is the Stefan-Boltzmann constant, and T_s is the temperature of the sample at the pixel of interest. The relation between the camera's temperature reading T_c for the pixel and the actual sample temperature T_s at the pixel is $\sigma T_c^4 = e\,\sigma T_s^4$ yielding

$$T_s = \frac{T_c}{\sqrt[4]{e}}. \tag{17}$$

This analysis assumes the emissivity remains constant during the deformation. It is believed that changes in the emissivity at low temperatures are negligible.

3.2.3 Visible and Infrared Images Synchronization in Space and Time

Figure 20 illustrates the electrical system of the experimental setup. The control box sends triggering signals to the VL and IR cameras, the oscilloscope, and the gas gun solenoids. The same reference time is required for both cameras to allow for synchronization of the VL and IR images in time. For spatial correlations of the VL and IR images, two calibration targets that can be identified by both cameras are used. The targets are visible in the VL and IR images due to differing colors and emissivity differences

between different colors. Figures 21(a) and 21(b) show the VL and IR images of a target used to measure the spatial resolutions (pixel sizes) of both cameras, respectively. To set a reference coordinate for both images, a star sector target is used and the center pixels of the FOVs of both cameras are moved to the center of the target [Figures 21(c) and 21(d)]. Using this reference coordinate and the pixel size of both the VL and IR images, the captured VL and IR images (Figure 22) are spatially synchronized for actual material samples. In general, the IR images are not as sharp as the VL images.

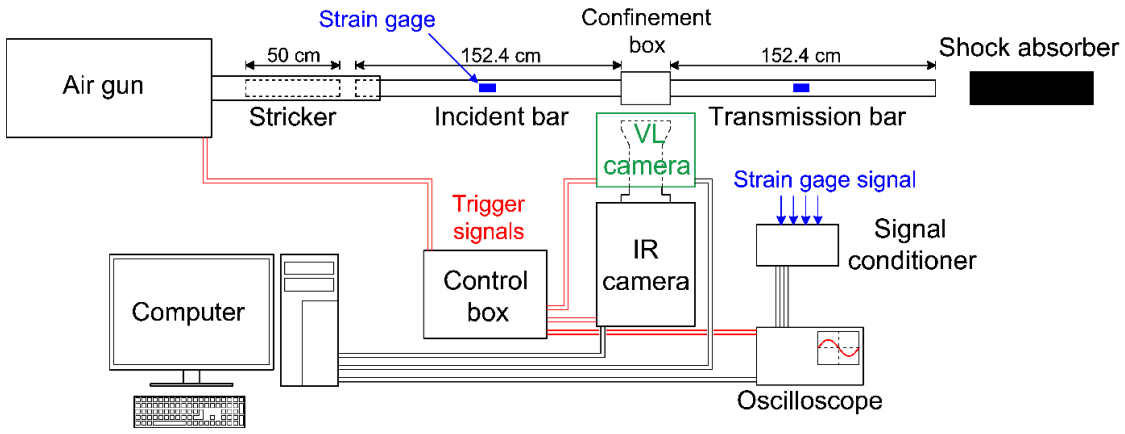

Figure 20 – Schematic illustration of electrical and control devices.

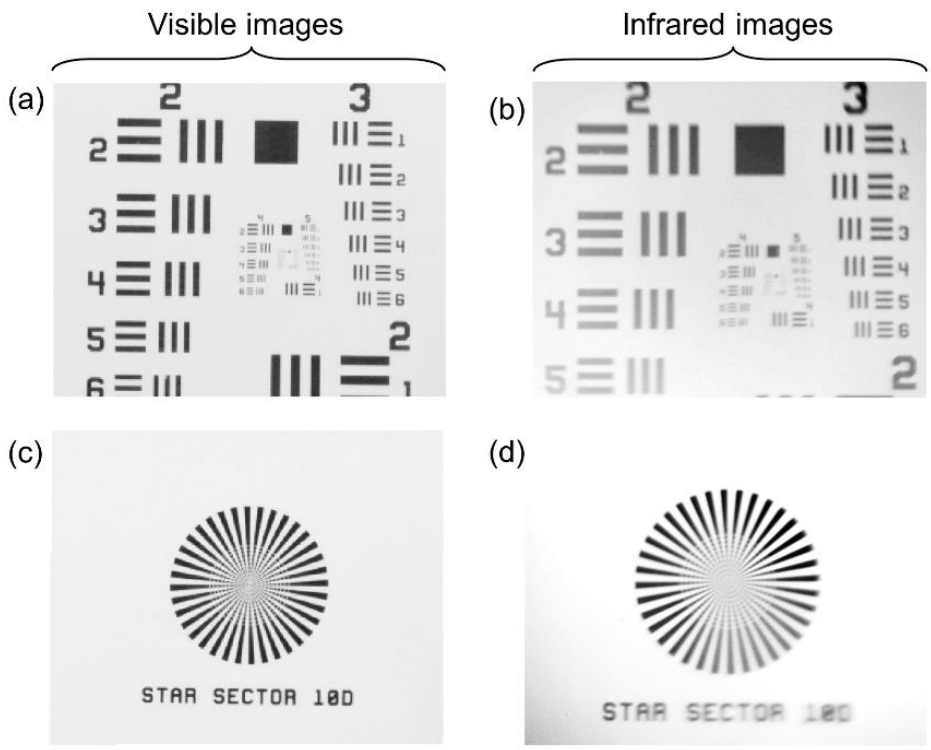

Figure 21 – (a) and (b): visible and infrared images of a target for resolution determination, respectively. (c) and (d): visible and infrared images of a star sector target for alignment, respectively. The resolution of all images is 320×256 pixels.

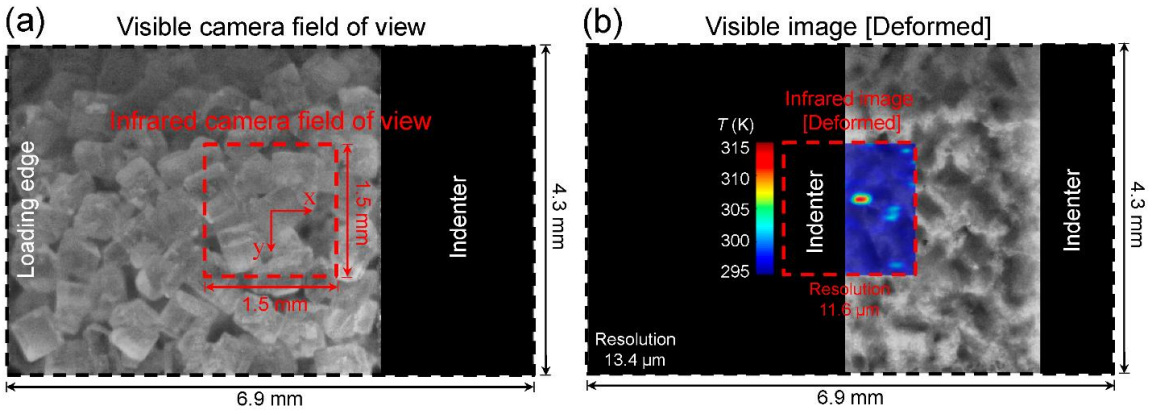

Figure 22 – Relative positions of visible and infrared fields of view for (a) the undeformed sample and (b) the deformed sample.

3.2.4 Materials

Experiments were conducted on sucrose $\left(C_{12}H_{22}O_{11}\right)$ granules with a molecular weight of 342.3 g/mol. Sucrose is a commonly used simulant for HMX energetic crystals in impact experiments [104]. The material is purchased from Research Products International (RPI). The granules are graded using standard AASHTO sieves and three sets of samples with the average grain sizes of 165 μm, 362.5 μm, and 775 μm are selected for the experiments. Figure 23 shows the initial density and average grain size of the three sets. The deformation of the sucrose granules is crystallographically dependent. The elastic modulus of sucrose single crystals on the (100) crystallographic plane is 38 GPa and the modulus on the (001) plane is 33 GPa [105]. The onset of shear stress causing plastic deformation in sucrose grains is 1 GPa [105].

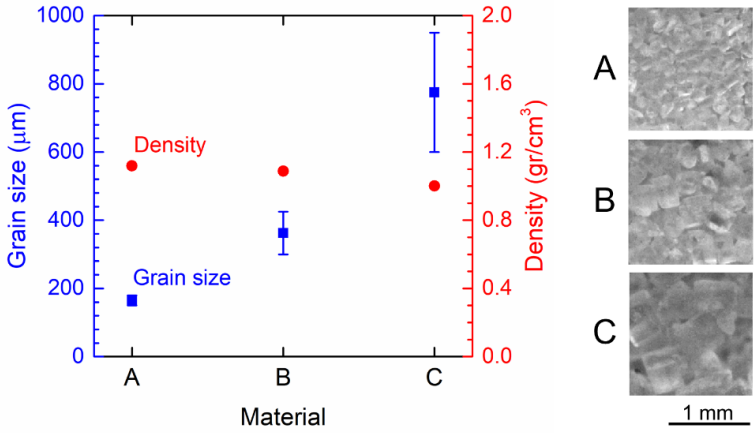

Figure 23 – Initial grain size and density of materials.

3.2.5 Loading Configurations

A classic compression split-Hopkinson bar (SHPB) or Kolsky bar setup is used for the dynamic compression of the samples as discussed below. The striker (projectile), and incident and transmission bars are made from the C350 maraging steel with a density of

$\rho = 7800$ Kg/m^3 and a Young's modulus of $E = 210$ GPa, yielding a bar wave speed of $c = \sqrt{E/\rho} = 5188$ m/s. The length of the striker is $L_{st} = 50$ cm. With this configuration, the duration of the generated compressive pulse in the incident bar is $\tau = 2L_{st}/c = 0.2$ ms. The length and the diameter of each bar (incident and transmission) is $152.4\,\text{cm}\ (5\,\text{ft})$ and $1.27\,\text{cm}\ (0.5\,\text{in})$, respectively.

The Sucrose grains are confined in a box with a sapphire window. Loading is through two indenters, as illustrated in Figure 24. The internal dimensions of the confinement box are $5\times7\times5$ mm. The confinement box is designed such that the ends of the incident bar and the transmission bar are placed inside the indenters (not visible). This design prevents lateral movements of the confinement box and the sample relative to the lenses in order to ensure the safety of the optics and in order to maintain the focal distance between the sample and the lenses necessary for capturing sharp images. The relative positions of the confinement box, the incident bar, and the transmission bar are shown in Figure 17(b). The maximum overall strain rate in the experiments carried out is 1260 ± 90 s^{-1}.

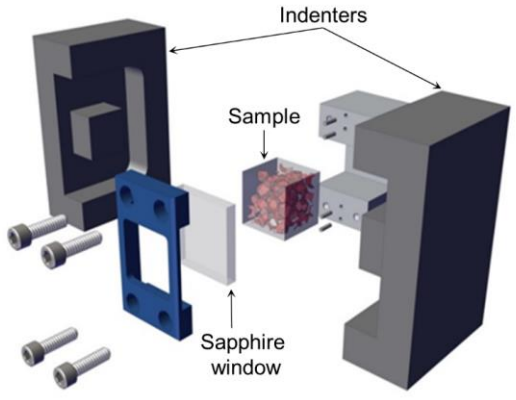

Figure 24 – Illustration of the confinement box, the sample, and the sapphire window for the compression experiments.

In a standard SHPB apparatus, the overall stress, strain and strain rates in the sample can be calculated using the signals obtained by strain gages mounted on the bars. A requirement for this calculation is that the sample is relatively small and wave reverberations due to impedance mismatch between the bars and the sample are equilibrated quickly. In this work, the confinement box causes the wave reverberations to be more significant relative to cases without the confinement box. As such the standard calculations are less accurate. In this chapter, the overall strain and strain rate in the samples are calculated based on the relative distance of the indenters (engineering strain, $\Delta L/L_0$, where $L_0 = 5\,\text{mm}$ is the initial length of the sample in the loading direction). The relative distance between the indenters are obtained from the VL images. This is more accurate than using the bar signals.

3.3 Results and Discussion

The experiments here focus on the evaluation of the capabilities of the developed MINTED system. The three materials are subjected to loading under the conditions discussed above. The recorded images are computationally analyzed. The temperature fields reported here reflect interpretation accounting for the emissivity effect based on Eq. (17). The temperature fields are analyzed in conjunction with the deformation fields to correlate the locations of hotspots with microstructure features. Digital image correlation (DIC) analyses are carried out to obtain the strain fields for comparison with the temperature fields. The use of the three sets of samples allows the effects of grain size on the responses of the materials to be analyzed. During the experiments, the environment temperature and humidity are $296.3 \pm 0.25\,\text{K}$ and $42.9 \pm 0.8\,\%$, respectively.

3.3.1 Deformation Mechanisms

Under compression, the sucrose grains are fractured and smaller crushed particles hold together and form a coherent compact, in what is known as the briquetting process. Sucrose has a high level of briquetting tendency under compression, unlike other organic materials such as coal and sodium chloride [106]. Figure 25 shows an SEM image of material C $\left(\bar{d}_0 = 775\,\mu\text{m}\right)$ after the experiment. This figure shows that some grains have sizes similar to the sizes of the initial grains, suggesting that these grains may not have fractured under loading. This figure also provides visual evidence of briquetting. Micro densification is important for achieving sufficient areas of contact between the particles in a compact in order for the whole sample to remain coherent after the pressure is released (i.e., briquetting). Although organic particles such as sodium chloride, coal, and sucrose are known to be brittle [107], these materials behave plastically if they are small and subjected to high levels of compressive stress [108]. The critical size of a particle for transition from fragmentation to plastic deformation is uncertain and varies over a considerable range of factors.

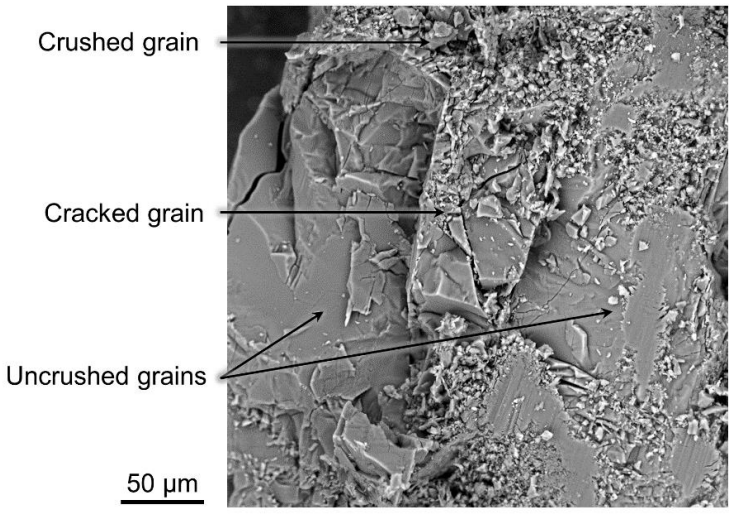

Figure 25 – SEM image of material C after the experiment.

Figure 26 shows the stages of overall deformation (engineering strain, $\Delta L/L_0$, where $L_0 = 5$ mm is the initial length of the sample in the loading direction) in the materials as a function of time during the experiments. The overall strain in the sample is calculated using the relative positions of the indenters recorded in the VL images. Three stages are observed: (1) fragmentation of grains $(0 \le t < 0.56 \text{ ms})$, (2) briquetting $(0.56 \le t < 1.18 \text{ ms})$, and (3) unloading $(t \ge 1.18 \text{ ms})$. The three materials show similar deformation trends; therefore, material C is mainly discussed in this section. Figure 26 also shows the times of the infrared images captured at a rate of one frame for every twenty visible images based on the framing rates of the two cameras. In addition, this figure denotes the infrared images with and without temperature increase.

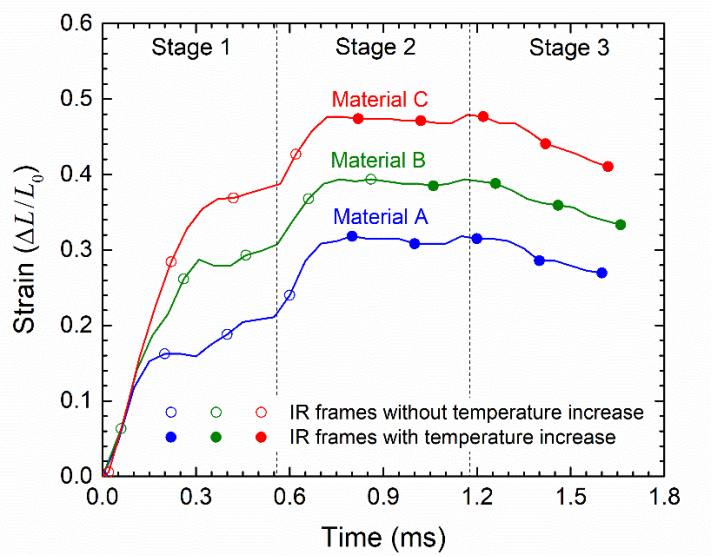

Figure 26 – Overall strain in the material as a function of time. The solid and hollow circles show the temperature frames with and without temperature increase, respectively.

In the first stage of deformation $(0 \le t < 0.56 \text{ ms})$, material C (sieve 30) is compressed by 38% and inter-granular void collapse occurs, as shown in Figure 27. Fine grains $(d \le 50 \text{ μm})$ resulting from fragmentation flow between large grains $(d \ge 250 \text{ μm})$

and fill the voids in between. The filled voids do not experience as extensive deformation as unfilled voids. In this stage, the IR camera captures two infrared images and neither shows appreciable temperature increase. In the second stage of deformation $\left(0.56 \le t < 1.18 \text{ ms}\right)$, the material is further compressed by 10% and unlike in the first stage, a limited amount of fragmentation is observed. Four IR images are captured in this stage, with the latter two images showing increases in temperature inside the material. In the last stage $\left(t \ge 1.18 \text{ ms}\right)$, partial unloading occurs as the overall strain decreases from 47.1% to 41.2%. The two IR images associated with the third stage show significant temperature increase in the material.

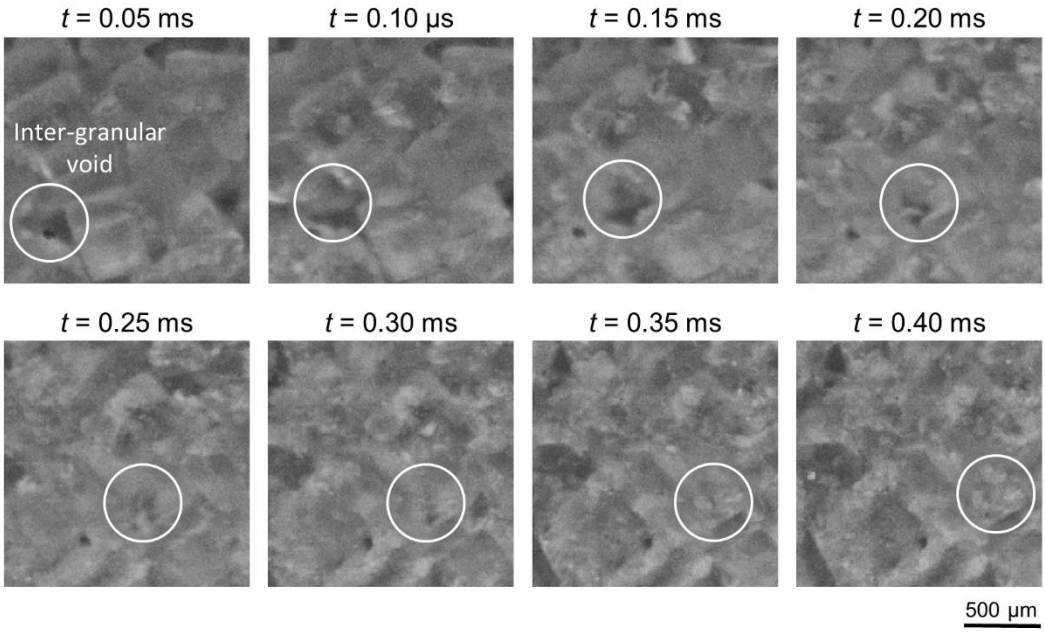

Figure 27 – Visible image sequence of inter-granular void collapse (material C).

3.3.2 Temperature Fields

The two major heating mechanisms in the materials are plastic deformation and friction. Sucrose is known to be brittle in general, but can deform plastically if the grains are small and high levels of compressive stresses are present. According to our

observations, grain fragmentation in the first stage does not directly lead to heat generation; however, fragmentations affect heat generation by facilitating inelastic deformation and, more importantly, localized frictional heating along fragmented faces.

Experimentally, it is challenging to quantify the contribution of each underlying mechanism to the formation of hotspots. However, the simultaneous visible and infrared images allow the locations of the hotspots with respect to microstructure features to be identified. The localized temperature spikes or hotspots are responsible for thermal softening, thermal runaway, and ignition in energetic materials. Identification of the locations of the hotspots is important for understanding the underlying mechanisms leading to formation of the hotspots. For example, a hotspot inside a grain and far from interfacial boundaries most likely results from inelastic deformation, while a hotspot at a boundary likely results from frictional dissipation. In addition, knowledge of the potential locations of hotspots can be used to modify the local thermo-mechanical response of materials by changing the constituent and interfacial properties.

Figures 28(a-b) show a sequence of visible images and the corresponding temperature fields for material C, respectively. The first infrared image showing temperature increase is captured at $t = 0.8\ \text{ms},$ which occurs in the second stage of deformation. Due to the highly non-uniform stress distributions, some grains experience little deformation or failure. As a result, a few large grains $\left(d \geq 250\ \mu\text{m}\right)$ remain in the briquette. Inelastic deformation occurs after micro-squashing. Therefore, unfragmented or partially fragmented grains show little plastic deformation in the interior but mostly frictional heating and deformation at or near the boundaries. The boundaries of larger grains are the primary locations of hotspots, as shown in Figure 28(b), suggesting the primary role of interfacial friction in the formation of these hotspots.

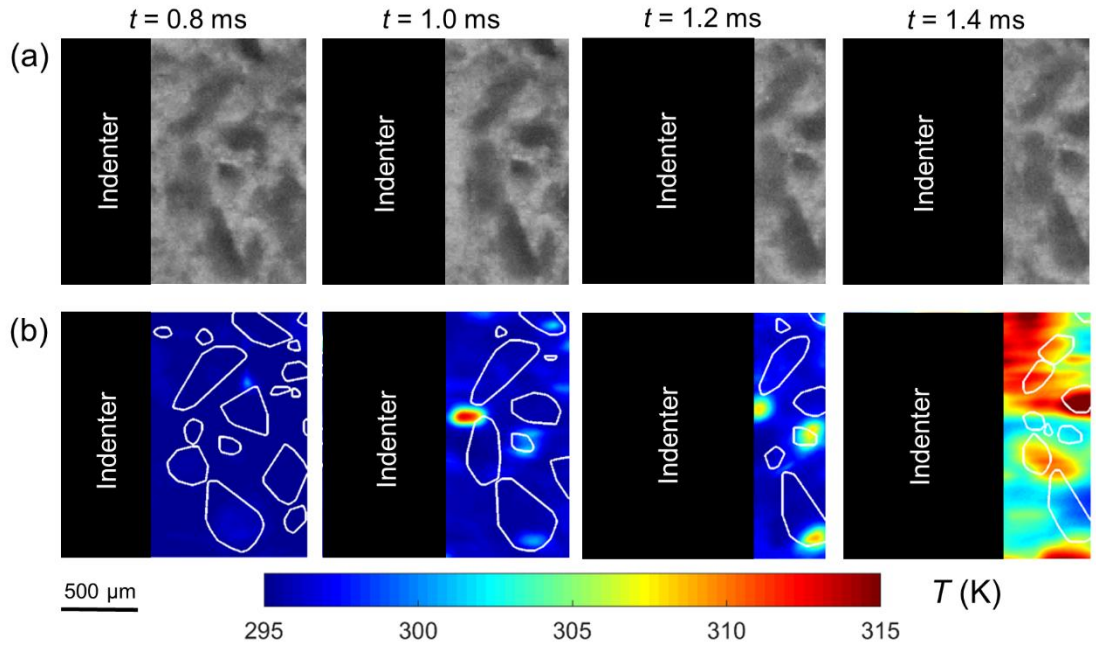

Figure 28 – Visible and infrared image sequences of material C. No temperature increase is observed for $t < 0.8$ ms.

Variations in grain size of the materials provide perturbations to the thermo-mechanical processes, causing temperature distributions to differ. Figure 29 shows the temperature distributions in the three materials at $t = 1.23$ ms. Despite the higher overall temperature levels, the temperature fields in the materials with smaller grain sizes (materials A and B) are less localized. Materials with smaller grains experience more energy dissipation, since smaller grains are more likely to undergo plastic deformation, and their high surface to volume ratios facilitate frictional dissipation. As a result, the samples with smaller initial grain sizes show higher amounts of heating and higher overall temperatures than materials with larger grain sizes. However, despite the higher amounts of overall heat generation, the materials with smaller grains have lower levels of peak temperatures. This reduction in localized heating results from two factors. First, energy dissipation from plastic deformation spreads more widely in and is less localized. Second, frictional heating is more uniformly distributed since more sites for frictional heating exist.

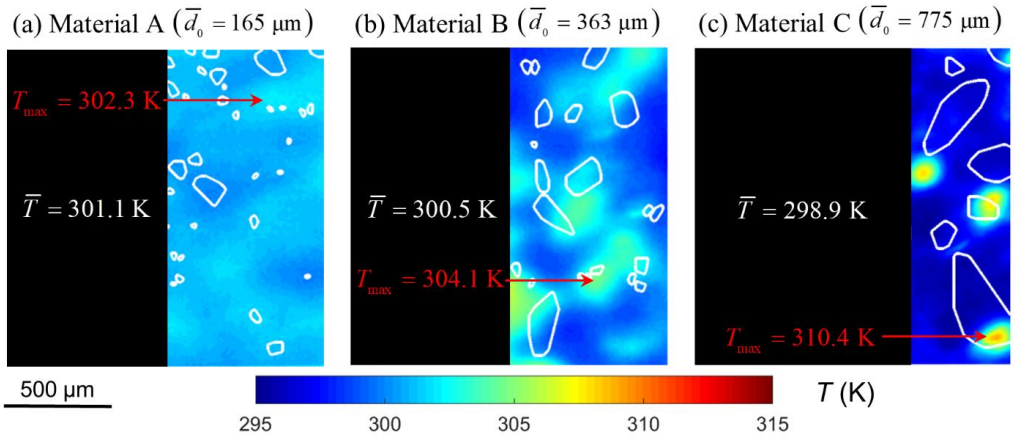

Figure 29 – Temperature fields in the materials at $t = 1.23$ ms; (a) material A, (b) material B, and (c) material C.

Figures 30(a-b) show the average temperature and the peak temperature levels of the materials. The materials with larger grain sizes have lower average temperatures but higher peak temperatures. Specifically, the difference between the average and peak temperatures in material A $\left(\bar{d}_0 = 165\,\mu\text{m}\right)$ is only 1.3 K, while the difference in material C $\left(\bar{d}_0 = 775\,\mu\text{m}\right)$ is 16.5 K. The uncertainty in temperature measurements is 0.5 K according to calibration data. The correlation between local deformation and temperature in hotspots is discussed in the next section.

3.3.3 Digital Image Correlation (DIC) Analysis of Deformation

Hotspots result from various deformation mechanisms; therefore, the deformation fields are very useful in the determination of dominant mechanisms contributing to the formation of hotspots. To obtain the strain fields, digital image correlation (DIC) analysis is performed. The analysis is carried out with the Ncorr, an open-source subset-based package with enhanced algorithms [109]. This package uses the reliability-guided digital image correlation (RG-DIC) framework [110]. Since displacements are at discrete locations, strain fields calculated directly from displacements tend to be noisy and

unreliable. To address this issue, Ncorr uses a 2D Savitzky-Golay (SG) digital differentiator based on the principle of local least-square fitting with two-dimensional polynomials [111].

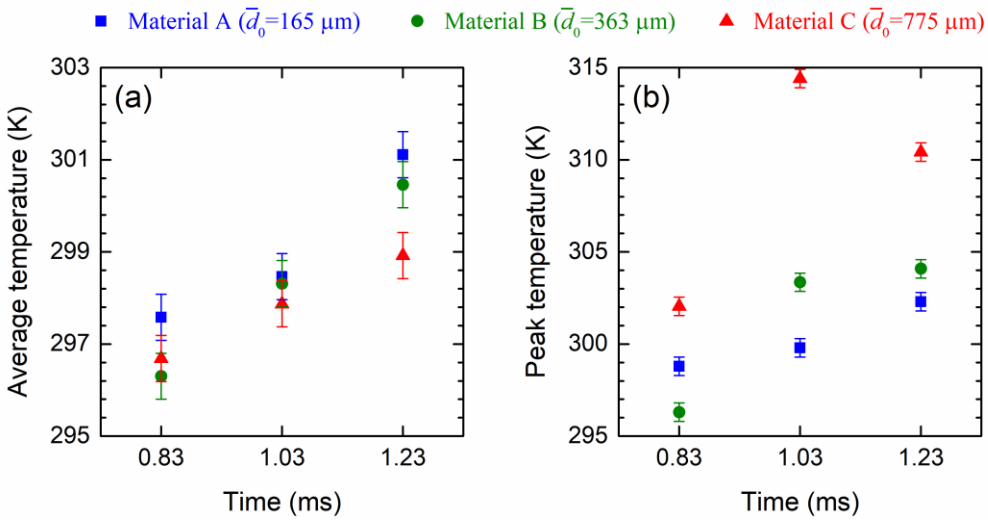

Figure 30 – (a) Average temperature levels in the materials and (b) peak temperature levels in the materials as functions of time. At $t = 0.83\,\text{ms}$, material B $\left(\bar{d}_0 = 363\,\mu\text{m}\right)$ is at the initial temperature state. The error bars show the uncertainty in temperature measurements.

DIC analysis assumes displacement continuity in the region of interest (ROI) where the correlation is performed. The incorporation of discontinuities in DIC analyses is an open problem in the literature. For the cases when the discontinuity path is known, the displacement field on each side of the discontinuity can be analyzed separately [112]. A potential drawback of this approach is that the displacements at or near the discontinuities/interfaces cannot be calculated directly. A DIC analysis is even more complex and less reliable when arbitrary crack initiation sites and propagation paths exist. Because of these reasons and the significant fragmentation in the first stage of deformation, the DIC analysis is only performed for the second stage of deformation when the material is briquetted. Therefore, the obtained strain fields from the DIC analysis are not representative of the total deformation from the very beginning of loading. In general, out-

of-plane movements of grains are unavoidable and these movements partially degrade the DIC results. Out-of-plane movements of grains are restricted during the second stage as a result of briquetting. After briquetting, the sample has planar surfaces. These surfaces remain planar during the deformation process as a result of confinement. For confined compacted sugar samples, Forsberg and Siviour (2009) performed 2D-DIC and 3D digital volume correlation (DVC), and showed that the results of 2D and 3D analysis are very close [113]. To estimate the distortion levels of IR and VL images, distortion targets were used. These targets consist of arrangement of identical speckles with known distances. The long-distance microscope lenses used for the IR and VL imaging showed negligible levels of distortion.

Figure 31 shows the reference image, the final image, and the subset size with respect to the microstructure for the DIC analysis. The natural pattern of the briquette is used for the DIC analysis [113]. To compensate for the lack of a speckle pattern, a large circular subset with a diameter of 50 pixels $(0.67\ \text{mm})$ and a total number of 1964 pixels is used. The subset size is large enough to circumscribe the largest grain in the reference image [see Figure 31(a)]. In the second stage, the average stain rate is $153\ \text{s}^{-1}$ and the maximum strain rate is $697\ \text{s}^{-1}$ which occurs at the beginning of this stage. Therefore, with a temporal resolution of $10\ \mu\text{s}$, the average strain increase between successive frames is 1.5×10^{-3} and the maximum strain increase between successive frames is 7×10^{-3} which occurs only for the first few frames.

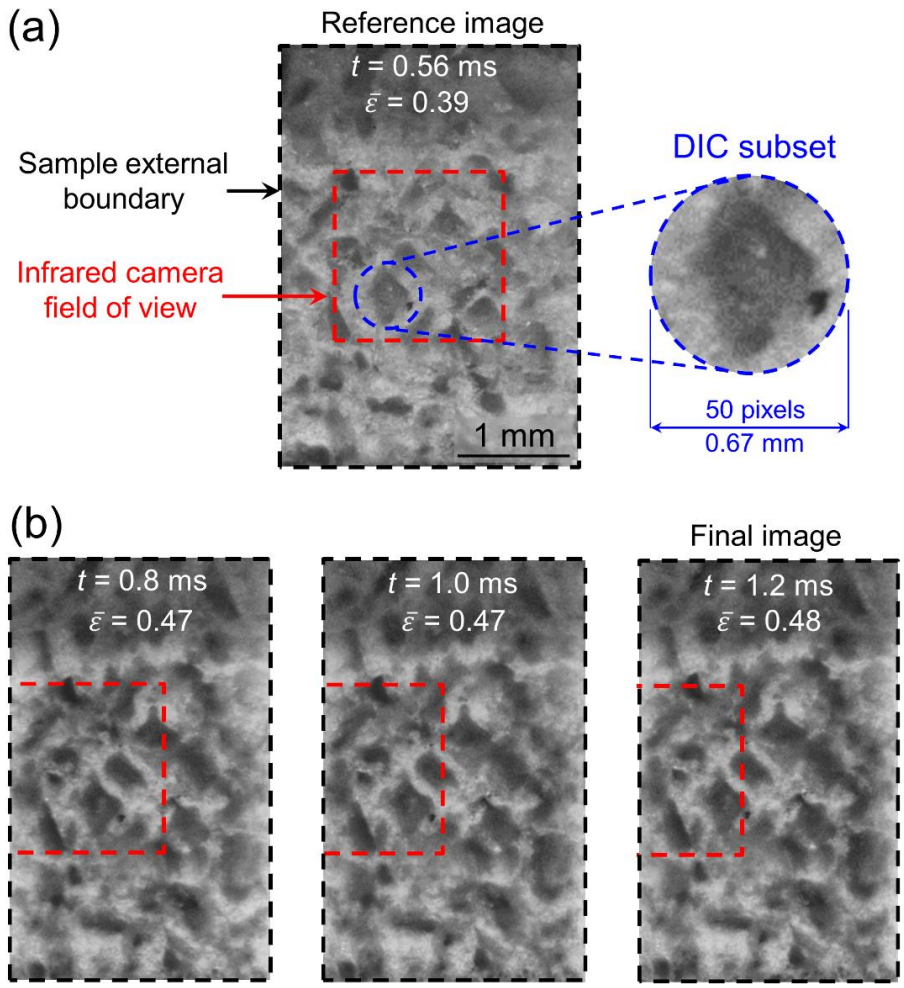

Figure 31 – (a) The reference image and the subset size, and (b) 2 out of the 63 intermediate frames and the final image used for the DIC analysis. The black dash line shows the external boundaries of the sample and the red dash line shows the FOV of the IR camera.

Figure 32 shows the temperature and Almansi strain fields of material C at $t = 1.0$ and 1.2 ms. The Almansi strain tensor is defined through

$$\boldsymbol{\varepsilon} = \frac{1}{2}\left(\mathbf{I} - \mathbf{F}^{-T}\mathbf{F}^{-1}\right), \tag{18}$$

where $\mathbf{I}$ and $\mathbf{F}$ are the second-order identity and the deformation gradient tensors, respectively. The superscripts "$-T$" and "-1" denote the inverse transpose and inverse of tensors, respectively. The strain fields show the local deformation in the sample from the

beginning of the second stage of deformation $(t = 0.56\ \text{ms})$. Therefore, these strain fields are not representative of the total deformation in the sample since the very beginning of loading. Since the temperature of the material does not begin to increase appreciably until the latter part of the second stage of deformation, the deformation mechanisms involved in the second stage are primarily responsible for the temperature increase in the material. The strain fields indicate highly heterogeneous deformation. The normal strains show regions of instantaneous expansion and contraction in both axial directions. The shear strains show vertices or shear in both the clockwise and counterclockwise directions. These features are consistent with the flow of granular materials.

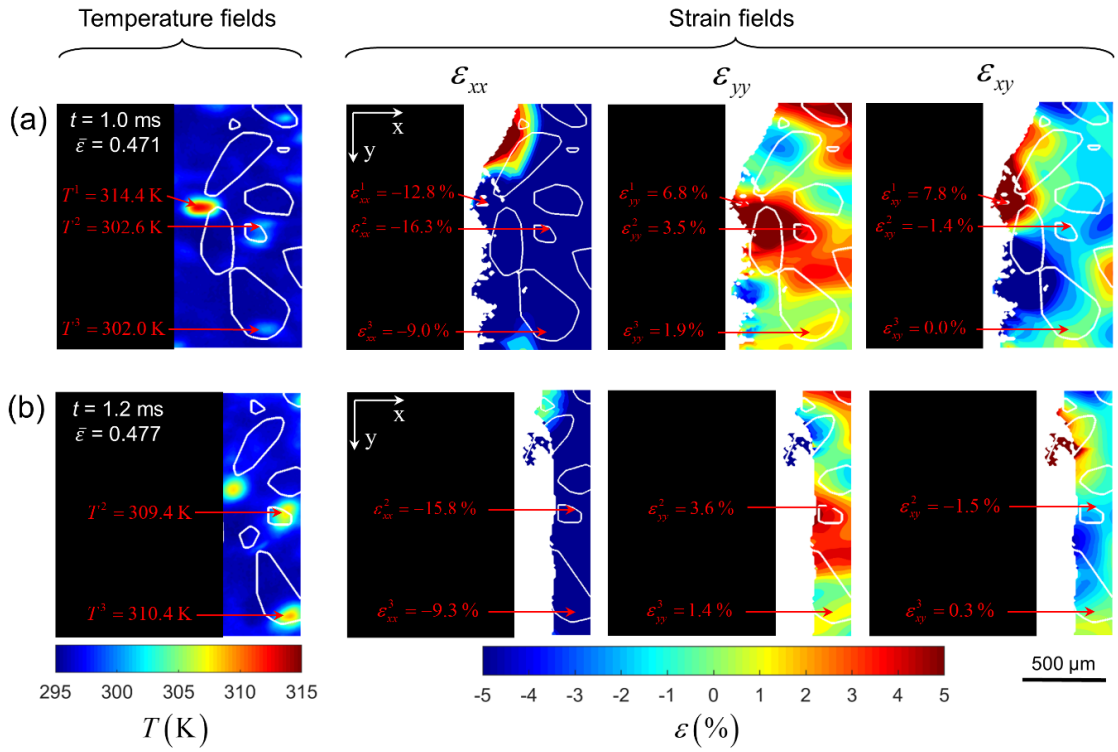

Figure 32 – Temperature and strain fields for material C; (a) $t = 1.0$ ms, and (b) $t = 1.2$ ms. These strain fields show the local deformation in the sample from the begining of the second stage of deformation $(t = 0.56\ \text{ms})$.

3.3.4 Correlation Between Deformation and Temperature in Hotspots

With the VL and IR image sequences, the unique MINTED capability allows the determination and tracing of the trajectories of hotspots or material points with respect to the microstructure. To achieve this, the VL and IR images are first spatially and temporally synchronized. The hotspot or material point $\mathbf{X}_i$ has position $\mathbf{x}_i = \mathbf{x}_i\left(\mathbf{X}_i, t\right)$ at time t. This position is obtained by solving the for $\mathbf{x}_i$ in the form of

$$\mathbf{x}_i = \mathbf{X}_i + \mathbf{u}\left(\mathbf{x}_i, t\right), \tag{19}$$

where $\mathbf{u}\left(\mathbf{x}_i, t\right)$ is the Eulerian displacement measured at $\mathbf{x}_i$ at t. Figure 32(a) shows three hotspots in the sample at $t = 1.0$ ms and the corresponding local strains. Two of these hotspots are traced and their temperatures and local strains are captured at $t = 1.2$ ms [Figure 32(b)].

Although the overall strain essentially ceases to evolve in the second half of the second stage of deformation, a fraction of the input work stored in the sample dissipates over time, causing local deformation to continue and temperature to increase further. As evidence, Figure 32 compares the temperature and strains of two hotspots $\left(\text{denoted with } T^2 \text{ and } T^3\right)$ at $t = 1.0$ and 1.2 ms, when the overall strain of the sample remains constant $\left(\bar{\varepsilon} \cong 0.47\right)$. The temperature increases in the two hotspots from $t = 1.0$ ms to $t = 1.2$ ms are accompanied by increases in the local shear strain $\left(\varepsilon_{xy}\right)$ in the hotspots. Specifically, the 8.4 K increase in the temperature of hotspot 3 (labeled with T^3 in Figure 32) is associated with a ~0.3% increase in ε_{xy}.

Figure 33(a) quantifies the number and average area of hotspots whose interior temperatures are above or at temperature T in Figure 32(b). Figure 33(b) quantifies the

deformation modes (volumetric and maximum shear strains) for the hotspots in Figure 32(b). The two major heating mechanisms in the materials are plastic deformation and friction, both of which result from shear deformation beyond certain limits. It is challenging to separate the contributions of the two mechanisms without additional information. Both volumetric strain and maximum shear strain levels are higher in the hotspots with higher temperatures and the shear deformation is more pronounced in the hotspots. The results show a direct correlation between maximum shear strain and temperature levels in hotspots.

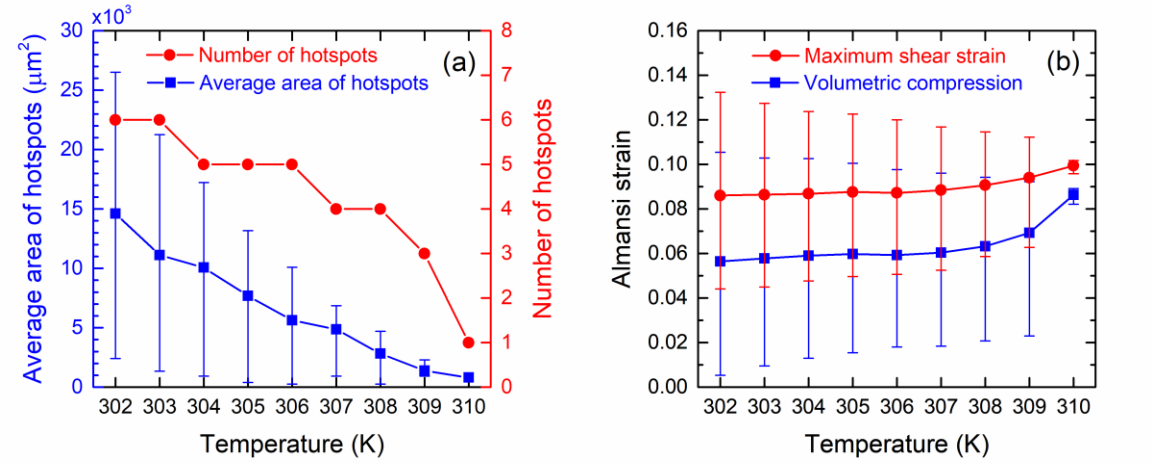

Figure 33 – (a) Number and average area of hotspots whose interior temperatures are above or at temperature *T*, and (b) local volumetric and maximum shear Almansi strains in hotspots as functions of hotspot temperature for material C at $t = 1.2$ ms [Figure 32(b)].

3.3.5 Effect of Subset Size on Computation of Local Deformation Levels

Proper selection of subset size relative to the length-scale of physical features is important in DIC analyses. Smaller subsets yield better resolutions for small-scale features while larger subsets cause more averaging and may be appropriate for larger-scale features. Results obtained from smaller subsets contain higher levels of noise that may obscure small-scale physical features. Large subsets reduce noise levels but may not allow capture

of small-scale physics. In addition, a subset needs to be large enough to track an arrangement of speckles/features in order to perform correlation. In the experiments here, the natural pattern of the briquetted sample is used for the DIC analysis. To compensate for the lack of a speckle pattern, the subset needs to be large enough to capture boundaries of grains in order to calculate the deformation fields inside grains. Therefore, a large circular subset with a diameter of 0.67 mm (50 pixels) that circumscribes the largest grain in the sample is used [see Figure 31(a)].

Hotspots are important physical features in the experiments performed here. Hotspot 2 (labeled with T^2 in Figure 32) is at the boundary of a small grain with a size of 0.173 mm next to another grain with a size of 0.3 mm. Therefore, a good correlation can be achieved even with subset sizes smaller than 0.67 mm (50 pixels) for the neighborhood of hotspot 2. Figure 34 shows the strain components associated with hotspot 2 at $t = 1.0$ and 1.2 ms for subset sizes 0.4 – 0.94 mm $(30 - 70$ pixels$)$. The smallest subset with a size of 0.4 mm (30 pixels) yields the highest level of ε_{xy} but the lowest levels of ε_{xx} and ε_{yy} in hotspot 2. As the subset size increases to 0.94 mm (70 pixels), ε_{xy} decreases and the normal strains $\left(\text{i.e., } \varepsilon_{xx} \text{ and } \varepsilon_{yy}\right)$ reach constant levels. The increase in ε_{xy} with decreasing the subset size shows that the shear deformation is more localized. Since this localized deformation occurred at a grain boundary, this shear deformation results from friction. In addition, the increase in ε_{xy} associated with the 6.4 K increase in the temperature of hotspot 2 from $t = 1.0$ ms to $t = 1.2$ ms is perspicuous with small subsets. Specifically, the increase in ε_{xy} from $t = 1.0$ ms to $t = 1.2$ ms is 1.4% for the subset size of 0.4 mm (30 pixels) while the increase is only 0.1% for the subset size of 0.64 mm (50 pixels).

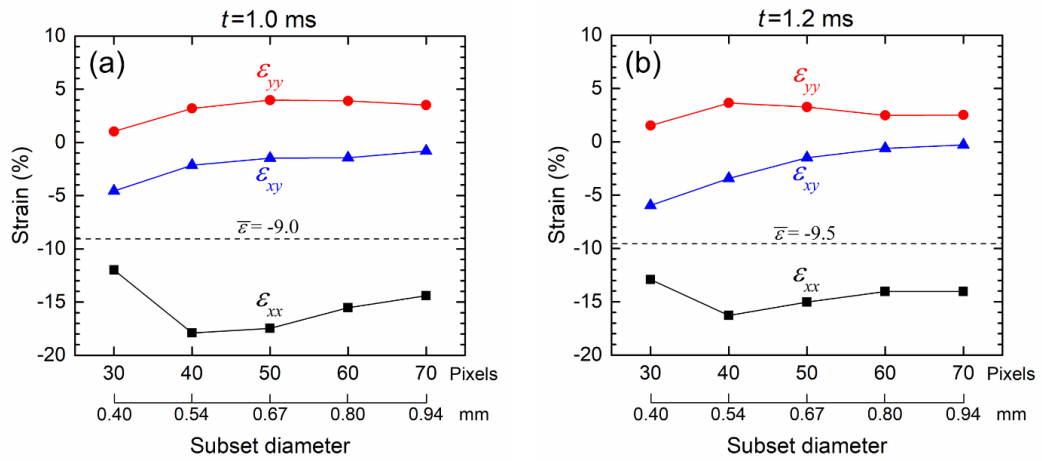

Figure 34 – Variations in local strains (ε_{xx}, ε_{yy}, and ε_{xy}) inside hotspot 2 (labeled with T^2 in Figure 32) during the second stage of deformation as a function of subset size; (a) $t = 1.0$ ms, and (b) $t = 1.2$ ms. Here, $\bar{\varepsilon}$ denotes the overall strain occurred in the sample during the second stage of deformation.

3.4 Summary

A novel capability (**MINTED**, or **m**icroscale **in**-situ imaging of **te**mperature and **d**eformation fields under dynamic loading) for time-resolved and space-resolved measurements of the temperature and deformation fields at the microstructure level for dynamic conditions is developed. The method integrates a state-of-the-art high-speed infrared (IR) camera and a high-speed visible light (VL) camera in a split-Hopkinson pressure bar (SHPB) or Kolsky bar apparatus. To simultaneously capture deformation and temperature fields at normal incidence, the visible (VL) and infrared (IR) emissions from the sample are separated by a dichroic beam splitter. The beam splitter reflects VL light and directs the light into the VL camera. This is a general capability that can be used to study deformation, failure and heating in a range of materials, including metals, composites, ceramics, soft materials, and energetic materials.

To demonstrate the capabilities of the MINTED system, experiments were performed on sucrose granules, which are widely used as a simulant of energetic crystals. The experiments involve three sucrose materials with the average grain sizes of 165 μm, 362.5 μm, and 775 μm. The samples are confined in a box behind a sapphire window. Under loading, the grains are fragmented, squashed, and briquetted. The materials undergo significant temperature increases in the briquetting stage. Despite higher overall temperature levels, the temperature fields in the materials with smaller grain sizes are less localized. The unique capability here for simultaneous measurements of deformation and temperature fields allows the determination and tracing of the locations of hotspots or material points with respect to the material microstructure features. The results show that the boundaries of unfragmented grains are the primary locations of hotspots. The maximum shear strain levels are locally higher than volumetric strain levels in the hotspots, and there is a direct correlation between maximum shear strain and temperature levels in hotspots.

CHAPTER 4. DEFORMATION MODES AND TEMPERATURE SIGNATURES IN AMEM SIMULANT

4.1 Introduction

Unidirectionally printed materials show overall transversely isotropic behavior with the print (filament) direction as the anisotropic axis. In addition, these materials show orientation-dependent failure behavior. Hong et al. tested UV-cured AM photopolymers and reported that the tensile toughness level parallel to the filaments is approximately two times higher than the toughness level perpendicular to the filaments [114]. Therefore, it is necessary to account for anisotropic failure in modeling of AM photopolymers. Based on isotropic hyperelastic and viscoplastic models for polymers [115], Zhang and To proposed a transversely isotropic continuum model for additively manufactured photopolymers [116]. This model applies to the macro-scale behavior of AM photopolymers. However, to understand meso-scale thermo-mechanical response of AMEMs, it is necessary to explicitly account for microstructure morphology and heterogeneities at lower size scales.

The focus here is the mesoscale thermo-mechanical responses under impact loading of a high solid-loaded photopolymer manufactured using the DIW process and cured with UV-light. The material mimics the attributes of some AMEMs. Samples are extracted from a single DIW block and subjected to loading along four different directions. The experiments are performed in a SHPB or Kolsky bar apparatus at the average strain rate of ~313.4 s^{-1}, with the novel capability for simultaneous measurement of the temperature and deformation fields presented in Chapter 3. The technique involves the use of digital image

correlation (DIC) for displacement and strain distribution quantification. The deformation and temperature fields are coordinated to obtain understanding of the deformation, failure, and heating mechanisms in the material at the mesoscale. To quantify the complex physics observed in the experiments and their interplays, finite element simulations are performed accounting for the geometry and microstructure morphology of the samples used in the experiments. The simulations account for finite-strain inelastic deformation, arbitrary crack initiation and propagation, contact and friction at crack surfaces, inelastic and frictional heat generation, and heat conduction. Most material constitutive parameters are obtained from independent experiments or determined using experimental data in the literature.

4.2 Technical Approach

4.2.1 Material and Microstructure

The additively manufactured energetic material (AMEM) simulant blocks were fabricated using direct ink writing at the Air Force Research Laboratory, Eglin Air Force Base. The ink contained approximately 74% solid particulate by volume with the remainder being a UV-initiated methacrylate binder (26% by vol) that results in a particulate-reinforced polymeric composite upon curing. The solid particles are comprised of four distinct populations, two organic and two inorganic in nature, with average diameters in the range of 30 – 100 μm. The morphologies of the particles vary from smooth spheres to jagged, rough prisms. The ink was extruded through a 1.6 mm diameter nozzle with a layer height of 1.5 mm.

Figure 35 shows the external structure of a material block. The tomographic images of three sections of the block show internal defects in the forms of voids and debonding sites. Figure 36(a) shows a three-dimensional view of the voids in this block. The overall volume fraction of voids in the material block is 2%. The size and shape of the voids are characterized using the actual volume and the bounding box of each void. The shapes of two such voids are shown in Figure 36(b). Figure 36(c) shows the density distributions of the three linear dimensions of the bounding boxes in the x, y, and z directions. The density distributions of the aspect ratios are shown in Figure 36(d). The defects are elongated in the y (print or filament) direction and are relatively flattened in the z (build) direction. The mechanical properties the primary orientations are obtained from quasi-static tests and listed in Table 6.

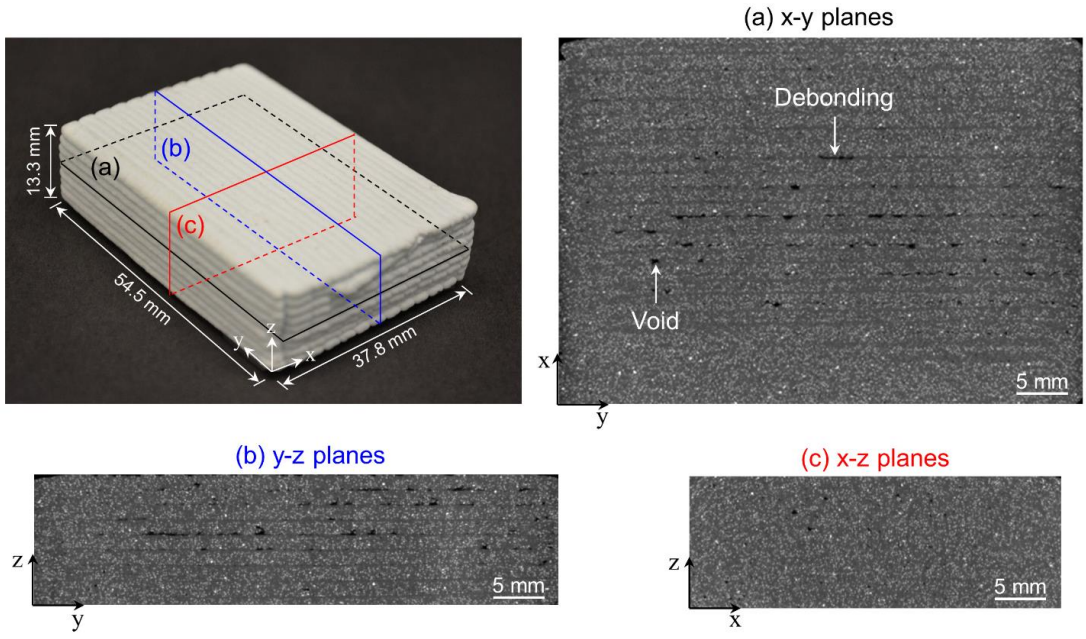

Figure 35 – External structure of a material block and the tomographic images of three sections of the material block. The tomographic images show the internal defects including voids and debonding sites.

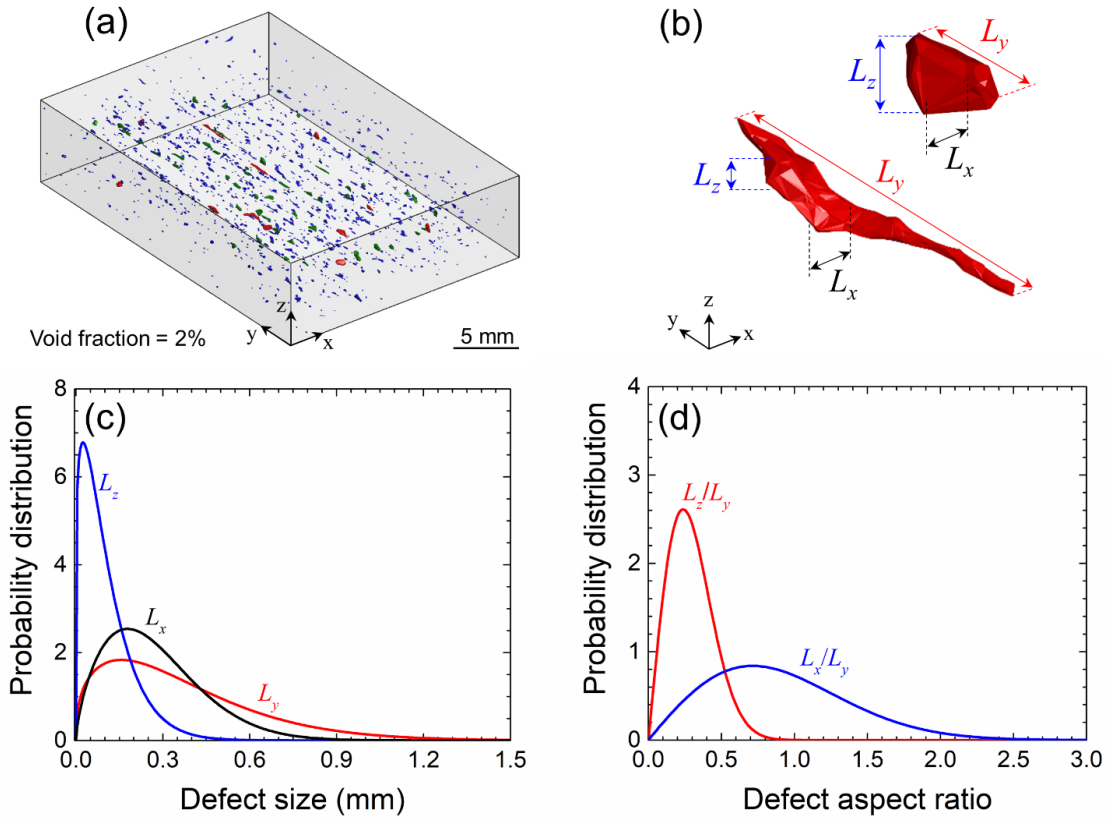

Figure 36 – (a) The distribution of voids in a 3D-printed photopolymer-solid particle composite block, (b) the shapes of two voids, (c) probability density distributions of defect sizes in the x, y, and z directions, and (d) probability density distributions of defect aspect ratios. The overall void fraction in the material is 2%.

Table 6 – Mechanical properties of the AMEM simulant in different orientations.

Loading orientation	Young's modulus (GPs)	Yield stress in compression (MPa)	Yield strain in compression (%)
Along filaments (y)	2.54±0.05	23.95±4.50	1.15±0.18
Perpendicular to filaments (x and z)	0.97±0.19	21.64±3.02	2.57±0.76

4.2.2 Integrated High-speed Visible Light and Infrared Imaging System

The MINTED system presented in Chapter 3 is used to capture the transient deformation and temperature fields over the same microstructure area of a sample with micrometer spatial and microsecond temporal resolutions. The VL images are recorded at a temporal resolution of 10 μs, a spatial resolution of 13.6 μm, and a field of view (FOV) of 7.0×4.4 mm. The IR images are captured at a temporal resolution of 300 μs, a spatial resolution of 11.4 μm, and a FOV of 2.2×2.2 mm [shown in Figure 17(c)].

Dynamic compression of the samples is achieved using a split-Hopkinson pressure bar (SHPB) with a load pulse duration of 0.2 ms and an average strain rate of ~313.4 s^{-1}. The samples are compressed without lateral confinement. Loading along 4 sample orientations relative to the AM print direction is considered. The 4 loading orientations are along the x direction, y (print or filament) direction, z (build) direction, and xy-diagonal direction. For this purpose, the samples are cut from the AM blocks accordingly at an overall size of 5×5×5 mm, as illustrated in Figure 37. The VL and IR FOVs are illustrated. The experiments are carried out at ambient temperatures and humidity levels of $23.3 \pm 1.8\,^{\circ}\mathrm{C}$ and $44.6 \pm 2.1\%$, respectively.

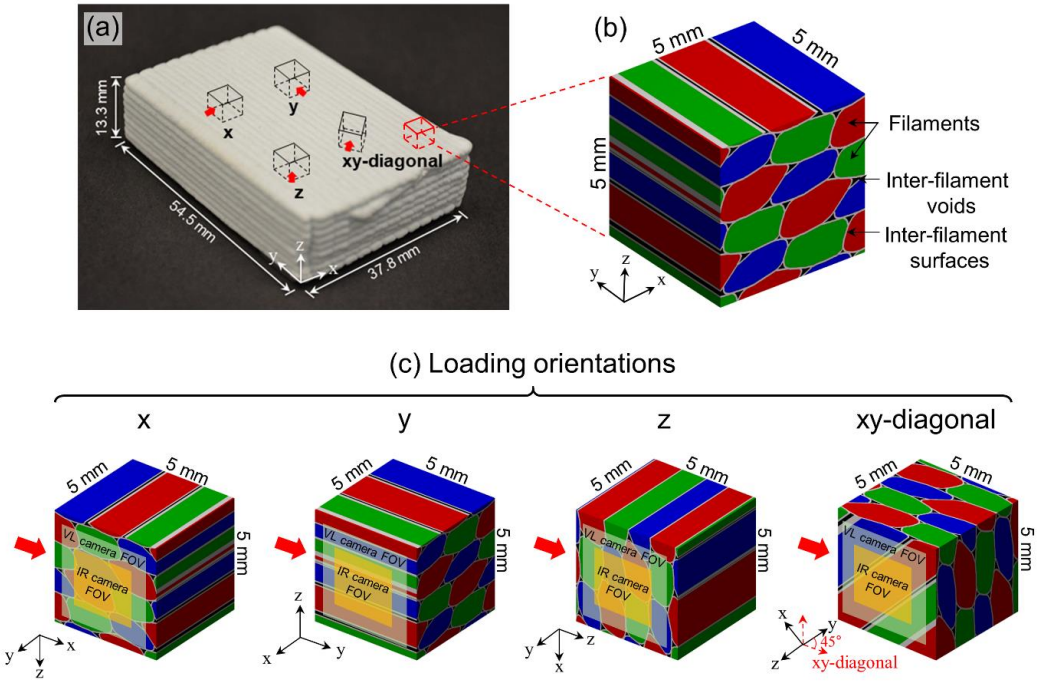

Figure 37 – Illustration of loading directions with respect to the print structure. The y and z directions are the print (filament) and build directions, respectively.

4.2.3 Digital Image Correlation (DIC) Analysis of Deformation Fields

To quantify the strain distributions in the samples, digital image correlation (DIC) analyses are performed using the open-source Ncorr package [109]. To provide characteristic patterns for the image correlation, the surfaces of the samples are sparsely sprayed with the black paint. The speckle patterns sprayed on the samples are shown in Figure 38(a). The probability density distributions of speckle dimensions are shown in Figure 38(b). The proper size of 3-6 pixels is achieved for speckles [117]. Higher densities of speckles can lead to higher resolutions for deformation fields, but cover higher fractions of sample surfaces resulting in more interference with the temperature measurement. Here, the densities of speckles are limited to $16.5 \pm 1.4\%$ [Figure 38(c)] to maintain a proper tradeoff between the deformation resolution and the temperature measurement accuracy.

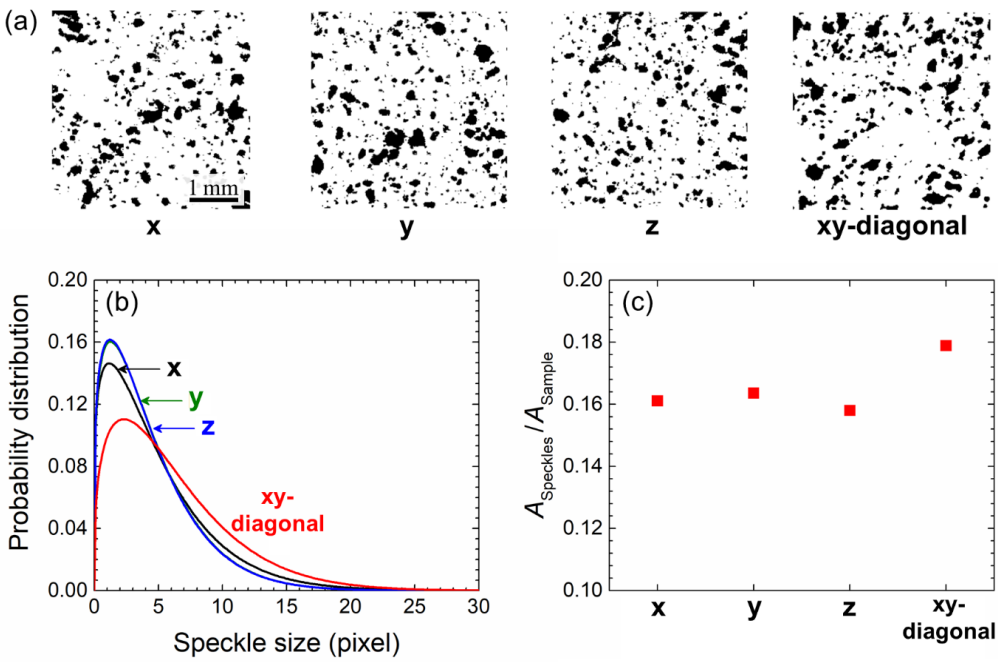

Figure 38 – (a) Speckle patterns sprayed on the samples for DIC analysis, (b) probability density distributions of the speckle dimensions, and (c) area fractions of the samples covered by the speckles.

To estimate the errors in the DIC analyses, the displacement and strain fields readings associated with known rigid translations of the samples are calculated. In this scenario, the samples are translated in the loading direction (x-direction) without deformation. Under ideal conditions, the DIC analyses should yield uniform displacement field and zero strain. Any deviation from the applied displacement and resulting strain field provide a measure for the error in the DIC analyses and associated experimental setup. Figures 39(a-b) show the probability density distributions of error in the displacement along the loading or x-direction at $x = 2$ and 4 mm, respectively. Three subset sizes of 30, 50, and 70 pixels are used. Here, the selection of subset sizes smaller than 30 pixels results in incomplete and noisy strain fields. For all selected subset sizes, the maximum displacement error is ~9 μm, which is smaller than the pixel size of 13.6 μm. Figures 39(c-

d) show the error ion the longitudinal strain, the maximum is 7×10^{-3}, associated with the smallest subset size (30 pixels). Using the subset size of 30 pixels, Figures 40(a-b) show the probability distributions of displacement error along the loading direction in the four samples. Figures 40(c-d) show the probability distributions of the error in the longitudinal strain in the four samples. The maximum error in the longitudinal strain calculations is 10^{-2}. In the analyses, a subset size of 30 pixels is used, with the uncertainty levels in the displacement and strain being 9 μm and 1%, respectively.

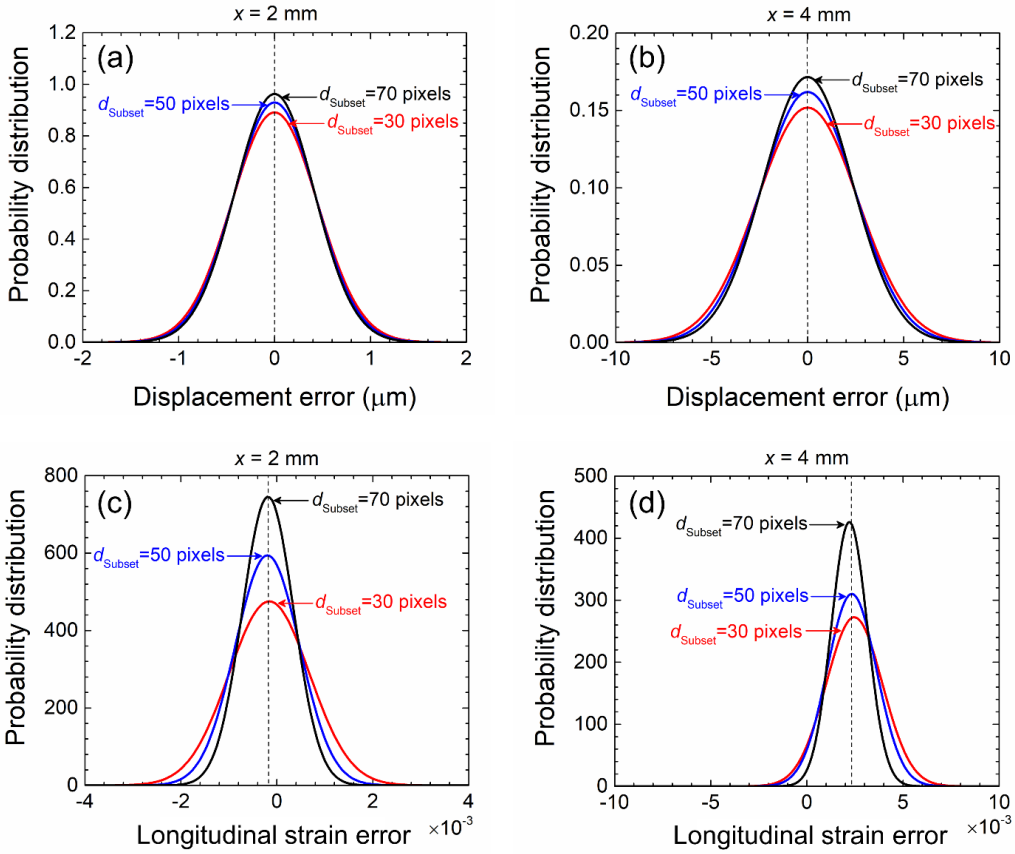

Figure 39 – Probability density distributions of the errors in the displacement and longitudinal strain obtained by rigidly translating a sample by $x = 2$ and 4 mm.

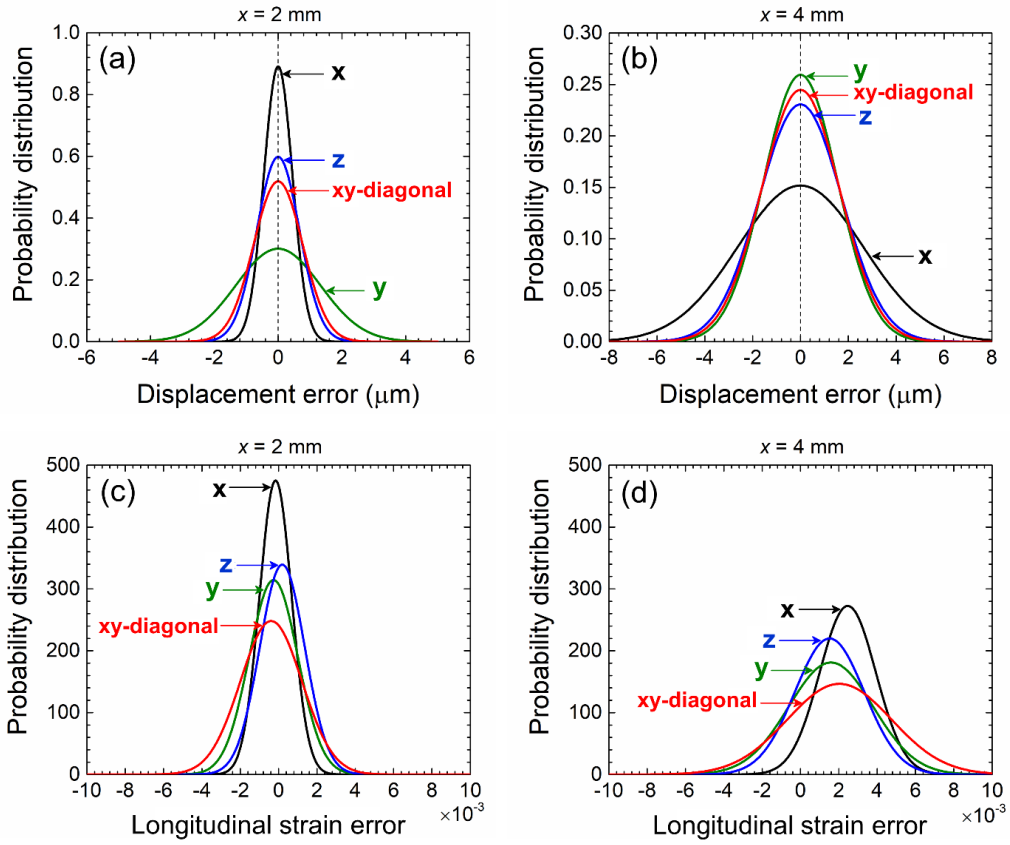

Figure 40 – Probability density distributions of the errors in the displacement and longitudinal strain calculations for different loading directions obtained by rigidly translating the samples by x = 2 and 4 mm. The subset size is 30 pixels.

4.2.4 Thermo-mechanical Computational Simulations

The experiments capture deformation modes and corresponding temperature signatures in the AMEM simulant. However, the effects of microstructural attributes and frictional and inelastic dissipation cannot be quantified experimentally due to limitations of available diagnostics. Therefore, experimentally-informed finite element simulations are also performed to gain the quantification. Microstructures are generated based on scanned images of the morphology of the 3D-printed material block. Material constitutive parameters are determined based on independent experiments or data reported in the literature. The Young's modulus and the yield strength are measured through quasi-static

tests. The equation of state (EOS) is obtained through our recent x-ray phase-contrast imaging (XPCI) experiments [118] on this material. The damage and thermal parameters are approximated to match the results of simultaneous high-speed optical and infrared images. Here, it is assumed that the filaments are homogenous elastic-plastic materials.

To account for the process-inherent heterogeneities in the material, an approach involving the use of different bulk constituents is taken. Specifically, the microstructure consists of three different constituents, one the filaments, another for the inter-filament surfaces, and a third for the inter-filament voids, as shown in Figure 37(b). Among the filaments, three groups with differing properties (as indicated by the three different colors) are used to account for random fluctuations in the overall properties of the filament material. The elastic properties of each group are selected such that the overall elastic properties at the sample level match experimental measurements in both the longitudinal and transverse directions. The determination of the three sets of properties follows the Voigt upper bound and Reuss lower bound [119], i.e.,

$$\left.\begin{aligned} \phi_L &= \sum_{i=1}^{n} v_i \phi_i \\ \phi_T &= \left[\sum_{i=1}^{n} v_i / \phi_i \right]^{-1} \end{aligned}\right\}, \tag{20}$$

where ϕ_i and v_i are the property value and the volume fraction of constituent i, respectively, and $n = 3$ accounting for the three groups of filaments, the interfaces, and the voids. ϕ_L and ϕ_T are the overall property values at the macroscale in the longitudinal and transverse orientations, respectively. Since the defects are mainly located at the inter-filament sites, they are implicitly modeled through reduction in the mass density and

degradation in the mechanical properties at the inter-filament sites [see Figure 37(b)]. A critical plastic strain criterion determines the initiation and propagation of shear failure. The onset of damage at the two-filament junctions and three-filament junctions are approximated to be two-thirds and one-third of the filaments, respectively [114].

The experiments suggest that friction can contribute significantly to the heating in the material, as the highest temperatures measured are inside shear bands where shear failure occurs. Therefore, it is important to account for frictional dissipation as well as inelastic dissipation in the simulations. Therefore, a Lagrangian framework that explicitly tracks interfaces resulting from material failure, interfacial frictional sliding, and consequent frictional heating is used. The simulations also account for finite-strain elastic-plastic deformation, strain-rate effect, inelastic heating, and heat conduction. The framework below is implemented in ABAQUS 2018 in conjunction with MATLAB, Python and FORTRAN based pre and post processors.

4.2.5 Constitutive Relations

The governing equations are balance of momentum and conservation of energy in the forms of

$$\nabla \cdot \boldsymbol{\sigma} = \rho \ddot{\mathbf{u}}, \tag{21}$$

and

$$\rho c_v \frac{\partial T}{\partial t} = k \nabla^2 T + \dot{W}^P + \dot{W}^F, \tag{22}$$

where, $\nabla = \partial/\partial x\,\mathbf{i} + \partial/\partial y\,\mathbf{j} + \partial/\partial z\,\mathbf{k}$ is the gradient operator in which ∂ denotes partial derivative, $\boldsymbol{\sigma}$ is the Cauchy stress tensor, ρ is mass density, $\ddot{\mathbf{u}}$ is the acceleration, T is temperature, c_v is specific heat and estimated to be $1500\ \mathrm{J\,kg^{-1}\,K^{-1}}$, and k is thermal conductivity. Implied in Eq. (22) is Fourier's law of conduction. $\dot{W}^P = \boldsymbol{\sigma} : \mathbf{D}^P$ and $\dot{W}^F$ are the rates of plastic work and frictional dissipation per unit volume, respectively. Here, $\mathbf{D}^p$ is the plastic part of the rate of deformation tensor. The kinematic relations for elastic-plastic deformation are presented in [47, 120].

The linear Drucker-Prager pressure-dependent (DP) model is used to determine the onset of plastic deformation [121],

$$\left.\begin{aligned} \sigma_e - \sigma_H \tan\beta - \left(1 - \frac{1}{3}\tan\beta\right)\bar{\sigma}_c = 0 \\ \tan\beta = 3\frac{m-1}{m+1} \end{aligned}\right\}, \tag{23}$$

where σ_e is the von Mises equivalent stress, $\sigma_H = \left(\sigma_{11} + \sigma_{22} + \sigma_{33}\right)/3$ is the hydrostatic stress, β is the friction angle of the material in the meridional stress plane, and $m = \sigma_c/\sigma_t$ in which σ_c and σ_t are the yield point in compression and tension, respectively. The DP model is used for polymers with $m \simeq 1.3$ [122]. The Jonson-Cook constitutive model can be used to account for the effects of strain, strain rate, and temperature on the flow stress in compression $\left(\bar{\sigma}_c\right)$ in the form of

$$\bar{\sigma}_c = \left[A + B\left(\bar{\varepsilon}^{pl}\right)^n\right]\left[1 + C\ln\left(\frac{\dot{\bar{\varepsilon}}^{pl}}{\dot{\varepsilon}_0}\right)\right]\left[1 - \left(\frac{T - T_0}{T_m - T_0}\right)^m\right], \tag{24}$$

where the first bracket represents the effect of strain hardening, the second bracket accounts for the effect of strain rate, and the last bracket denotes the effect of temperature. Here, $\bar{\varepsilon}^{pl}$ is the equivalent plastic strain, $\dot{\bar{\varepsilon}}^{pl}$ is the equivalent plastic strain rate, $\dot{\varepsilon}_0$ is the reference strain rate, T is temperature, T_0 is the reference temperature, and T_m is the melting temperature. *A*, *B*, *C*, *n*, and *m* are material parameters. In this study, the effects of strain hardening and temperature are not considered since the material shows negligible temperature increases and no strain hardening $\left(B=0, T\approx T_0\right)$. Under this condition, $A=\sigma_c$ which is the yield strength in compression corresponding to the reference strain rate $\dot{\varepsilon}_0$, and $C=0.005$ based on a qualitative comparison of the results from the computations and the experiments.

The Mie-Grüneisen equation of state (EOS) is used to describe the volumetric behavior,

$$p=-\sigma_H=\frac{\rho_0 c_0^2\eta}{\left(1-s\eta\right)^2}\left(1-\frac{\Gamma_0\eta}{2}\right)+\Gamma_0\rho_0 E_m, \tag{25}$$

where, ρ_0 is density in the reference configuration, $\eta=1-\rho_0/\rho$ is the nominal volumetric compressive strain in which ρ is the instantaneous density, Γ_0 is Grüneisen's gamma at the reference state and for polymers $\Gamma_0\simeq 1$, E_m is the internal energy per unit mass, and c_0 and *s* are the constants in the linear relationship between the shock velocity U_s and the particle velocity U_p, $U_s=c_0+sU_p$. For the material analyzed, $U_s=2315.4+1.905U_p$, and the orientation-dependency of U_s-U_p relationship is negligible [118].

To account for arbitrary patterns of fracture, a phenomenological damage criterion proposed by Hooputra et al. [123] is used. The damage model assumes that the equivalent plastic strain at the onset of damage is $\bar{\varepsilon}_D^{pl}$. The evolution of damage is based on fracture energy per unit area dissipated during the damage process, and the equivalent plastic strain at failure is $\bar{\varepsilon}_f^{pl}$. $\bar{\varepsilon}_D^{pl}$ and $\bar{\varepsilon}_f^{pl}$ are the input parameters and selected based on experimental results. To reduce mesh dependence associated with material failure, a characteristic element length L_E is incorporated in ABAQUS. An equivalent displacement at failure is introduced such that $\delta_f = L_E \cdot \bar{\varepsilon}_f^{pl}$. For three-dimensional elements, L_E is the cube-root of element volume. An alternative solution to mitigate the effects of mesh sensitivity is a non-local approach (not used here) which defines a characteristic length L_M as a material property [124, 125]. The material property sets are listed in Table 7 and color-coded through this dissertation.

A penalty force algorithm is used to achieve proper contact at fracture sites. The Coulomb friction law is used to determine the stick-slip states of the sliding surfaces in contact and to estimate frictional heating. The frictional heating rate over volume ΔV with surface ΔS is

$$\dot{W}^F = \frac{1}{\Delta V} \int_{\Delta S} \mu \sigma_n v_{rel} \, dS, \tag{26}$$

where μ is coefficient of friction and selected to be 0.5 for all surfaces in contact, σ_n is the normal stress between the surface pair in contact, and v_{rel} is the relative sliding velocity of contact pairs.

Table 7 – Material property sets used in the simulations.

Material set	Density (gr/cm^3)	E (GPa)	σ_c (MPa)	$\varepsilon_y\,(\%)$	$\bar{\varepsilon}_D^{pl}\,(\%)$	$\delta_f = L_E \cdot \bar{\varepsilon}_f^{pl}$ (mm)
Filaments-set 1 (blue filaments)	1.6	0.5	15.0	3.0	12	0.0188
Filaments-set 2 (green filaments)	1.6	2.5	22.5	0.9	12	0.0188
Filaments-set 3 (red filaments)	1.6	4.5	30.0	0.7	12	0.0188
Inter-filament surfaces	1.1	2.5	22.5	0.9	8	0.0125
Inter-filament voids	0.5	0.5	15.0	3.0	4	0.0063

4.3 Results and Discussion

4.3.1 Mesh-size Convergence Analysis

To evaluate mesh sensitivity, the size of elements is varied over a range of 31-79 μm. Figure 41 shows the energy dissipated through plastic deformation, friction, and damage as a function of the element size. The solution reaches convergence for an element size of 31 μm. At this size, samples are meshed with ~4×10^6 cubic elements. To prevent shear locking and reduce volumetric locking, reduced-integration eight-node brick elements (specified with C3D8RT in ABAQUS) are used [126]. The selection of a certain mesh size in conjunction with the implementation of a characteristic length equal to the cube root of the element volume provides an approximately non-local basis for damage initiation and evolution.

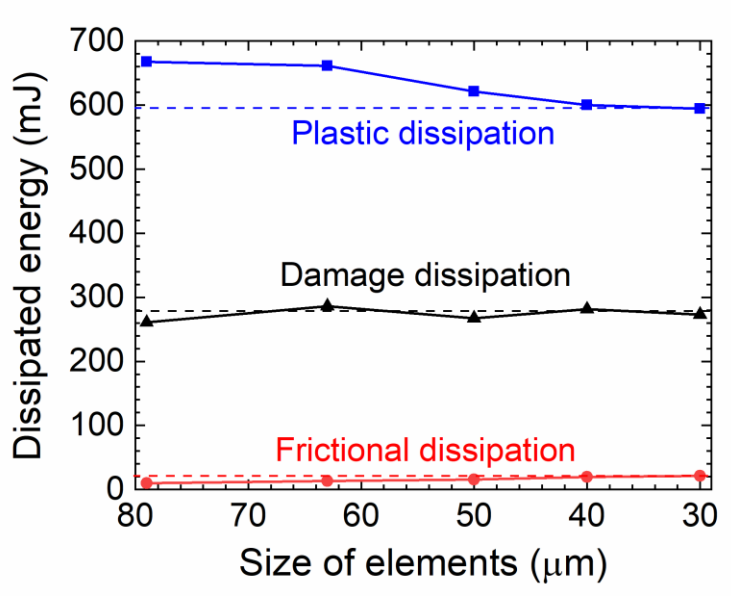

Figure 41 – Dissipated energy levels as a function of element sizes.

4.3.2 Experiments and Model Validation

To ensure the computational model captures the essential physics of the material, the results obtained from computations are compared with experimental measurements. Figure 42 compares stress-strain curves obtained from the computations and experiments under quasi-static loading conditions. Under both longitudinal and transverse loading, the calculated overall stress levels are in very good agreement with the experimentally measured stress levels. Specifically, the computations closely predict the onset of plastic deformation and failure.

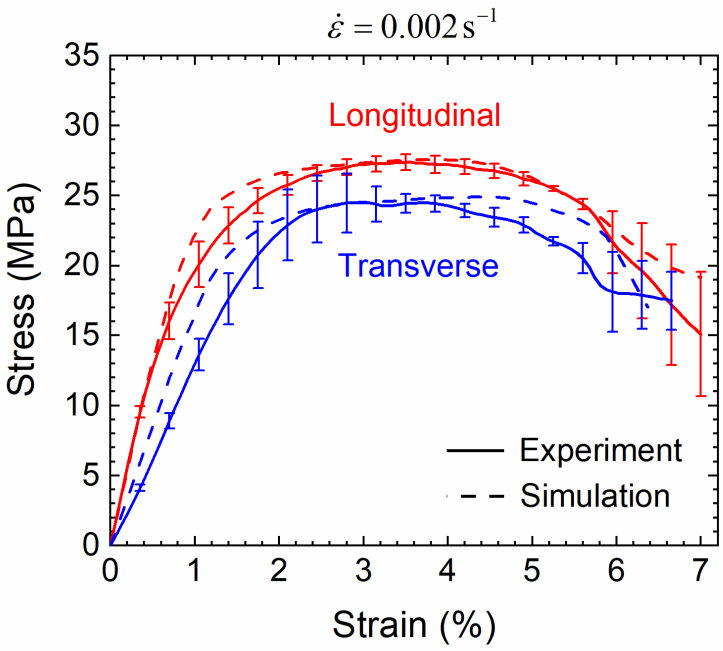

Figure 42 – Comparison of measured and calculated strain-stress curves for longitudinal and transverse orientations. The error bars show the variation of the overall stress levels measured for multiple samples.

The results obtained through computations are quantitatively and qualitatively compared with those obtained from dynamic experiments. The experiments and computations are performed at a loading rate of ~313.4 s^{-1}. The deformation modes, the time and strain at damage initiation, and temperature signatures are compared. The samples are deformed to overall levels of strain up to ~20%. Figure 43(a) shows the time histories of the overall engineering strain $\bar{\varepsilon} = (L - L_0)/L_0$ from the experiments and computations. L is the instantaneous length of a sample and $L_0 = 5$ mm is the initial length. This strain is measured by tracking the positions of the indenters through the VL images. Both computations and experiments show fracture at or after ~ 200 μs of loading, with the onset of failure at overall strains in the range of 3.4-5.9%. The onset of fracture is indicted by "•", with solid lines before this symbol denoting unfractured states and dash lines after this

symbol denoting post-fracture deformation. The infrared images are captured at $t = 300$ and 600 μs.

Figure 43(b) compares the lowest, average, and highest temperature levels obtained from the simulations and the experiments. The superscripts "Exp." and "Sim." denote experimental measurements and simulations, respectively. The calculated temperatures are in very good agreement with the experimentally measured temperatures, with the error being only ~3.9 K in the highest temperatures at $\bar{\varepsilon} = 0.19$ and $t = 600$ μs. At this time, the maximum error in the temperature increase between the computations and the experiments is ~14.0%. The agreement provides one validation of the computational model.

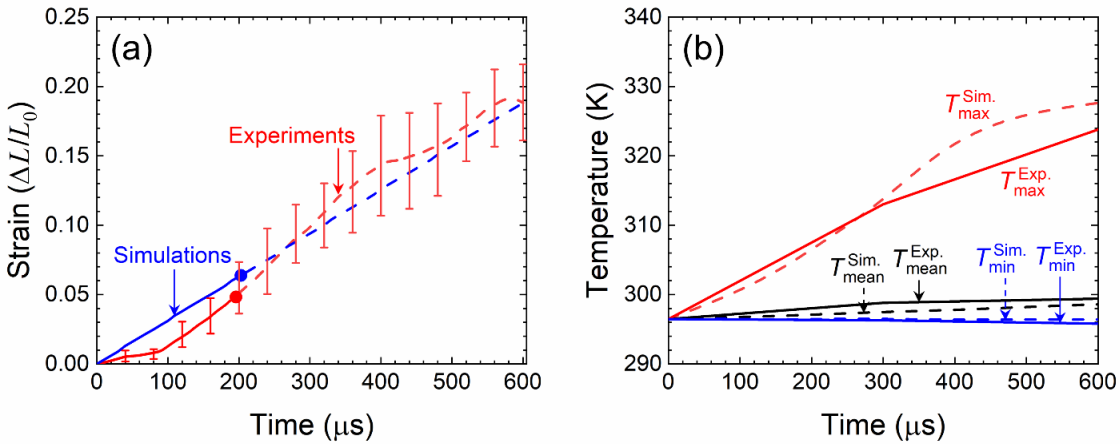

Figure 43 – Comparison of measured and calculated overall strain levels as a function of time. The onset of rupture is indicted by "•", with solid lines before this symbol denoting un-ruptured states and dash lines after this symbol denoting post-rupture deformation. The error bars show the variation of the overall strain levels among the multiple samples. (b) Comparison of measured and calculated lowest, mean, and highest temperature levels.

4.3.3 Damage Initiation and Crack Nucleation Sites

Figure 44 shows a sequence of optical images for the sample loaded in the x (⊥ print) direction (see Figure 37). Under loading, the sample shows shear deformation and shear rupture. To quantify the deformation fields in the samples, digital image correlation (DIC) analyses are performed. A total of 4 samples are studied at similar conditions. The DIC analyses concern the deformation fields up to the onset of shear rupture which occurs around $t = 170 - 220\ \mu s$ or overall strains of 3.4-5.9% for the sample set. Figure 45 shows the distributions of the maximum in-plane tensorial shear strain $\left(\gamma_{\max}/2\right)$ in the samples at the onset of rupture as calculated via

$$\frac{\gamma_{\max}}{2} = \sqrt{\left(\frac{E_{xx} + E_{yy}}{2}\right)^2 + E_{xy}^2}, \tag{27}$$

where E_{xx}, E_{yy}, and E_{yy} are the Lagrangian strain components. The local maximum shear strain level at rupture is 4.8±0.8%. The DIC calculation is carried out using a subset size of 30 pixels $\left(408\mu m\right)$. Note that post rupture, this shear strain continues to increase and can reach values up to 20%. The shear band angle with respect to the loading direction is 33.6±5.3°. A similar value for the shear band angle was previously observed in a polymer bounded composite tested in an SHPB environment [68]. The material properties obtained and the physics captured in the experiments are used to inform the simulations. Table 8 quantifies the average and maximum strain rate, overall compression strain at onset of fracture, fracture initiation time, the overall strain at fracture initiation, and overall total compression for all samples analyzed.

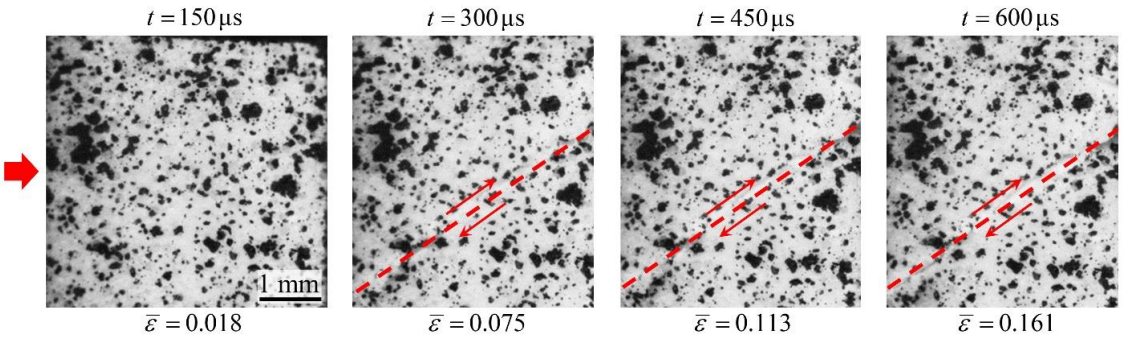

Figure 44 – Deformation for loading in the x-direction. The dashed lines and the arrows outline the rupture process and the relative motion.

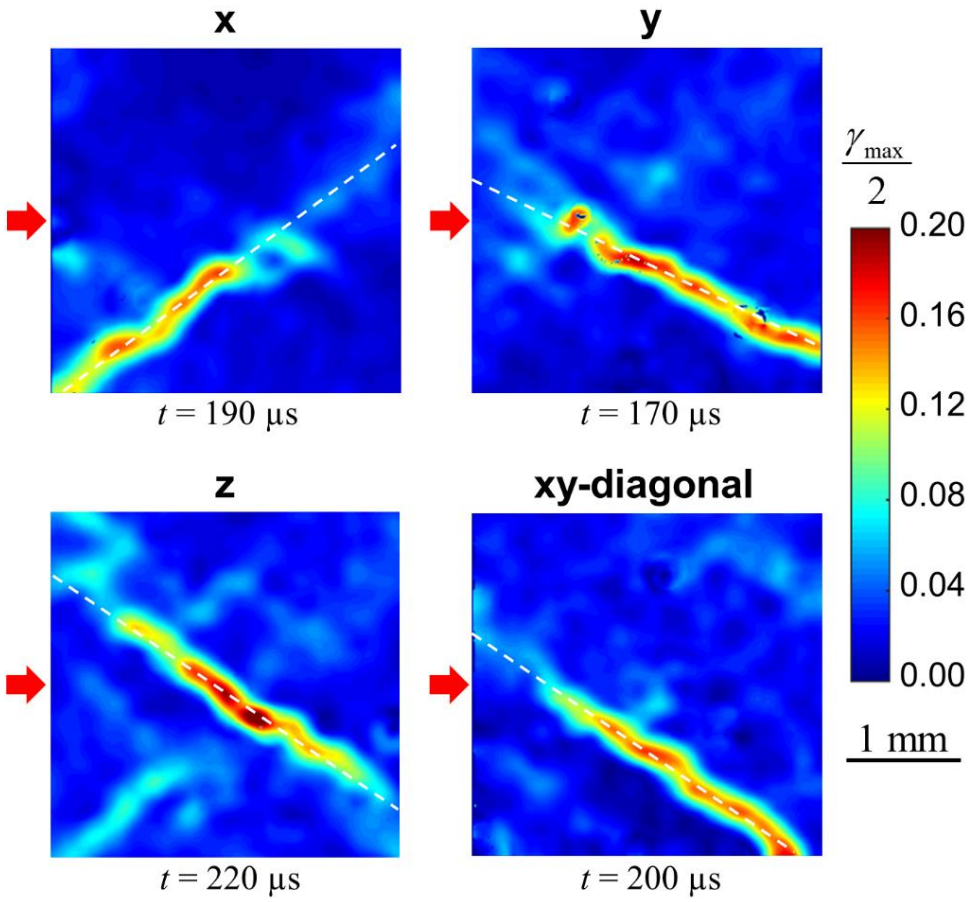

Figure 45 – Distributions of the maximum tensorial shear strain $(\gamma_{max}/2)$ at the rupture nucleation.

Table 8 – Summary of experiments.

No.	Loading direction	Maximum strain rate (s^{-1})	Average strain rate (s^{-1})	Fracture time (μs)	Overall strain at fracture	Overall compression
1	x	675	268	190	0.034	0.161
2	y	950	343	170	0.053	0.206
3	z	425	283	220	0.059	0.170
4	xy-diagonal	1100	360	200	0.044	0.216

In the experiments, shear bands nucleate from the edge of the samples for loading in the x, y, or xy-diagonal directions. For loading in the z-direction, the dominant shear band nucleates from an internal point rather than the edge, due to internal heterogeneities. It is difficult to experimentally relate the crack nucleation sites to the print structure due to the opaque nature of the sample. The computations, on the other hand, offer an opportunity to track the crack paths in the sample's interior. Here, it is assumed that samples are initially crack-free and cracks result from the loading events. The computations account for failure at all possible sites, inside the filaments and along the interfaces. Figure 46 shows the fracture initiation sites in samples loaded along the four direction at $\bar{\varepsilon} = 0.064$ or $t = 204\,\mu s$. Cracks nucleate at or before $\bar{\varepsilon} = 0.064$ or $t = 204\,\mu s$. The nucleation is at the filament junctions and propagates through the filaments. The sample loaded in the y-direction (along the filaments) does not experience significant fracture at this stage, and instead shows only minor crack development and interfacial debonding along the loading direction at the later stage of $\bar{\varepsilon} = 0.31$ when the other loading directions show extensive crack development throughout the sample. The effects of the orientation-dependent fracture strain levels on the overall stress-strain relations are discussed in the next section.

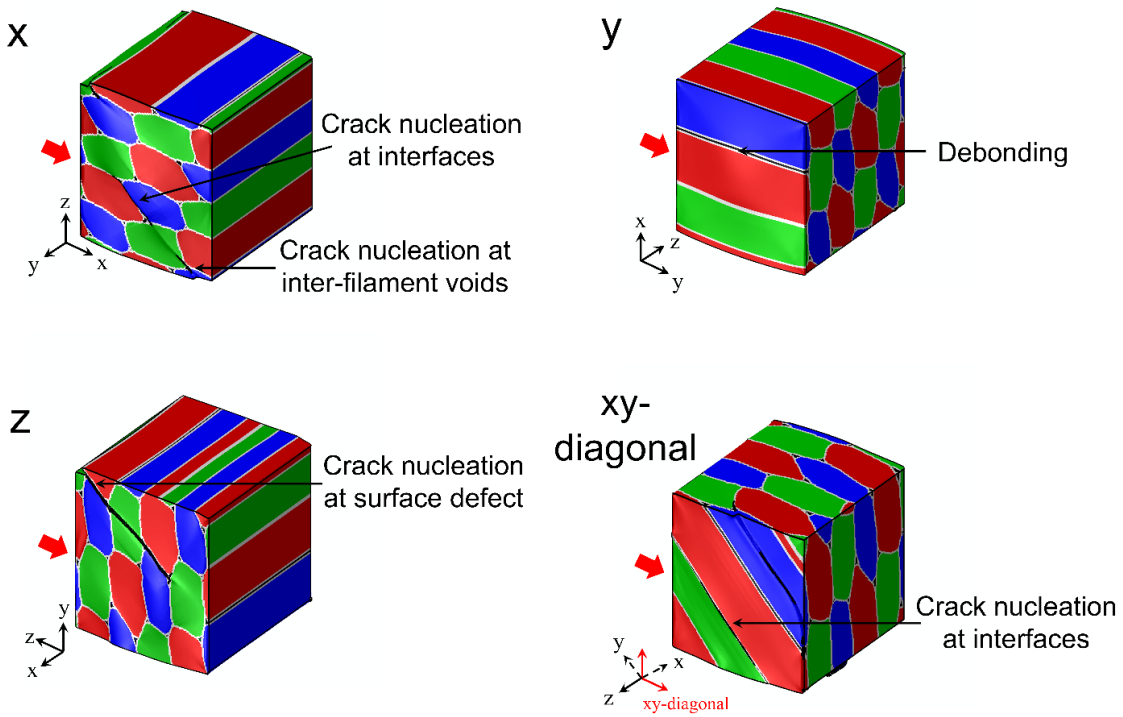

Figure 46 – Fracture initiation for different loading directions at $\bar{\varepsilon} = 0.064$ or $t = 204\,\mu s$.

4.3.4 Stress-Strain Curves

Figures 47(a-b) show the overall stress-strain relations for the four loading orientations. For comparison, a calculation is also carried out for the homogeneous sample (without microstructure or heterogeneities) having the properties of the base material as measured from the quasi-static uniaxial compression experiments (see Table 6). Specifically, Figure 47(a) shows the overall stress-strain relations for the early stages of loading up to $\bar{\varepsilon} = 0.03$. The sample loaded along the filaments (y-direction) shows a higher level of initial stiffness than the samples loaded perpendicular to the filaments (x or z direction). This is in agreement with the trend seen in experiments (see Table 6). The homogenized sample achieves the highest level of stress among all samples at the end of

elastic region $\left(\bar{\varepsilon} = 0.012, \bar{\sigma} = 25.7 \text{ MPa}\right)$. Beyond this point, the homogenized sample shows more pronounced damage initiation such that the overall stress level becomes the lowest among all samples at $\bar{\varepsilon} = 0.03$.

Figure 47(b) shows the stress-strain relations for overall strain levels up to 0.3. Overall in later stages, the sample loaded in the y-direction sustains a higher level of stress relative to the samples loaded in the other orientations. This sample even has a stress level that is higher than the stress level of the homogeneous sample up to $\bar{\varepsilon} = 0.2$. This is due to the fact that the material undergoes minor damage and consequently experiences lower loss of stiffness. When the sample is loaded in the y-direction (along filaments), the initiation of damage is in the form of debonding sites parallel to the loading directions. The overall stress state in the sample does not result in major tension or shear at the tips of the cracks parallel to the loading direction. Therefore, the evolution of damage is relatively slow. In the homogenized sample, the cracks nucleate approximately at the 45-degree angles relative to the loading direction where maximum shear occurs. Consequently, damage propagates at a higher rate than the sample loaded in the y-direction. In contrast, the homogeneous sample sustains higher stress levels than the samples loaded in x, y and xy-diagonal directions. For these loading directions, portions of the microstructure interfaces are oriented at or close to the maximum shear planes. Since the damage initiation threshold levels at the interfaces are lower than the levels in the base material or the filaments, damage initiation is facilitated by the material microstructure. In summary, depending on the loading orientation, the microstructure morphology can significantly affect the material integrity and stress-carrying capability.

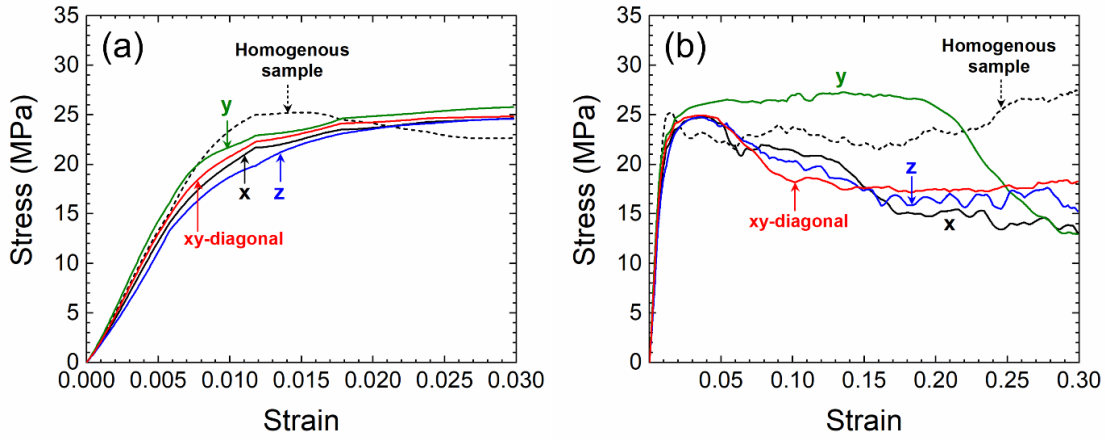

Figure 47 – Stress-strain curves for loading in the x, y, z, and xy-diagonal directions: (a) strain levels up to 0.03 and (b) strain levels up to 0.3.

4.3.5 Temperature Distributions

Plastic deformation and internal friction result in heating in the samples. Experimentally, it is challenging to separate the contributions of these mechanisms, but their combined effects are captured. Figure 48 shows the experimentally measured temperature fields in the four samples at $\bar{\varepsilon} = 0.19$ or $t = 600$ μs. The loading conditions are listed in Table 8. Significant temperature increases occur along the shear bands, with the highest temperatures occurring at the centers of the bands. There is no appreciable temperature increase far away from the shear bands. The maximum temperature increases in the samples is 27.4 ± 0.5 K, with a 0.5 K measurement error according to calibration data. Intense shear and the temperature increases occur primarily in shear bands in a localized fashion. The development of such hotspots is of primary interest for energetic materials, as they may lead to the initiation of chemical reaction. To quantify the spatial distribution and the extent of localization of heating, the temperature fields in Figure 48 are further analyzed by calculating the fractions of the sample area with each temperature.

This allows the degree of heating localization to be compared across different cases. Figure 49(a) shows the results of the analysis. The vertical axis can be interpreted as the probability of a random point on the sample surface to assume a certain temperature at $t = 300$ and 600 μs (corresponding strains are ~0.10 and ~0.19). This axis can also be interpreted to be the proportions of the sample surface having any given temperature in the range shown. The dominant temperatures in the samples (the temperature that is associated with the highest proportion of the material surface) are ~296-299 K. The highest temperatures in the samples are ~324 K and occurs mostly in the smaller regions where the samples undergo intense shear inside and around the shear bands.

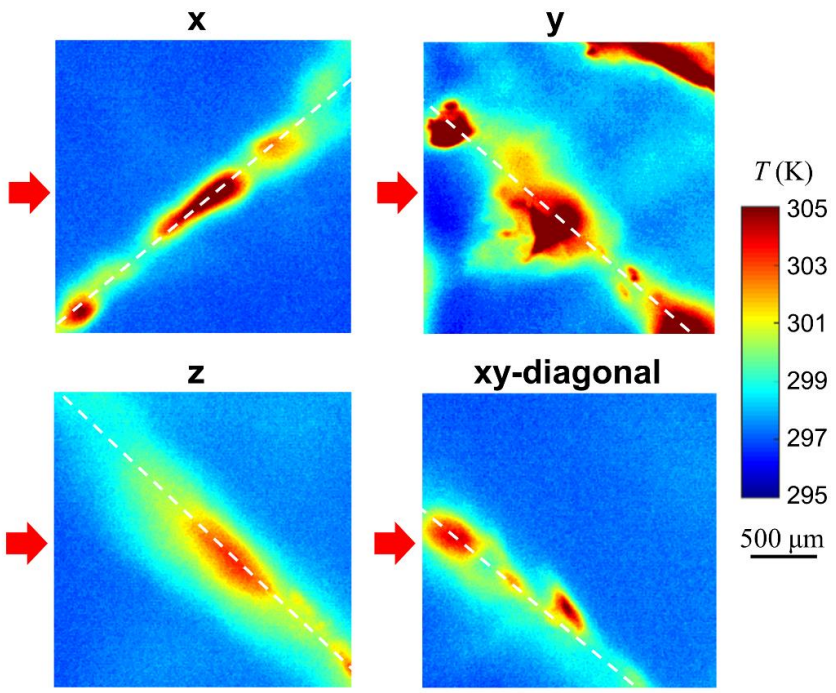

Figure 48 – Experimentally measured temperature fields in the samples loaded in the x, y, z, and xy-diagonal directions at $\bar{\varepsilon} = 0.19$ or $t = 600$ μs.

The orientation dependence of the temperature distributions can be observed through computations. Figure 49(b) shows how localized or spread out spatially the heating

is. Loading in the xy-diagonal direction yields the highest temperatures. In contrast, loading in the other directions lead to less concentrated heating and higher fractions of the material participate in the deformation and heating at the lower end of the temperature range. The homogeneous sample has the least concentration of heating, as expected.

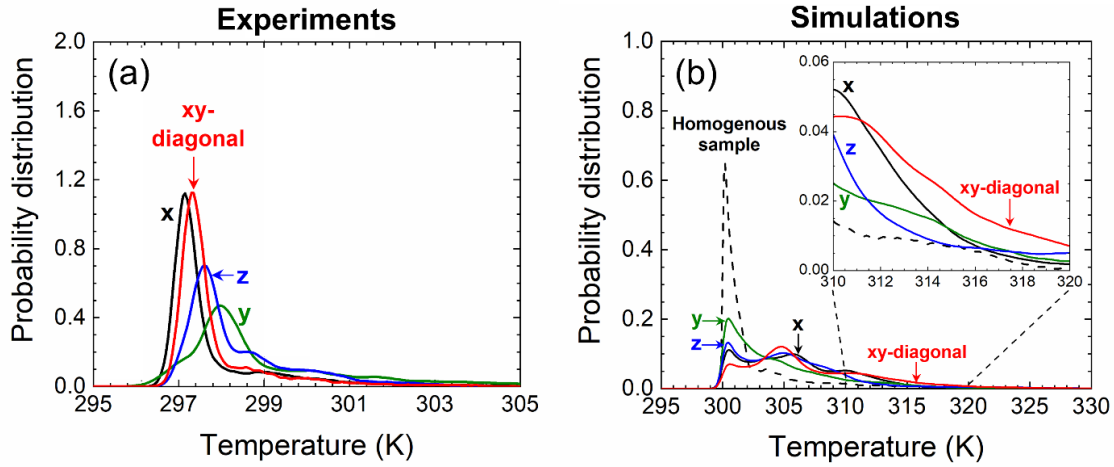

Figure 49 – Temperature distributions for different loading directions at $t = 600\,\mu s$; (a) experiments, and (b) computations.

4.3.6 Displacement, Velocity and Temperature Profiles Along Shear Bands

Post rupture, the deformation fields on the two sides of the shear band are calculated separately using different regions of interest (ROIs). The edges of the ROIs next to the shear bands are 0.2 mm (15 pixels, the subset radius) from the shear band centerline. For loading in the x-direction, Figure 50 shows the horizontal and vertical displacement fields and the corresponding temperature fields at $t = 300$ and $600\ \mu s$. Rupture occurs at $t = 200\ \mu s$. The displacement field on each side of the shear band is approximately uniform. There is no appreciable temperature increase away from the shear band. Significant temperature increases occur along the shear bands, with the highest

temperatures occurring at the centers of the bands. The s-axis in the figure indicates the distance along the shear bands referred to in the rest of this chapter.

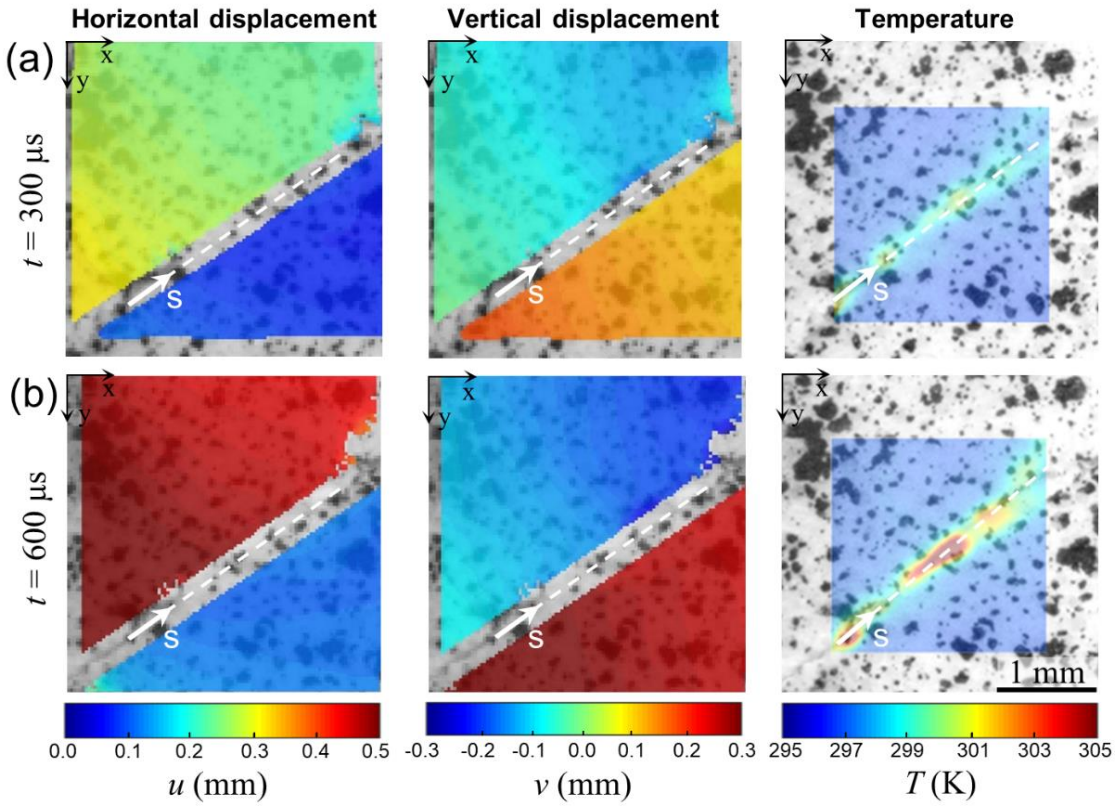

Figure 50 – Displacement and temperature fields in the sample loaded in the x-direction at (a) t = 300 µs and (b) t = 600 µs.

Figure 51 compares the profiles of the relative displacement and velocity across the shear bands (displacement and velocity jumps) with the temperature profiles at $\bar{\varepsilon} = 0.19$ or $t = 600$ µs. The horizontal axis presents the distance along the bands. For loading in the x-direction, the shear band-parallel displacement and transverse velocity jump are relatively uniform along the bands, indicating relatively homogeneous slip along the shear band path (s-axis). However, the corresponding temperature profiles along the shear band are quite non-uniform. The displacement and velocity jump for the y, z, and xy-diagonal directions show significant variations along the bands. In general, there is a correlation

between the magnitudes of the relative displacement and velocity jump, their non-uniformity along the bands, and the temperature increases. The non-uniformity appears to be associated with the heterogeneous nucleation of cracks along the shear band paths. Higher and faster relative slip tend to give rise to higher local temperature increases. For example, for loading in the y-direction, the location of the peak temperature at $t = 600$ μs (~324 K) coincides with the location of displacement and velocity jump change along the shear band path.

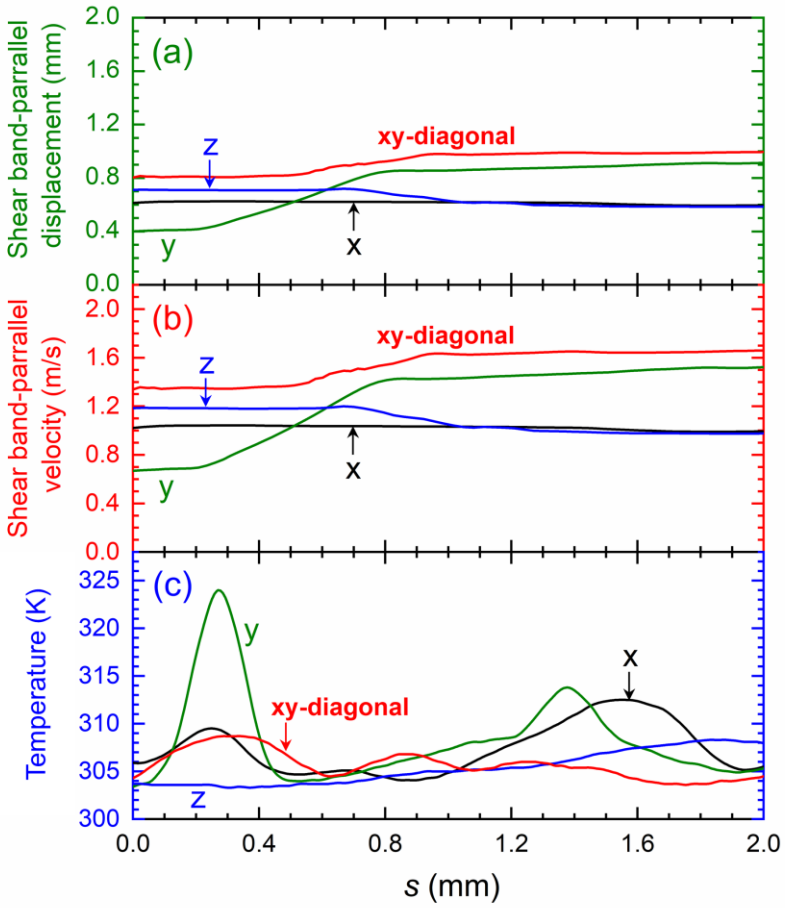

Figure 51 – (a) Profiles of relative displacement, (b) velocity jump across shear bands, and (c) temperature along the shear bands at t = 600 μs.

4.3.7 Energy Dissipation Levels

Dissipations from friction and plastic deformation turn into heat and contribute to the temperature increase in the samples. The dissipation mechanisms (friction and plasticity) and their relative contributions to heating are analyzed as functions of the loading orientations. Figures 52(a-b) show the contributions to dissipation by plastic deformation (W_P) and fiction (W_F), respectively. Overall, the contribution of internal friction is orders of magnitude lower than that of plasticity. Loading in the y-direction results in the highest plastic dissipation but lowest frictional dissipation. In contrast, loading in the xy-diagonal direction leads to lowest plastic dissipation but highest frictional dissipation. This interplay is directly related to the formation of shear bands and the extent of localization of the shear deformation. In general, less damage corresponds to higher levels of stress carried by the materials which in turn lead to higher levels of inelastic/plastic dissipation. Figure 52(c) show the frictional dissipation as a fraction of the overall dissipation in the samples (W_F/W). Depending on the orientation, frictional dissipation is only responsible for 0.9 - 4.5% of the total heating and bulk plasticity accounts for the rest. Although in absolute terms, frictional dissipation is low, it plays an important role in hotspot development, owing to the fact that frictional heating is highly localized in the shear bands. The importance of frictional dissipation can be revealed by comparing the trends in frictional dissipation and the highest temperatures in the samples. The sample loaded in the xy-diagonal direction experiences the lowest overall heating, but has the highest level of frictional dissipation and the highest fraction of material volume in the peak temperature range of 310-320 K [see Figure 49(b)] among all orientations. Loading in the y-direction leads to the highest level of inelastic dissipation and overall

dissipation. Note that while loading in the y-direction leads to overall heating that is approximately 37.2% higher than that for loading in the xy-diagonal direction, it leads to a lower fraction of material volume having the higher temperatures in the range of 310-320 K. This is because the deformation is less localized under y-direction loading and more spread out in the material.

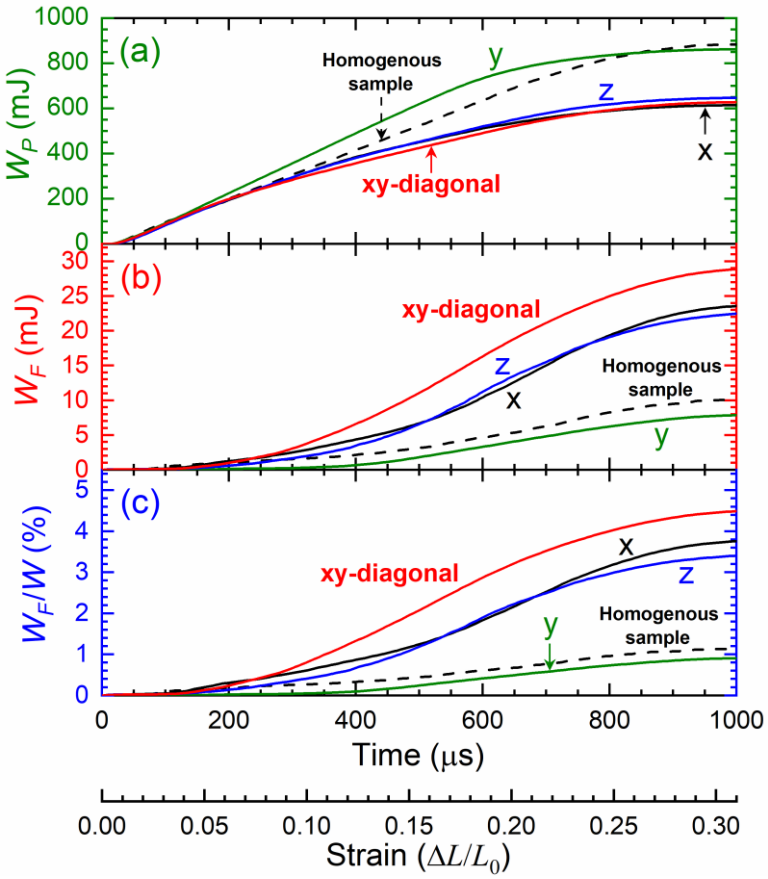

Figure 52 – (a) Plastic dissipation levels, (b) frictional dissipation levels, and (c) friction dissipation as a fraction of overall dissipation as functions of time for loading in different directions.

4.4 Summary

Experiments and simulations are performed to analyze the dynamic thermo-mechanical behavior of an AMEM simulant whose base material consists of a photopolymer and solid particles. The mesoscale deformation, failure, and heating of the material under loading along four different directions with respect to the print structure are studied. This chapter focuses on response anisotropy arising from the AM structures of the material. A split-Hopkinson pressure bar (SHPB) is used to apply compressive loading at an overall strain rate of 313.4 s^{-1}. Integrated high-speed visible light (VL) and infrared (IR) imaging is used to simultaneously measure the deformation and temperature fields over the same area of a sample with microsecond-level time resolutions and micron-level spatial resolutions. The overall field of views (FOVs) for the VL and IR images are 7.0×4.4 mm and 2.2×2.2 mm, respectively. Shear band development is the primary mechanism for deformation, heating, and ultimate failure. The influence of loading direction relative to the AM structure of the material primarily manifests through how shear bands form. Post-rupture sliding along the shear bands is the primary heating mechanism and leads to significant temperature increases, with the highest temperature increase observed being 27.4 K. The maximum shear strains at rupture is observed to be 4.8 ± 0.8%. The shear bands are observed to be 33.6 ± 5.3° relative to the loading direction. The deformation and temperature profiles along the shear bands are obtained. The correlations in the variations in the profiles appear to coincide with the nucleation of rupture out of material heterogeneities and defects.

An experimentally-informed Lagrangian finite element framework is developed that accounts for finite-strain elastic-plastic deformation, strain-rate effect, arbitrary failure

initiation and propagation, post-contact and friction, heat generation resulting from friction and inelastic bulk deformation, and heat conduction. The microstructures used in the simulations are generated based scanned morphologies of the real material. Simulations performed focus on failure initiation and the contributions to heating, and interplays between plasticity and internal friction. The results show that cracks nucleate at the filament junctions and propagate through filaments. Loading in the print direction leads to minor damage and higher stresses compared with other loading directions. Loading at 45-degree with respect to the print orientation (xy-diagonal direction) leads to lower stresses, more intense shear banding and higher temperatures. The simulations further reveal that intense shear leads to more significant contributions of internal friction to heating and higher fractions of the material volume that attain higher temperatures. Overall, frictional dissipation accounts for only 0.9-4.5% of heating with plasticity responsible for the rest. Despite of this disparity, friction plays an important role in hotspot development, owing to the fact that it is much more localized and occurs primarily in the interior of intensely formed shear bands.

CHAPTER 5. EFFECT OF STRUCTURE ON RESPONSE OF AMEM SIMULANT TO INTERMEDIATE STRAIN RATE LOADING

5.1 Introduction

Built upon Chapter 4, this chapter further analyzes the mesoscale thermo-mechanical response of the material under dynamic loading. The analysis here focuses on the effects of microstructure, porosity, inter-filament strength, and filament size on overall behavior at strain rates of 400-2000 s^{-1}.

5.2 Material and Microstructure

Three sets of simulations are performed to quantify the effects of print structure, defects (voids and interfaces), and filament size on the thermo-mechanical response of the material to dynamic loading. In the first set, the behavior of the reference microstructure (1.2 mm size filaments and 3 vol% inter-filament voids) is analyzed in 4 [x, y (filament), z (build), and xy-diagonal] orientations. In the second set, variants of the reference microstructure are analyzed with 0, 3 and 6 vol% voids while the 1.2 mm size for the filaments is maintained. In addition, two other cases with stronger and weaker inter-filament surfaces with respect to that in the reference microstructure are analyzed. In the third set, three samples are analyzed with filament sizes of 0.8, 1.2, and 1.6 mm. The three cases have the same level of porosity of 3% voids by volume. In the latter two simulation sets, the samples are subjected to dynamic loading in the x-direction in which the effects

of AM microstructure are most pronounced. Figures 53(a-c) summarize the microstructures of the samples used in all simulation sets. Samples are compressed between two rigid surfaces (front and back), and no lateral (upper and lower) confinement is used. Loading is in the horizontal direction, with the left surface the moving with velocities of 2-10 m/s and the right surface remaining stationary, resulting in overall strain rates of 400-2000 s^{-1}. This loading configuration mimics the loading conditions in the split-Hopkinson pressure bar (SHPB) or Kolsky bar experiments reported in Chapter 4.

5.3 Results and Discussion

5.3.1 Orientation Dependence of Behavior

A sample is subjected to loading along 4 orientations (x, y, z, and xy-diagonal, with filaments oriented in the y-direction). Figure 54(a) shows how damage evolves in the samples at a strain rate of 1200 s^{-1}. Damage initiates at the filament junctions and propagates through the filaments. The sample experiences only minor damage at $\bar{\varepsilon} = 0.35$ when it is loaded in the y-direction, while the sample shows extensive damage when it is loaded at other orientations. Figure 54(b) shows the temperature fields in the samples at $\bar{\varepsilon} = 0.35$ ($t = 290\,\mu s$). Temperature spikes are located at or near fracture sites. Figure 55 quantifies the spatial distribution of temperature corresponding to Figure 54(b). Loading in the xy-diagonal direction results in the highest temperatures. In contrast, loading in other orientations yields less concentrated heating and higher fractions of the material participate at the lower end of the temperature range. The homogeneous sample obtains the lowest temperature levels.

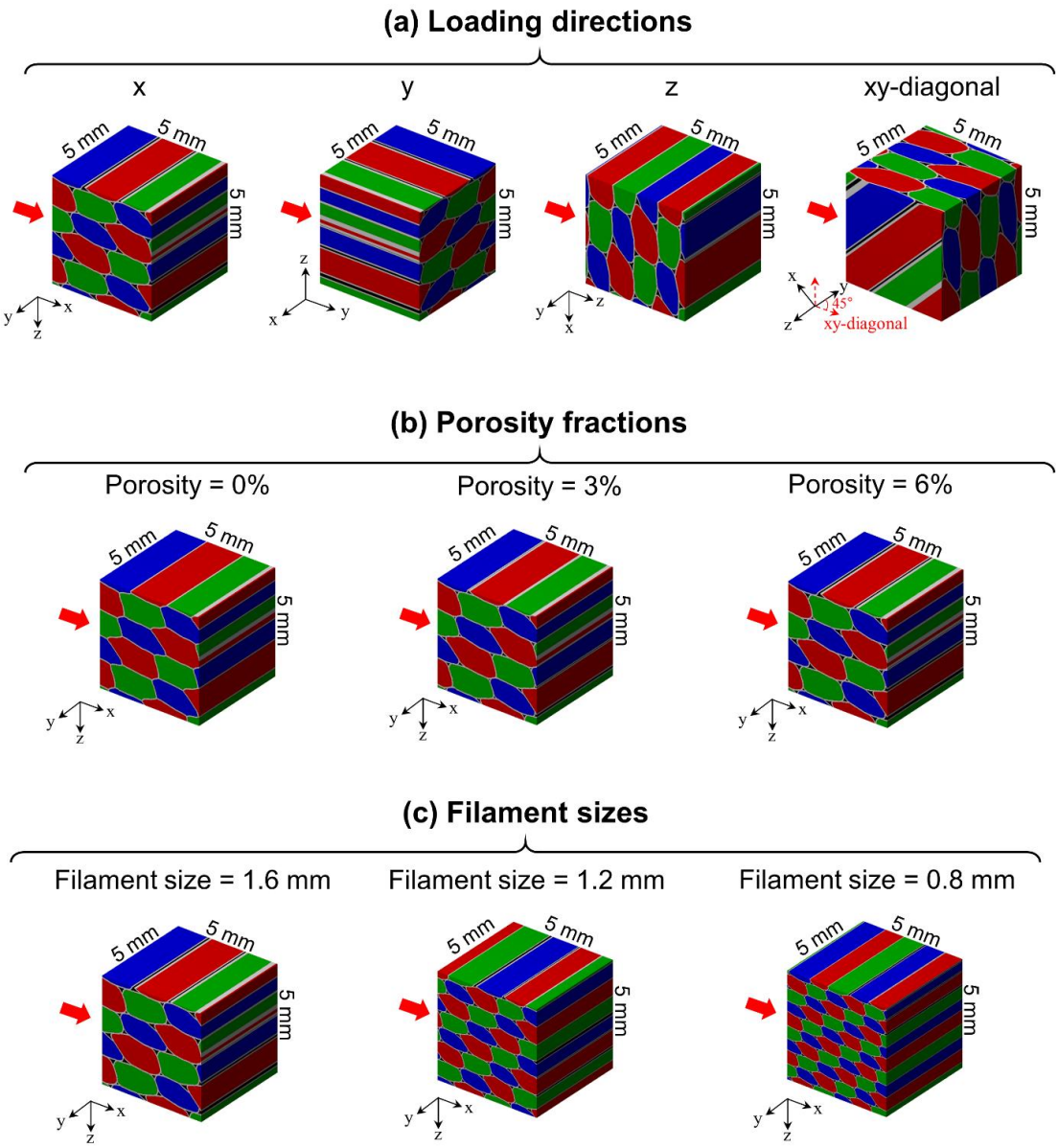

Figure 53 – Simulation sets and illustrations of impact directions with respect to AM printing pattern and microstructure morphologies; (a) loading along various orientations with respect to the material print structure, (b) porosities of 0-6 vol%, and (c) filament sizes of 0.8-1.6 mm.

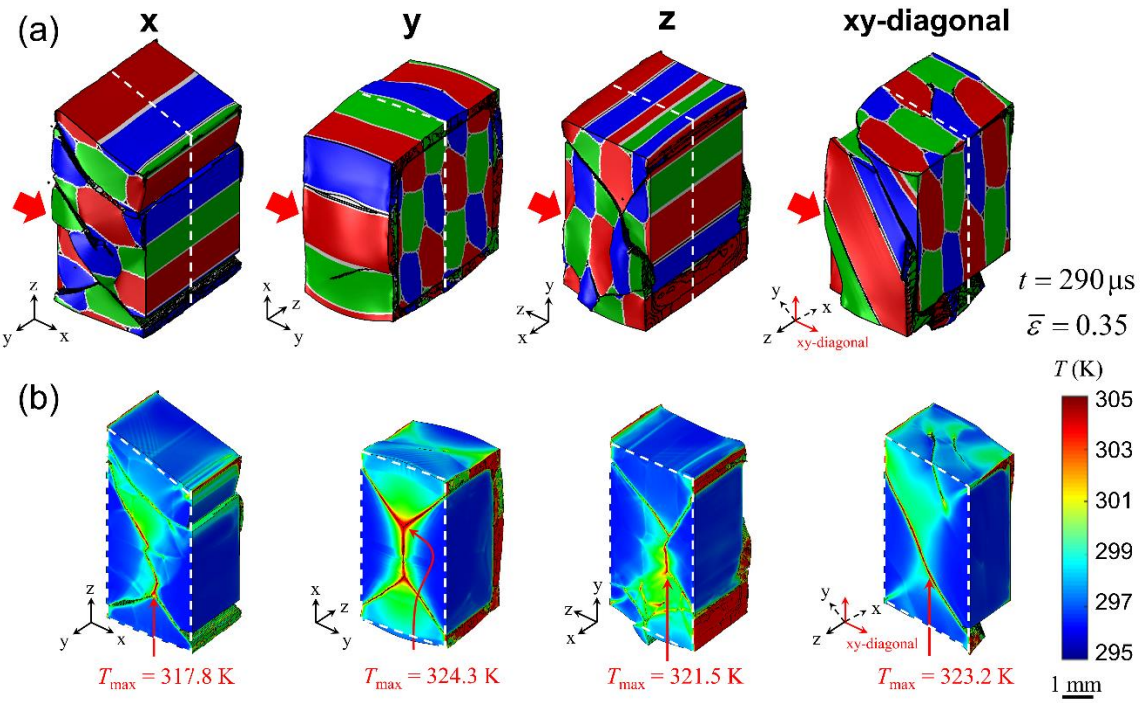

Figure 54 – (a) Fracture evolution in the samples loaded in various orientations, and (b) temperature distributions for loading along x-direction, y (filament) -direction, z (build) -direction, and xy-diagonal direction.

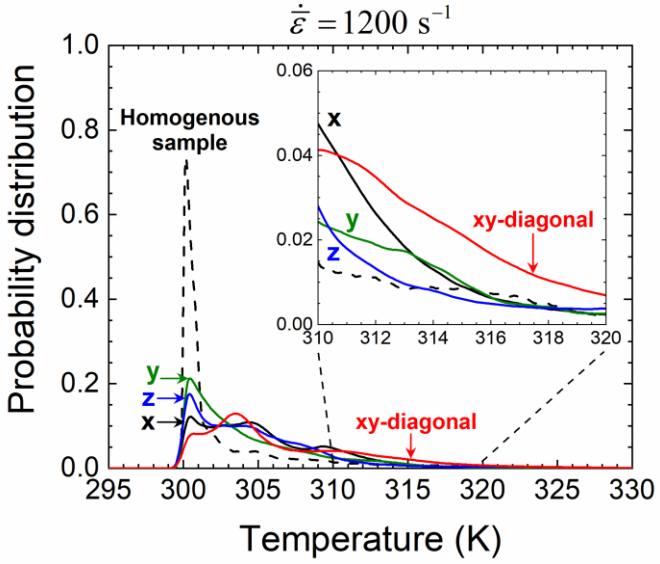

Figure 55 – Temperature distributions of the samples loaded in various directions and subjected to a strain rate of 1200 s^{-1}.

Figures 56(a-b) quantify contributions to dissipation by plastic deformation (W_P) and fiction (W_F) as functions of overall strain rate and loading orientation at $\bar{\varepsilon} = 0.35$. Both W_P and W_F increase with an increase in the loading rate, as expected. Frictional dissipation is more sensitive to the loading rate and increases $18.9 - 27.1\%$ as the loading rate increases from 400 to 2000 s^{-1}, but plastic dissipation is less sensitive and only increases $1.7 - 6.4\%$ over the same loading range. Loading in y-direction results in the least damage [see Figure 54(a)] and the highest level of stress carried by the material, leading to the highest plastic dissipation among all loading directions. In contrast, loading in the xy-diagonal direction leads to the highest damage and fracture, leading to the highest frictional dissipation. Despite only $1 - 4\%$ contribution to total heating, friction dissipation is localized at fracture sites and plays an important role in the development of hotspots. Figure 55 shows temperature distributions for all loading orientations. Although loading in the xy-diagonal direction yields the lowest overall plastic dissipation, but the highest level of frictional dissipation and the highest fraction of material volume in the peak temperature range of 310-320 K. Loading in y-direction leads to the lowest frictional dissipation and the lowest fraction of material volume in the peak temperature range despite the highest overall dissipation in the direction. The interplay between plasticity and friction is discussed in Chapter 4.

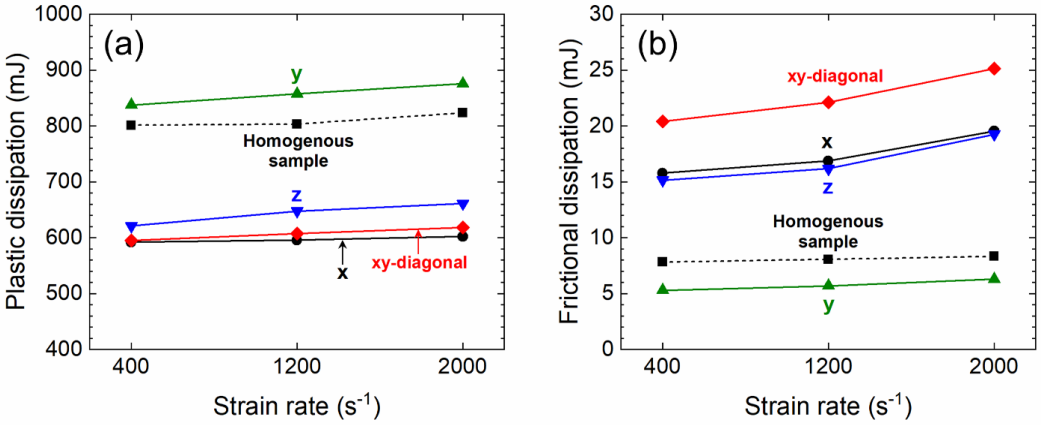

Figure 56 – Dissipations from (a) plastic deformation and (b) friction as a function of strain rate at $\bar{\varepsilon}$ = 0.35.

5.3.2 Effect of Void Volume Fraction and Inter-filament Strength

Voids and inter-filament surfaces are the two types of defects in the material. These defects control the overall response to dynamic loading. To quantify the effects of void fraction and interfacial strength, variants of the reference sample are analyzed. In one set of simulations, the porosity of the samples varied 0-6 vol%. The porosity of the reference sample is 3 vol%. Two other samples are generated based on the reference sample with amounts of voids of 0 vol% in one and 6 vol% in the other. The material constituent properties and the overall microstructure morphology are the same in all three samples.

Figure 57 shows the overall stress-strain curves of the three samples at a strain rate of 1200 s^{-1}. The samples with lower porosities show higher levels of stress carried up to the strain of 26% and all cases show approximately equal levels of stress after that. The variations in overall stress levels result from damage initiation and evolution. In general, damage initiates from inter-filament junctions and propagates along shear bands. Higher porosity levels lead to earlier damage initiation. Figure 58(a) shows damage initiates at

$\bar{\varepsilon} \simeq 0.05$ for 6% porosity but at $\bar{\varepsilon} \simeq 0.08$ for 0% porosity. The overall damage dissipation levels begin to converge at $\bar{\varepsilon} \simeq 0.22$ and become approximately equal at $\bar{\varepsilon} \simeq 0.36$. In the homogeneous sample, damage initiates at $\bar{\varepsilon} \simeq 0.14$, which is later than in the heterogeneous samples. Higher porosities lead to higher levels of damage at earlier stages of loading and higher overall frictional dissipation, as shown in Figure 58(b). Figure 59 shows the temperature distributions. The samples with higher porosities exhibit higher proportions of volume with temperatures higher than 305 K. The samples with higher levels of frictional dissipation show higher material proportions with high temperatures. The difference in temperature distributions between the sample with no porosity and the samples with porosities is pronounced. In contrast, the difference in the temperature distributions among the samples with porosities is relatively minor. This fact shows that the rate of hotspot development with respect to the porosity is higher at lower porosity levels.

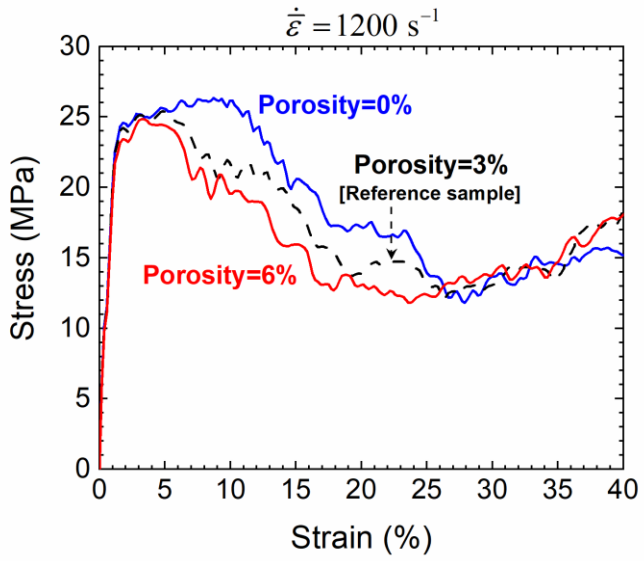

Figure 57 – Strain-stress curves of the samples with porosities of 0-6 vol%.

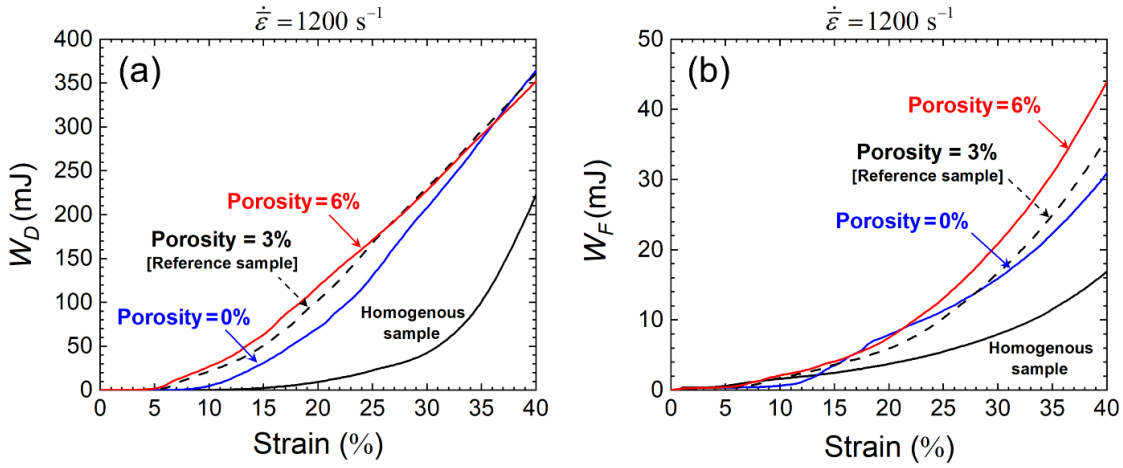

Figure 58 – Dissipations from (a) damage dissipation (W_D) and (b) friction (W_F) as a function of overall strain for the samples with porosities of 0-6 vol%.

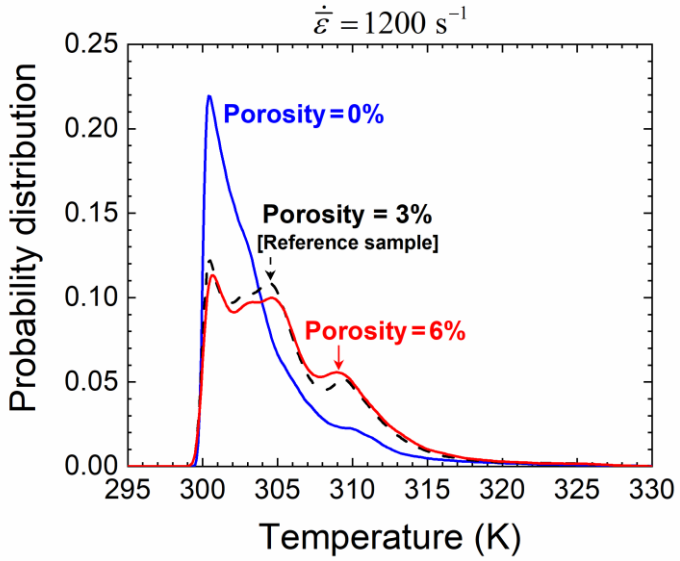

Figure 59 – Temperature distributions in the samples with porosities of 0-6% at $\bar{\varepsilon} = 0.35$.

In another set of simulations, three samples with various levels of interfacial strength are analyzed. Specifically, three levels of $\bar{\varepsilon}_f^{pl}$ (plastic strain at failure) for inter-filament surfaces are used. In the reference sample, the ratio between $\bar{\varepsilon}_f^{pl}$ at inter-filament

surfaces and at in the filaments is 0.67 $\left(R = 0.67\right)$. This level is referred to as "intermediate strength." The samples with *R*=0.37 and *R*=1 are referred to as having "low strength" and "high strength" inter-filament surfaces throughout this dissertation. When *R*=1, the plastic strain levels at the onset of damage $\left(\bar{\varepsilon}_D^{pl}\right)$ and failure $\left(\bar{\varepsilon}_f^{pl}\right)$ are equal to those in the filaments. Table 9 lists the values of parameters used for the three inter-filament strength levels.

Table 9 – Inter-filament property sets.

Property set	Density (gr/cm^3)	$E\left(\text{GPa}\right)$	$\sigma_y\left(\text{MPa}\right)$	$\varepsilon_y\left(\%\right)$	$\bar{\varepsilon}_D^{pl}\left(\%\right)$	δ_f (mm)	*R*
High-strength	1.1	2.5	22.5	0.9	12	0.0188	1.00
Medium-strength [reference sample]	1.1	2.5	22.5	0.9	8	0.0125	0.67
Low-strength	1.1	2.5	22.5	0.9	4	0.0063	0.34

Figure 60 shows the overall stress-strain curves of the samples with various inter-filament strength levels. The inter-filament strength level determines the overall integrity of the sample under loading. The samples with higher levels of inter-filament strength experience lower levels of damage and carry higher levels of stress. Figure 61 shows fracture patterns and temperature fields of cross-sections parallel to the loading direction. Higher levels of *R* result in lower levels of fracture. The hotspots are at or near crack surfaces. The sample with *R*=1 shows relatively larger hotspots at fracture sites. This fact can be quantitatively seen in Figure 62, where the temperature distributions in the samples

are shown. Compared with the samples with R=0.34 or 0.67, a higher proportion of the sample with $R=1$ is approximately at or close to the initial temperature (300-302 K). This is due to the fact that this sample undergoes a lower level of fracture; therefore, there are fewer sites for frictional sliding and consequent frictional heating. However, the R=1 case shows a higher proportion with temperatures higher than 312 K. The peak temperature values are primarily controlled by localized frictional heating. The frictional heating rate increases as normal stress increases [see Eq. (26)]. The samples with higher levels of inter-filament strength show lower levels of fracture and sustain a higher level of stress. Therefore, the fracture sites in these samples undergo more intense frictional heating as a result of the higher levels of stress.

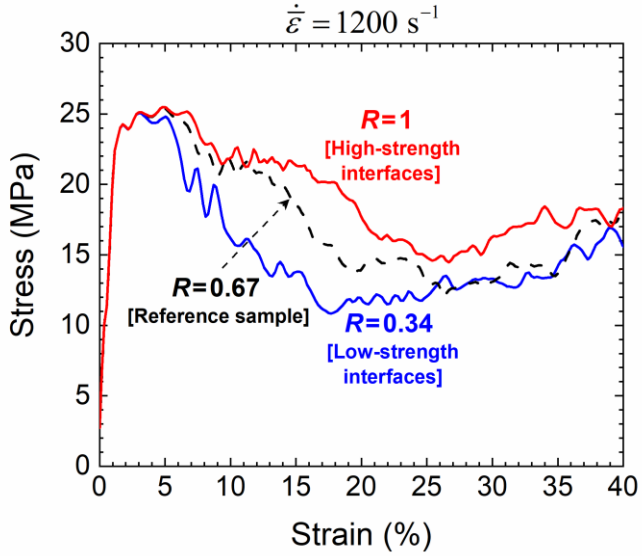

Figure 60 – Strain-stress curves of the samples with various inter-filament strength levels.

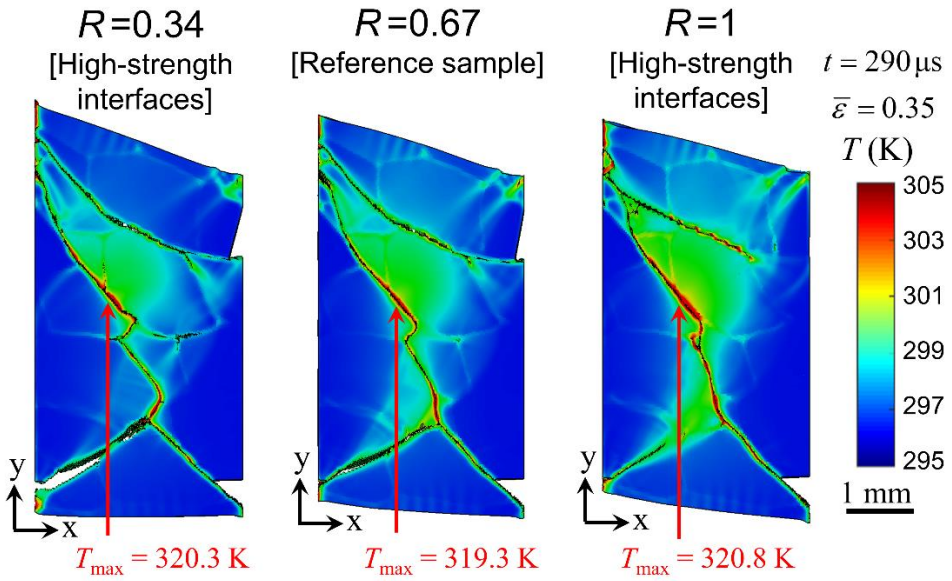

Figure 61 – Temperature fields in the samples with various inter-filament strength levels at $\bar{\varepsilon} = 0.35$ and $t = 290\,\mu s$.

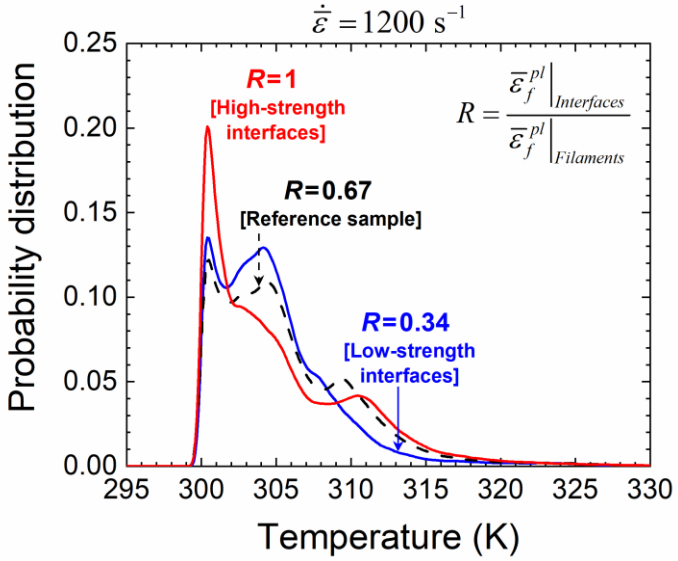

Figure 62 – Comparison of temperature distributions in the samples with various inter-filament strength levels at $\bar{\varepsilon} = 0.35$.

5.3.3 *Effect of Filament Size*

Filament size is an important printing parameter which can be used to tailor the thermo-mechanical response of printed materials. Here, three samples with filament sizes of 0.8 mm, 1.2 mm, and 1.6 mm are analyzed. These samples are loaded in the x-direction (perpendicular to the filaments) in which the role of the AM microstructure is more pronounced. The strain rates are in the range of 400-2000 s^{-1}. Figures 63(a) and 63(b) show fracture patterns and temperature fields at a strain of 1200 s^{-1}, respectively. The samples with smaller filament sizes show more damage and higher temperature spikes at the fracture sites. Figure 64 shows the temperature distributions in the samples corresponding to Figure 63(b). The samples with smaller filament sizes shows higher proportions at temperature levels higher than 314 K.

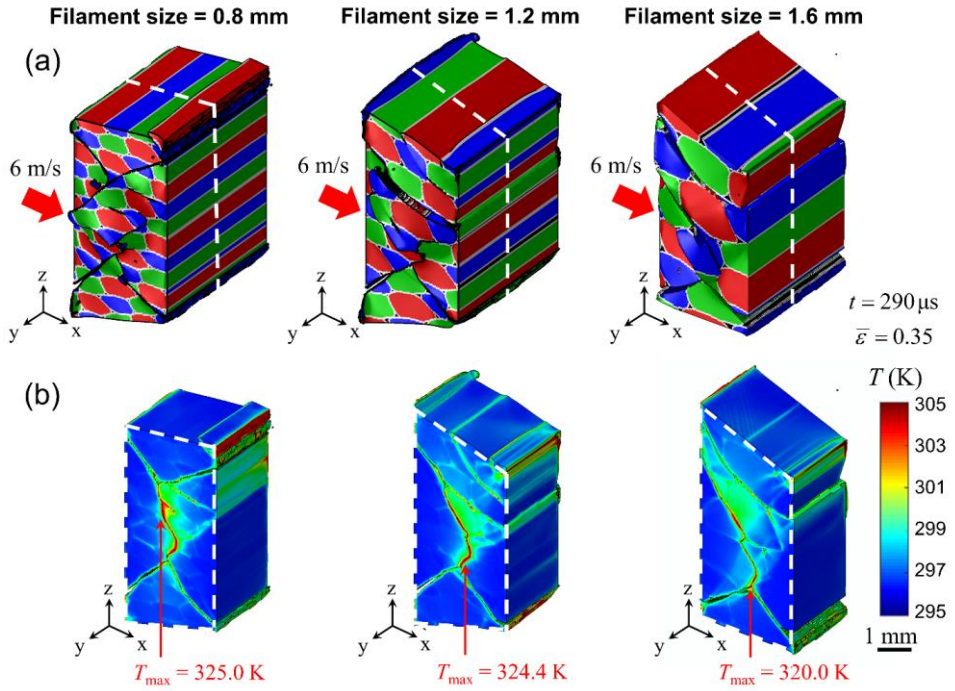

Figure 63 – (a) Fracture patterns and (b) temperature distributions in the samples with filament sizes of 0.8-1.6 mm at $\bar{\varepsilon} = 0.35$.

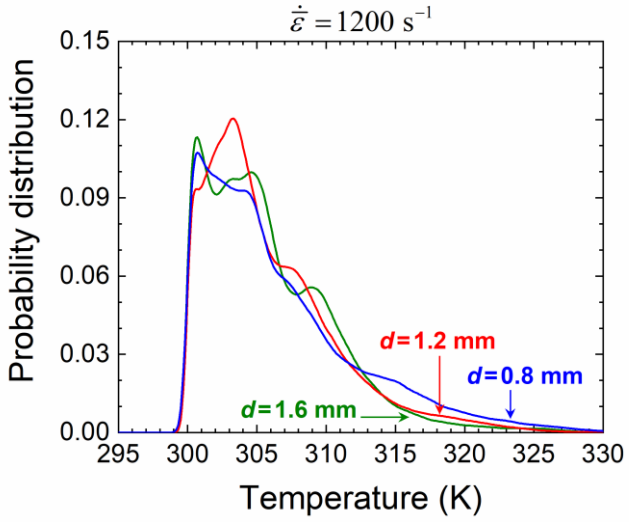

Figure 64 – Temperature distributions in the samples with filament sizes of 0.8-1.6 mm at $\bar{\varepsilon}$ = 0.35.

Figure 65 shows the ratios of damage dissipation in the heterogeneous AM samples to that in the homogenized sample $\left(W_D/W_D'\right)$ as a function of overall strain rate. The inherent heterogeneities as a result of the layer-by-layer build process lead to localized deformation and earlier damage initiation. Therefore, their dissipation levels are higher than that in the homogenous sample $\left(\text{i.e., } W_D/W_D' > 1\right)$. The results show that the effect of microstructure is more pronounced at higher loading rates. For the reference sample, W_D/W_D' increases from ~3.9 to ~6.5 as the loading rate increase from 400 s^{-1} to 2000 s^{-1}. The samples with smaller filament sizes show higher levels of damage. This due to the fact that the samples with smaller filament sizes contain higher densities of inter-filament surfaces, which are weaker than filaments and dominate the onset of damage. The results also show W_D/W_D' levels converge as the filament size decreases. At the strain rate of 2000 s^{-1}, W_D/W_D' is ~6.5 for the filament size of 1.2 mm and increases slightly by only ~1% as the filament size decreases to 0.8 mm. However, this ratio decreases by 9% as the filament

size increases to 1.6 mm. This observation shows that there is an upper bound in dissipation as filament decreases.

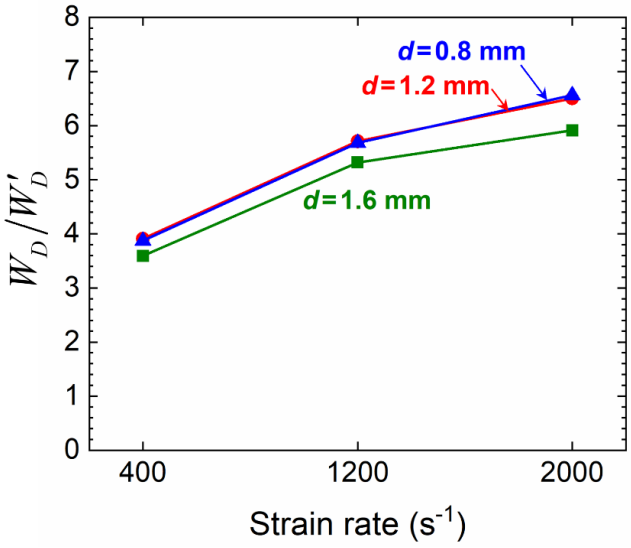

Figure 65 – Ratio of damage dissipation in the AM samples to that in the homogenous sample (W_D/W'_D) as a function of strain rate and filament size at $\bar{\varepsilon}$ = 0.35.

5.3.4 Effect of Microstructure Attributes on Dissipation

Figure 66 compares the ratios of overall plasticity, friction, and damage dissipations in the AM samples to that in the homogenous sample for all simulation sets. The values correspond to a 35% overall compression. The normalization with respect to the homogenous case provides an opportunity for comparing the effects of microstructure attributes. Figure 66(a) shows the normalized levels of dissipations for various loading orientations with respect to the filament direction. Except for 0° (loading along the filaments), the ratio for plastic dissipation (W_P/W'_P) is lower than unity. The ratios for damage and friction dissipations reach the highest values of 5.49 and 2.79, respectively, when loading is at 45°. Although damage dissipation for 0° is significantly higher than that

for the homogenous sample $\left(W_D/W_D' = 4.4\right)$, the corresponding frictional dissipation is lower $\left(W_F/W_F' = 0.72\right)$.

Figure 66(b) compares normalized dissipation levels for porosities in the range of 0-6%. Both W_F/W_F' and W_D/W_D' increase but W_P/W_P' decreases as porosity increases. This interplay between damage and plasticity results from the fact that higher porosities increase damage and result in lower levels of overall stress and plastic dissipation. At 0% porosity, W_F/W_F' and W_D/W_D' are the lowest at 2.01 and 4.54, respectively. At 6% porosity, W_F/W_F' and W_D/W_D' increase to 2.6 and 4.96, respectively. Figure 66(c) shows dissipations for the samples with filament sizes of 0.8-1.6 mm. While W_P/W_P' increases, both W_F/W_F' and W_D/W_D' decrease with as the filament size increases. The samples with smaller filament sizes have higher densities of inter-filament surfaces and undergo more damage and fracture. The results show that the dissipations plateau as the filament size decreases below ~1 mm. For the filament size of 1.6 mm, W_F/W_F' and W_D/W_D' are the lowest at 2.15 and 4.94, respectively. For the filament size of 0.8 mm, W_F/W_F' and W_D/W_D' are highest at 2.77 and 5.37, respectively.

Finally, Figure 66(d) shows the normalized dissipations as functions of inter-filament strength. Damage and plasticity exhibit opposite trends as the inter-filament strength increases, with W_P/W_P' increases, but W_F/W_F' and W_D/W_D' decrease. When the inter-filament surfaces are as strong as the filaments $\left(R = 1\right)$, W_F/W_F' and W_D/W_D' are

1.89 and 4.71, respectively. For the low-strength inter-filament surfaces $(R = 0.34)$, W_F/W_F' and W_D/W_D' are highest at 2.59 and 4.93, respectively.

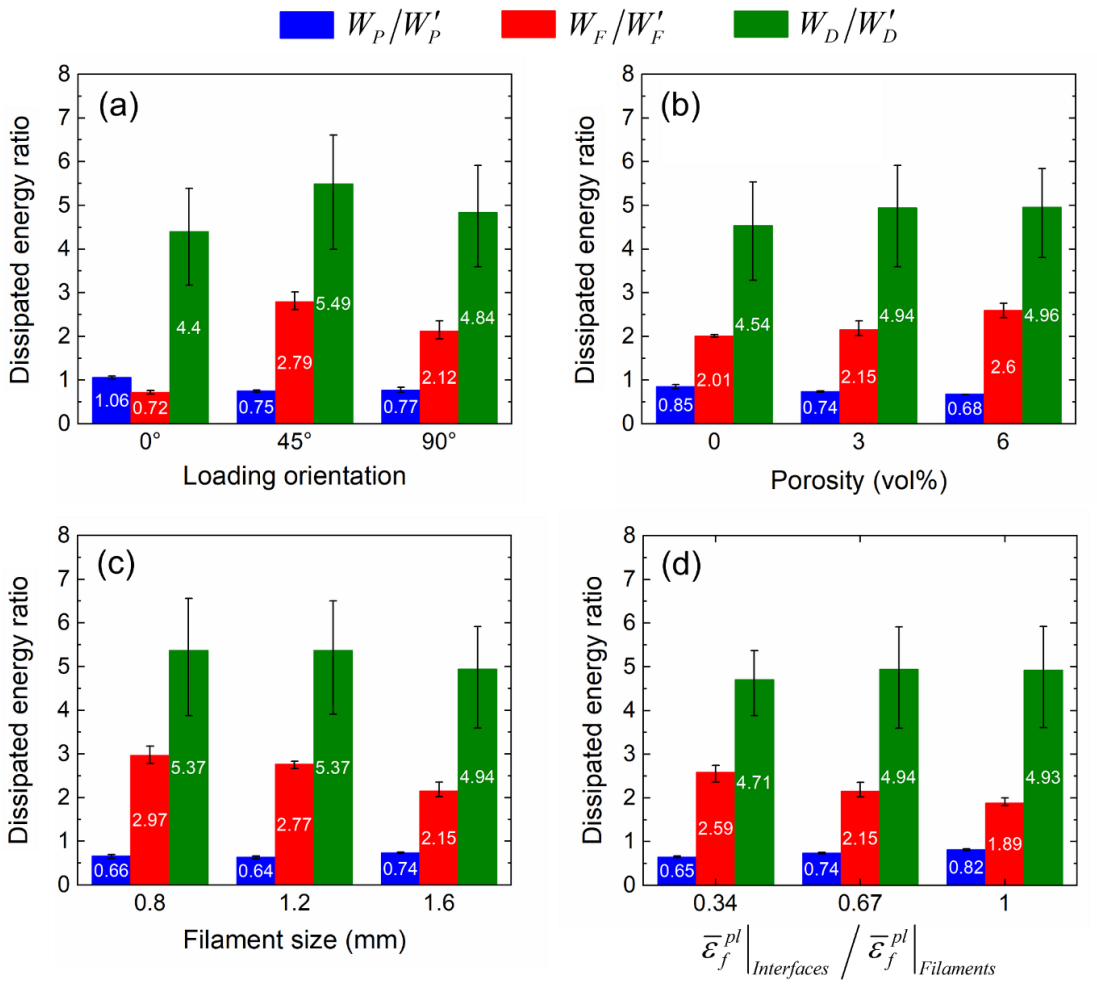

Figure 66 – Ratios of overall dissipated energy in the AM samples to that in the homogenous sample as functions of (a) loading orientation, (b) porosity, (c) filament size, and (d) interfacial strength at $\bar{\varepsilon}$ = 0.35.

5.4 Summary

Simulations are performed to analyze the thermo-mechanical response to dynamic loading of a photopolymer-particulate composite which is considered an AMEM simulant. This material is uni-directionally direct-ink-written. The computations explicitly account for the print structure, with the underlying composite represented with a homogenized constitutive model. Deformation, failure, and heating at the mesoscale are analyzed. To achieve this, an experimentally-informed Lagrangian finite element framework is developed, accounting for finite-strain elastic-plastic deformation, strain-rate effect, arbitrary failure initiation and propagation, post-failure contact and friction, heat generation resulting from friction and inelastic bulk deformation, and heat conduction. The samples generated mimic scanned morphologies of the actual materials used in experiments. Three sets of simulations are performed to quantify the effects of print structure, defects (voids and interfaces), and filament size on energy dissipations associated with different mechanisms, hotspot development, and overall stress evolution.

The sample are loaded at strain rates of 400-2000 s^{-1}. Inelastic and frictional dissipations increase with an increase in the loading rate. Frictional dissipation is more sensitive to the loading rate than plastic dissipation. Among all orientations, loading in the filament direction results in less damage and higher stresses. In contrast, loading at 45 degrees with respect to the filament direction (xy-diagonal direction) yields more intense shear bands and the highest temperatures. In comparison to a homogenous sample, AM samples experience ~3.9 times more damage dissipation at all loading directions. Frictional dissipation significantly depends on the loading direction, ~28% lower in the filament direction and ~146% higher in other directions with respect to a homogeneous sample.

Although friction contributes only $1-4\%$ to total heating, frictional heating is localized at fracture sites and plays a vital role in the development of hotspots. Voids tend to cause damage initiation at earlier stages of deformation. Higher porosities also result in larger hotspots at higher temperatures. Unexpectedly, higher inter-filament strength leads to larger hotspots at higher temperatures due to more intense frictional dissipation at higher internal stresses. Finally, smaller filament sizes cause higher levels of damage and higher dissipation due to interfacial friction.

CHAPTER 6. QUANTITATIVE ASSESSMENT OF INTERIOR DEFORMATION OF AMEM SIMULANT UNDER SHOCK LOADING

This chapter is based on the work published in Ref. [118].

6.1 Introduction

X-ray Phase Contrast Imaging (PCI) is a technique in which the detector is further from the sample (on the order of 1 m) than in traditional radiographic imaging (on the order of 100 mm), and as such both refraction and absorption of x-rays are utilized to create an image. This relatively large sample-to-detector distance allows wave interference due to Fresnel diffraction to appear as further contrast in addition to the already present contrast from x-ray absorption. Gradients in the index of refraction of materials, such as those at material interfaces and the wave front of shocked samples, create interference fringes, which then highlight the interfaces. Synchrotron radiation is uniquely suited to PCI due to its high degree of beam coherence and high flux [127-131]. By combining x-ray PCI with precise timing, it is possible to probe the interior of a material during and following an impact event. This can reveal phenomena that otherwise may not be observable directly. Traditionally, such phenomena have been indirectly studied or inferred from exterior measurements or post-mortem analysis of microstructures. Thus, x-ray PCI can give an unprecedented level of detail due to its high temporal (ns) and spatial (μm) resolutions. Recently, x-ray PCI has been used to study time- and space- resolved responses of porous

periodic metal lattices, granular materials, and energetic (composite) materials during dynamic compression [132-135].

This chapter analyzes the shock compression response of an AMEM simulant along two loading directions with respect to the printing pattern, using high-speed x-ray PCI [133]. This study takes advantage of the observable features associated with the shock wave front, and those behind it, to obtain strain fields in the interior of the opaque samples, via digital image correlation (DIC) analysis. DIC is an optical method that takes advantages of relative changes in a sequence of images [136]. DIC was used in conjunction with high-speed visible light imaging [137, 138], x-ray imaging [139], or X-PCI [140] to quantity the deformation fields during dynamic and impact tests. This study further extend the application of DIC with X-PCI to map the interior strain fields in an opaque 3D-printed material under shock loading.

6.2 Experimental Procedure

6.2.1 Sample Preparation

The samples (2×3×6 mm) for impact experiments were sectioned from the 5×4×2 cm AM fabricated block using a diamond saw (Crystal Systems Corporation Model CU-02) at 50 RPM, controlled with a goniometer to allow accurate cuts along desired orientations. The samples were cut far from the edges of the fabricated block to avoid edge effects. A linear translation stage on the diamond saw was used to ensure that the impact faces were flat and parallel. The densities and dimensions of each sample were measured and their orientations relative to the DIW print and build directions were noted prior to mounting them in 9 mm diameter molds and encasing them in evacuated epoxy consisting

of 70%wt Epon-828 Resin (Miller-Stephenson Chemical Company) and 30%wt Jeffamine T-403 hardener (Huntsman Corporation). The epoxy was cured at 70°C for three hours. Figures 67(a-b) depict schematics of samples along different orientations relative to the print pattern. Miller indices are used to indicate the sample orientations, with red arrows pointing to the impact (loading) directions, and x- and y- axes, respectively, denoting the horizontal and vertical directions constituting the field of view (FOV) of the PCI images obtained from impact experiments described next.

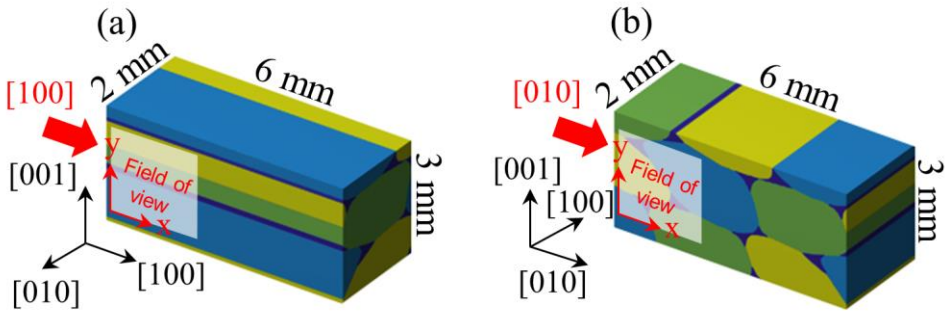

Figure 67 – Illustrations of sample orientations and impact directions with respect to AM printing pattern; (a) loading in the x- or [100]- direction (filament printing direction), and (b) loading in the y- or [010] direction (perpendicular to filament direction in xy-plane).

6.2.2 Plate Impact Experimental Setup

The plate impact experiments were performed using the interchangeable powder/gas gun at the Dynamic Compression Sector (DCS) at the Advanced Photon Source (APS). Figure 68 shows a schematic of the configuration used for performing the plate-impact experiments. The impact velocities ranged from 0.7-1.5 km/s. Solid Al 6061 impactors were used for the experiments. As shown in the schematic in Figure 68, the sample assembly consists of the AMEM simulant sample potted in EPON 828 epoxy, as

described in the previous section. The assembly was machined to a 6 mm diameter cylinder and mounted in a standardized Al holder, with the impact face flush with its surface.

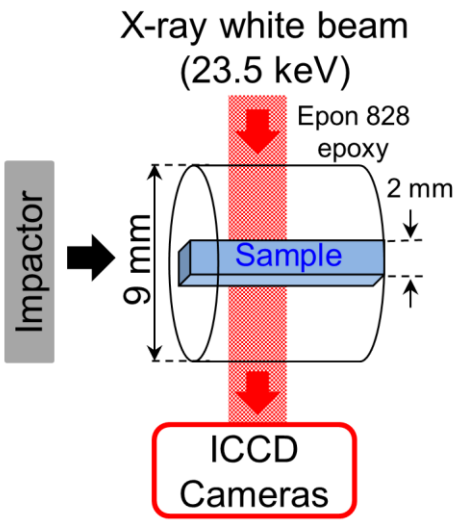

Figure 68 – Configuration of the impact experiment employing non-contact diagnostics, overall layout with solid Al 6061 impactor, AMEM sample assembly, and PCI arrangement [x-ray beam width illustrates field of view (FOV)].

6.2.3 High-speed X-ray Phase Contrast Imaging (PCI)

In-situ multi-frame x-ray phase-contrast imaging was performed on the samples during shock compression and spall experiments. PCI was chosen as a diagnostic tool to observe the effects of shock compression in the AMEM simulant samples and the evolution of the interior strains in the opaque heterogeneous material averaged in the direction of the x-ray beam. Synchrotron x-ray bunches from the APS arrive every 153.4 nanoseconds, transit through the EPON 828 epoxy and the AMEM sample before being detected by a lutetium oxyorthosilicate (LSO) scintillator. The x-rays are converted to visible light by the scintillator and imaged by four individually gated intensified charge couple device (ICCD) PI-MAX-4 cameras (Princeton Instruments, Inc.), which are triggered to coincide with the timing of the x-ray bunches. The timing was achieved by synchronizing the ICCD

triggering, the x-ray bunches, and the impact event through the use of a delay generator and two PZT timing pins. Eight images were obtained by utilizing the dual image feature of the ICCDs, allowing each camera to take two images at least 500 ns apart [141]. The inter-frame time between successive frames of the eight images is 153.4 ns, corresponding to the synchrotron x-ray bunch time. The field of view (FOV) is 2.47 mm wide and ~2 mm high. Although the ICCD images are 2.5×2.5 mm (1024×1024 pixels) in size, the actual FOV on the sample is determined by the slightly smaller dimensions of the x-ray beam, which is approximately 2.2×2.2 mm (900×900 pixels). The samples were oriented such that the x-ray beam always traveled through the 2 mm thickness, limiting the noise in the resulting image. As shown in Figure 67, the impact direction was along the 6 mm length of the sample.

6.3 Results and Discussion

Impact experiments on the AMEM simulant samples were performed at different velocities, with shock propagation along different print directions. The experiments were performed with solid Al 6061 impactors. DIC analysis performed on the phase-contrast images is used to obtain the interior strain fields (averaged in the direction parallel to the x-ray beam) associated with the shock compression.

6.3.1 X-ray Phase Contrast Image Corrections

Since the x-ray phase contrast images were recorded with four different camera units, it is necessary to correct the images for imperfect alignment and adjustment of the cameras. This step reduces error levels in displacement, velocity, and strain calculations. To correct for rotational misalignment and scale, the images from cameras 2, 3, and 4 were

transformed based on a reference image from camera 1 taken before the experiments in order to minimize distortion levels between images recorded by the four cameras. The transformation matrices for the correction were determined by matching sped up robust features (SURF) and recovering the rotation angle and scale factor. First, SURF features were detected in each of the four images. The features were then matched by their descriptors between the reference image (camera 1) and the three reference images from the other three cameras. Outliers were removed before finding a transformation corresponding to the matched point pairs by utilizing the M-estimator Sample Consensus algorithm (MSAC) [142]. After the transformation was verified to appropriately correct the camera misalignments, it was applied to the *in-situ* images for the particular sample from each camera before the DIC analysis was performed.

To estimate distortion levels between static images recorded by the four cameras, DIC analysis was performed on each set of four x-ray images of the stationary and undeformed sample. The image recorded by camera 1 was then used as the reference frame and relative displacement and strain fields in images from cameras 2 to 4 were independently calculated for each experiment. Ideally, these relative deformation and strain fields in images should be zero since the sample in the image was not yet subject to translation or deformation. However, as a result of the misalignments of the cameras, the DIC analysis yielded non-zero displacement and deformation fields. Figure 69 compares the horizontal and vertical displacement error distributions in corrected and uncorrected images recorded by cameras 2 to 4. The maximum displacement error in images recorded by cameras 2 to 4 is ~20 pixels. The correction reduced the error to a negligible level of ~2 pixels (~5 μm). The strain tensor used in this work is the Lagrangian strain [143]. Figure

70(a) shows the longitudinal strain (ε_{xx}) error maps for images recorded by cameras 2 to 4 before the correction. The maximum longitudinal strain error level in all images is $\pm 3\%$. Figure 70(b) shows the corresponding error maps after the corrections were performed. The maximum error was thus reduced to under $\pm 1\%$. Figure 71 shows the probability distribution of the three strain components for the corrected and uncorrected images recorded by cameras 2 to 4. The maximum strain error for all components is decreased from $\pm 3\%$ to $\pm 1\%$ after image correction is performed.

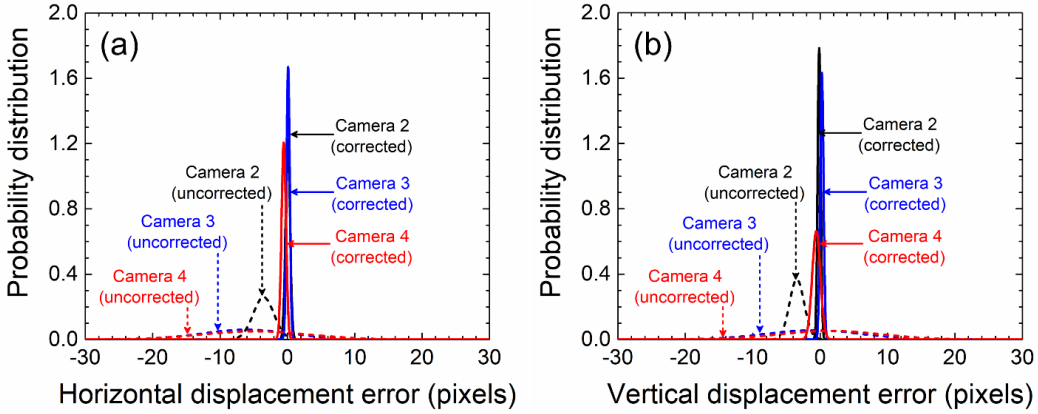

Figure 69 – Distributions of displacement errors in corrected and uncorrected images recorded by cameras 2, 3, and 4 relative to camera 1, (a) horizontal displacement error, and (b) vertical displacement error.

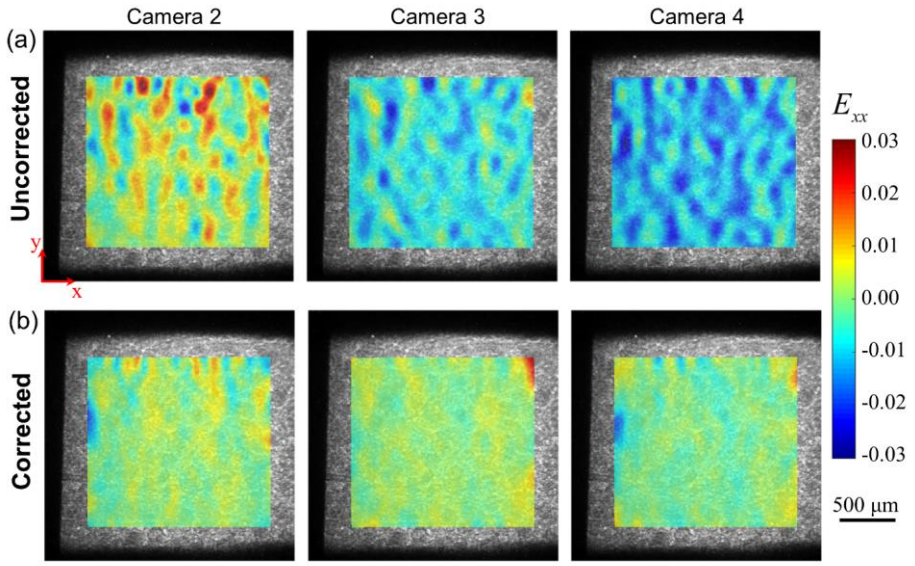

Figure 70 – (a) Longitudinal strain errors $(\Delta\varepsilon_{xx})$ in images recorded by cameras 2, 3, and 4 relative to camera 1, and (b) longitudinal strain errors in cameras 2, 3, and 4 after image corrections.

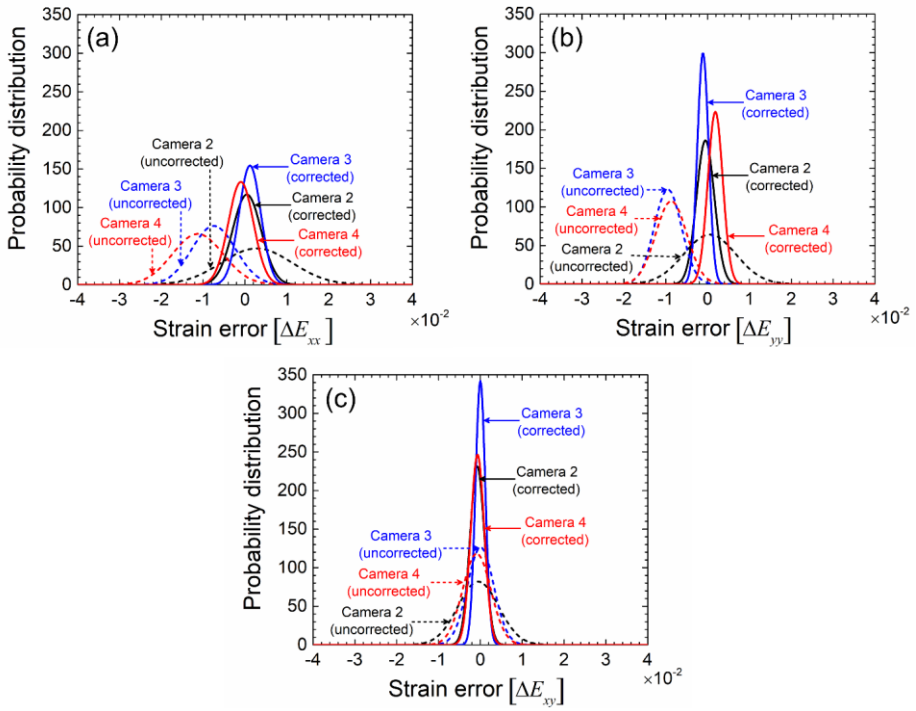

Figure 71 – Distributions of strain errors in corrected and uncorrected images recorded by cameras 2, 3, and 4 relative to camera 1; (a) axial strain error, (b) lateral strain error, and (c) shear strain error.

6.3.2 Strain Distributions

Time-resolved x-ray PCI of shock-compressed samples offers quantitative aggregated information about the deformation in the interior of opaque materials. Such information is generally lacking, owing to the inability to "see" inside a material. Other than the determination of the equation of state (as described above), most work using PCI so far has focused on qualitative observations, such as for resolving critical mechanisms of fracture in brittle silica particles [144] or the powder densification process [132], rather than quantification of "in-material" strains. Figure 72 shows the PCI images for a sample impacted from the left at ~900 m/s with an aluminum 6061 impactor. Loading is along the [001] direction (which corresponds to the build direction) of the AM block. The PCI images are the aggregation of a 3D event onto a 2D plane over a 2 mm sample thickness.

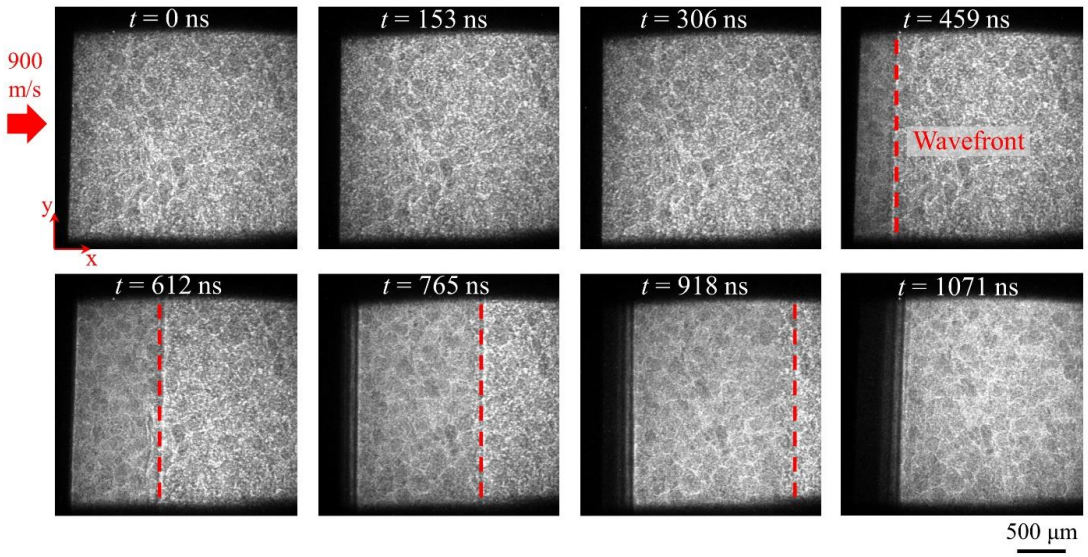

Figure 72 – X-ray phase contrast images for a sample impacted from the left at 900 m/s with an Al 6061 impactor. Loading is along the z-direction (through filaments) of the AM material.

The DIC analysis was carried out with the Ncorr package, an open-source subset-based package with enhanced algorithms [109]. Variations in the index of refraction of the material constituents spawn natural patterns in the x-ray images of the samples. Proper selection of the subset size relative to the characteristic length-scale of the physical features is important in DIC analyses. A subset needs to be large enough to track an arrangement of speckles/features in order to obtain correlation. To compensate for the lack of a speckle pattern here and because of the relatively large strain increment between successive frames (due to the small number of frames available), the subset needs to be large enough to obtain image correlation. A large circular subset with a diameter of 0.37 mm (150 pixels) was used (see Figure 73). Smaller subsets than this size yield incomplete and noisy strain fields.

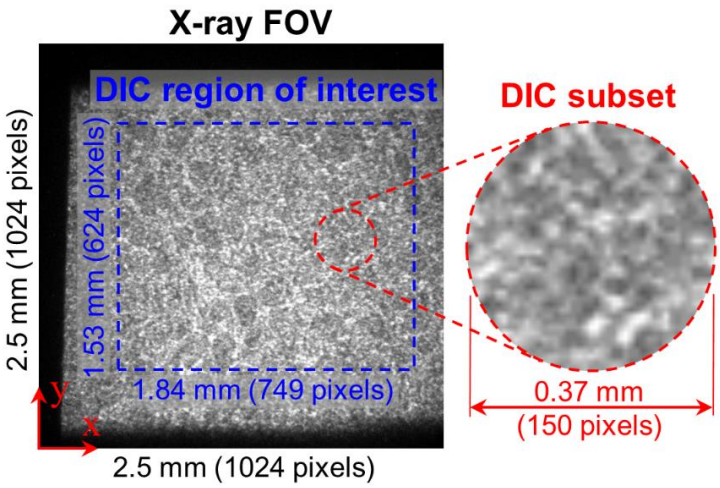

Figure 73 – An x-ray PCI image, DIC region of interest (ROI), and the DIC subset.

Figure 74 shows the evolution of the longitudinal Lagrangian strain (ε_{xx}) field. The sample is impacted by an Al 6061 impactor at ~0.9 km/s along the [010] direction. It can be seen that the strain field is rather uniform in the lateral (y) direction and there is a gradual rise in strain along the impact direction, which is attributed to the use of a large

subset size. Figure 75 shows the variations of the longitudinal strain (ε_{xx}), the lateral strain (ε_{yy}), and the shear strain (ε_{xy}) along the impact direction at the four times depicted in Figure 74. Figure 75(a) compares the sequence of longitudinal Lagrangian strain (ε_{xx}) profiles, showing the longitudinal strain level reaches a maximum of ~0.2 and remains at this plateau level as the wave propagates. Figures 75(b) and 75(c) show the variations of ε_{yy} and ε_{xy}, respectively. Both have magnitudes below 0.02 which is primarily within experimental error arising from the 3D nature of the deformation, since at the overall sample size scale these strain components should average out to zero for the uniaxial strain conditions of the experiment.

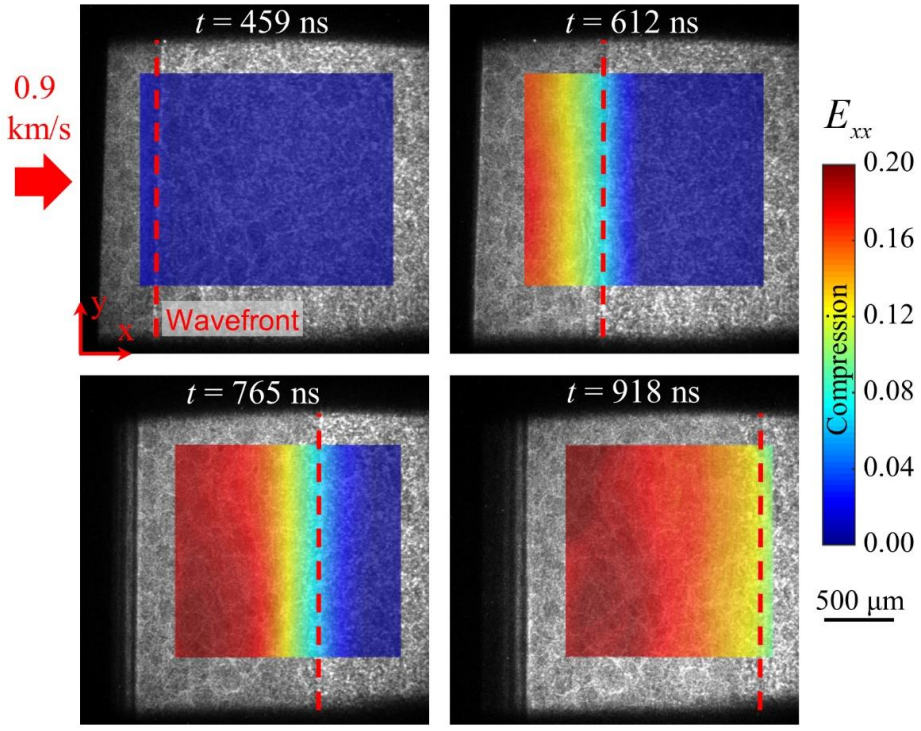

Figure 74 – Distributions of the longitudinal Lagrangian strain in a sample impacted along the [010]-direction by a 6061 Al impactor at 0.9 km/s.

The macroscopically uniaxial strain conditions of planar plate impact loading of a cylindrical sample involve primary motion of material points in the direction of impact. Material heterogeneities and microstructure cause 3D interior particle motion; however, the lateral displacements in the y-direction (vertical) and the z-direction (normal to the image plane which is also the direction of the x-ray beam) as shown in Figure 75 are relatively small compared with the displacement in the impact direction (x-direction). Also, since the heterogeneities are random, the lateral displacements fluctuate without clear preferred direction over significant size and time scales.

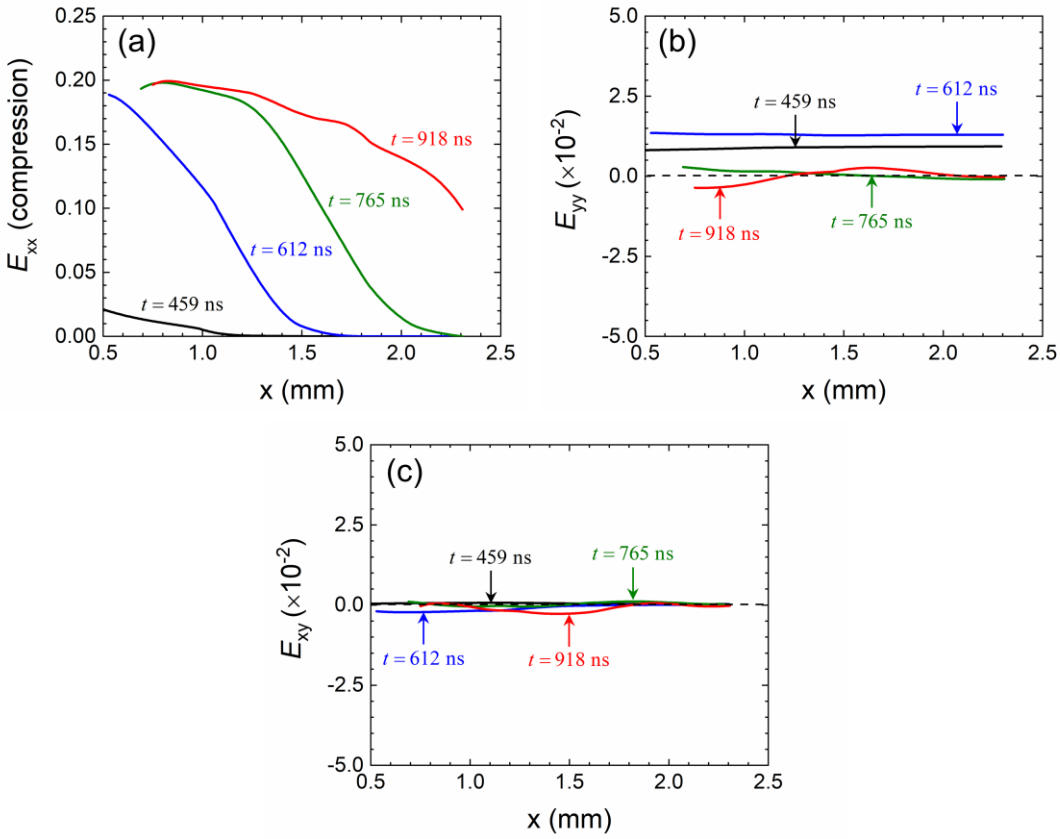

Figure 75 – Variations of the strains along the loading direction in a sample impacted along the [010]-direction [Figure 67(b)] by a 6061 Al impactor at 0.9 km/s; (a) ε_{xx}, (b) ε_{yy}, and (c) ε_{xy}.

Figure 76 compares the profiles of the longitudinal strain at the same time (approximately $t = 765$ ns) for two sets of samples, one set impacted along the [100] direction and the other set impacted along the [010]. Each set has three samples, impacted at velocities of 0.9, 1.2, and 1.5 km/s, respectively. Both loading directions exhibit similar behaviors, while the plateau strain level increases with impact velocity. The wave-front widths obtained from DIC depend on the subset size. A larger subset leads to a wider wave-front since DIC smooths out localized deformations over the subset size. To resolve this issue, the wave-front widths are more accurately calculated according to the x-ray PCI measurements. The results are shown in Figure 76 with dotted lines.

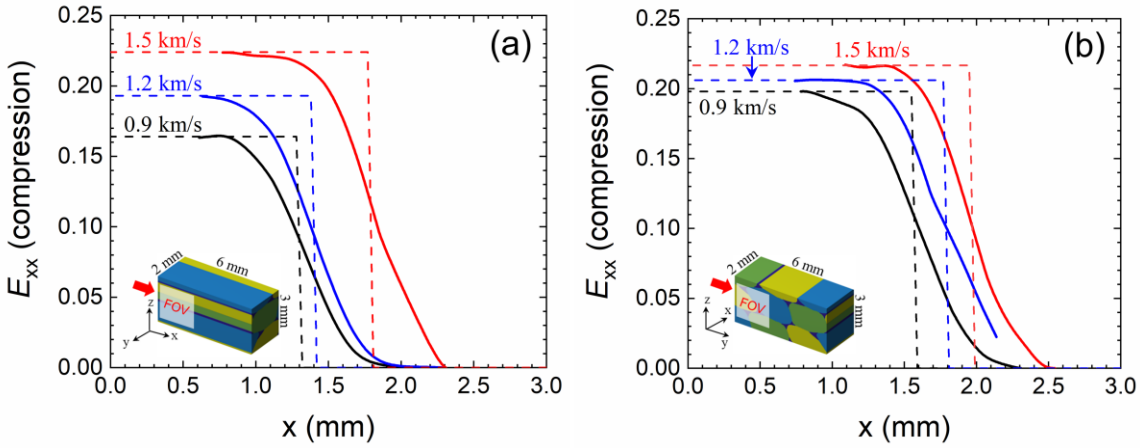

Figure 76 – Variations of the longitudinal Lagrangian strain at approximately $t = 765$ ns for samples impacted at different velocities between 0.9-1.5 km/s, (a) loading along the [100] direction, and (b) loading along the [010] direction.

It should be noted that the use and associated interpretation of DIC performed in the present work are somewhat different from the application of DIC with images of evolving surface speckle patterns. The DIC images used here are 2D patterns resulting from the aggregated rendering of 3D interactions between x-rays and material microstructure. As a result, the strain fields obtained are only approximate and average, they do not represent

the deformation fields in any plane or 2D cross-section. As such, the fields so obtained do not sufficiently resolve fine local features of local strains such as shear bands. However, it is important to recognize that the evolution of the PCI image patterns indeed results from the deformation of the material, and therefore, reflects the strain. Hence, estimation of the overall strain levels, especially in the axial or impact direction, which is the primary direction of specimen particle motion, is possible. It should also be noted that the subset size of the images used here is relatively large (~370 μm), consequently, the focus is on the overall trend and level, rather than local details (e.g., at the shock front).

The strain fields obtained from the DIC analyses of the x-ray PCI images provide insight into the interior shock response of a heterogeneous material (AMEM simulant). While the technique is quite useful, it only provides an average view of the overall strain variations and not the details of local strain distribution, owing to the fact that PCI images are 2D aggregate representations of heterogeneous 3D deformations. As such averaging over a significantly large area around each image location is necessary. The subset size used here is ~370 μm. The analysis is also made possible by the overall macroscopic uniaxial strain nature of the shock compression experiment. Microstructural features such as in composite systems with particles sizes of the order of 100 μm, or larger, can also function as a speckle pattern in regular DIC analyses.

6.4 Summary

The response to shock loading of an additively manufactured energetic material simulant along two directions relative to the print pattern is experimentally investigated. The samples were sectioned from a larger as-printed block. Time-resolved x-ray phase-contrast imaging (PCI) was used as an interior in-material diagnostic with ~154 ns time resolution and 2.45-micron spatial resolution. Digital image correlation (DIC) analysis was performed to determine the interior strains using the *in-situ* x-ray PCI images. The calculated axial strains increase with shock intensity, with a maximum level of ~22% at an impact velocity of 1.5 km/s. Consistent with the conditions of the overall uniaxial impact, the strains in the two lateral directions are negligible.

CHAPTER 7. SUMMARY AND FUTURE DIRECTIONS

7.1 Summary

This dissertation contributes to the overall understanding of the thermo-mechanical response of traditionally manufactured polymer-bonded explosives (PBX9501 and variants) and an additively manufactured energetic material (AMEM) simulant to dynamic loading. A Lagrangian cohesive finite element framework is used to analyze the thermo-mechanical response and ignition behavior of PBX9501 and its variants. The ignition probability, the dissipation mechanisms, the damage evolution, and the hotspot characteristics are quantified and analyzed. The results are compared with available experimental results for PBX9501.

The AMEM simulant is high solid-loaded photopolymer manufactured using the direct ink writing (DIW) process and cured with Ultraviolet (UV) light. AMEMs have a wide range of structural characteristics with a hierarchy of length scales and process-inherent heterogeneities which are hitherto difficult to precisely control. It is important to understand how these features affect AMEMs' response under dynamic/shock loading. Using the best diagnostics available, and new experimental capabilities and computational frameworks developed, this study establishes trends in and quantification of the relations between structure and response of a class of additively manufactured photopolymer-particulate composites.

Chapter 1 provides a background on the topic of thermo-mechanical response of energetic materials, challenges and opportunities of additive manufacturing of energetic materials, and the layout of this dissertation.

Chapter 2 quantifies the relative importance of the contributions of plasticity and internal friction to dissipation and heating in traditionally manufactured PBXs. The results show that plastic deformation of the energetic grains of the heterogeneous PBXs significantly influence their response and ignition behavior. The time to ignition is analyzed and quantified using the Weibull distribution function, providing explicit expressions for the ignition probability as a function of load intensity and HMX yield strength. The 50% ignition thresholds obtained are analyzed and presented in a load-intensity-load duration relation $\left(P^2 t_{50} = C\right)$.

Chapter 3 reports the development of a novel capability (MINTED, or microscale in-situ imaging of temperature and deformation fields under dynamic loading) for time-resolved and space-resolved measurements of the temperature and deformation fields at the microstructure level for dynamic conditions is developed. The method integrates a state-of-the-art high-speed infrared (IR) camera and a high-speed visible light (VL) camera in a split-Hopkinson pressure bar (SHPB) or Kolsky bar apparatus. To simultaneously capture deformation and temperature fields at normal incidence, the visible (VL) and infrared (IR) emissions from the sample are separated by a dichroic beam splitter. To demonstrate the capabilities of the MINTED system, experiments are performed on sucrose granules, which are widely used as a simulant of energetic crystals.

Chapter 4 analyzes the orientation-dependence thermo-mechanical response of the AMEM simulant to dynamic loading. Experiments and multi-physics computations are performed to relate localized deformation, dissipation mechanisms, and temperature rises to the print structure. The mesoscale deformation, failure, and heating of the material under loading along four different directions with respect to the print structure are studied. The MINTED system is used to obtain deformation and temperature fields over the same area of samples with micrometer spatial and microsecond temporal resolutions. Loading along different directions relative to the print structure of the material is achieved using a SHPB apparatus at the average strain rate of ~300 s^{-1}. Simulations accounting for the geometry and print structure of the samples are performed. The simulations performed focus on failure initiation and the contributions to heating, and interplays between plasticity and internal friction.

Built upon Chapter 4, Chapter 5 further analyzes the mesoscale thermo-mechanical response of the AMEM simulant under dynamic loading. The analysis focuses on the effects of print structure, porosity, inter-filament strength, and filament size on overall thermo-mechanical behavior at intermediate strain rates.

Finally, Chapter 6 experimentally investigates the response to shock loading of an additively manufactured energetic material simulant along two directions relative to the print pattern. Digital image correlation (DIC) analysis was performed to determine the interior strains using the *in-situ* x-ray phase contrast images.

7.2 Future Directions

While this dissertation serves as an essential stepping stone to further the overall understanding of thermo-mechanical response of energetic materials to dynamic loading, there are always improvements to be made. The following are worthwhile topics for future studies.

1. This dissertation is focused on uni-directionally printed materials with low overall porosities. Further studies should also consider other structures and wider ranges of heterogeneities.
2. The computations performed in Chapters 4 and 5 focus on the print structure level and use a homogenized material constitutive model that is informed by the mesoscale experiments. It will be interesting to explicitly account for microstructure constituents including the grains and the polymer binder and investigate the effects of microstructure attributes on overall response. To this effect, multi-scale simulations are essential.
3. Future studies should aim to quantify ignition and shock-to-detonation transition (SDT) behavior of AMEMs under a range of loading conditions, leading to the development of relations between the response, loading, print structure, and material/structural heterogeneities. Ultimately, these relations are expected to provide guidance for the development of new AMEMs, refinement of AM processes to achieve material quality control, quantification of uncertainties in response, and prediction of performance.

REFERENCES

1. Hartley, K.A., J. Duffy, and R.H. Hawley, *Measurement of the temperature profile during shear band formation in steels deforming at high strain rates.* Journal of the Mechanics and Physics of Solids, 1987. **35**(3): p. 283-301.

2. Marchand, A. and J. Duffy, *An experimental study of the formation process of adiabatic shear bands in a structural steel.* Journal of the Mechanics and Physics of Solids, 1988. **36**(3): p. 251-283.

3. Zhou, M., A.J. Rosakis, and G. Ravichandran, *Dynamically propagating shear bands in impact-loaded prenotched plates—I. Experimental investigations of temperature signatures and propagation speed.* Journal of the Mechanics and Physics of Solids, 1996. **44**(6): p. 981-1006.

4. Guduru, P.R., A.J. Rosakis, and G. Ravichandran, *Dynamic shear bands: an investigation using high speed optical and infrared diagnostics.* Mechanics of Materials, 2001. **33**(7): p. 371-402.

5. Li, Z. and J. Lambros, *Strain rate effects on the thermomechanical behavior of polymers.* International Journal of Solids and Structures, 2001. **38**(20): p. 3549-3562.

6. Li, Z. and J. Lambros, *Dynamic thermomechanical behavior of fiber reinforced composites.* Composites Part A: Applied Science and Manufacturing, 2000. **31**(6): p. 537-547.

7. Goretta, K.C., et al., *Thermomechanical response of polycrystalline BaZrO3.* Physica C: Superconductivity, 1998. **309**(3): p. 245-250.

8. Mukherjee, K., S. Sircar, and N.B. Dahotre, *Thermal effects associated with stress-induced martensitic transformation in a Ti-Ni alloy.* Materials Science and Engineering, 1985. **74**(1): p. 75-84.

9. McCormick, P.G., Y. Liu, and S. Miyazaki, *Intrinsic thermal-mechanical behaviour associated with the stress-induced martensitic transformation in NiTi.* Materials Science and Engineering: A, 1993. **167**(1): p. 51-56.

10. Field, J., et al., *Hot-spot ignition mechanisms for explosives and propellants [and discussion].* Philosophical Transactions of the Royal Society of London A: Mathematical, Physical and Engineering Sciences, 1992. **339**(1654): p. 269-283.

11. Field, J.E., G.M. Swallowe, and S.N. Heavens, *Ignition Mechanisms of Explosives during Mechanical Deformation.* Proceedings of the Royal Society of London. A. Mathematical and Physical Sciences, 1982. **382**(1782): p. 231-244.

12. Tarver, C.M., S.K. Chidester, and A.L. Nichols, *Critical Conditions for Impact- and Shock-Induced Hot Spots in Solid Explosives.* The Journal of Physical Chemistry, 1996. **100**(14): p. 5794-5799.

13. Winter, R.E. and J.E. Field, *The Role of Localized Plastic Flow in the Impact Initiation of Explosives.* Proceedings of the Royal Society of London. A. Mathematical and Physical Sciences, 1975. **343**(1634): p. 399-413.

14. Guirguis, R.H., *Ignition due to macroscopic shear.* AIP Conference Proceedings, 2000. **505**(1): p. 647-650.

15. Skidmore, C., et al. *Microstructural effects in PBX 9501 damaged by shear impact*. in *AIP Conference Proceedings*. 2000. AIP.

16. Menikoff, R., *Elastic-plastic response of HMX.* Research Highlights, 2005.

17. Swallowe, G.M. and J.E. Field, *The Ignition of a Thin Layer of Explosive by Impact; the Effect of Polymer Particles.* Proceedings of the Royal Society of London. A. Mathematical and Physical Sciences, 1982. **379**(1777): p. 389-408.

18. Barua, A., Y. Horie, and M. Zhou, *Microstructural level response of HMX–Estane polymer-bonded explosive under effects of transient stress waves.* Proceedings of the Royal Society of London A: Mathematical, Physical and Engineering Sciences, 2012. **468**(2147): p. 3725-3744.

19. Barua, A., et al., *Ignition criterion for heterogeneous energetic materials based on hotspot size-temperature threshold.* Journal of Applied Physics, 2013. **113**(6): p. 064906.

20. Barua, A. and M. Zhou, *A Lagrangian framework for analyzing microstructural level response of polymer bonded explosives.* Modeling and Simulation in Materials Science and Engineering, 2011. **19**(055001): p. 1-24.

21. Barua, A. and M. Zhou, *A Framework for Analyzing the Microstructure Level Thermomechanical Response of Polymer Bonded Explosives.* Materials Science Forum, 2011. **673**: p. 21-33.

22. Kim, S., et al., *Ignition probability of polymer-bonded explosives accounting for multiple sources of material stochasticity.* Journal of Applied Physics, 2014. **115**(17): p. 174902.

23. Kim, S., Y. Horie, and M. Zhou, *Ignition Desensitization of PBX via Aluminization.* Metallurgical and Materials Transactions A, 2015. **46**(10): p. 4578-4586.

24. Kim, S., et al., *Computational prediction of probabilistic ignition threshold of pressed granular octahydro-1, 3, 5, 7-tetranitro-1, 2, 3, 5-tetrazocine (HMX) under shock loading.* Journal of Applied Physics, 2016. **120**(11): p. 115902.

25. Herzog, D., et al., *Additive manufacturing of metals.* Acta Materialia, 2016. **117**: p. 371-392.

26. Frazier, W.E., *Metal Additive Manufacturing: A Review*. Journal of Materials Engineering and Performance, 2014. **23**(6): p. 1917-1928.

27. Wong, K.V. and A. Hernandez, *A review of additive manufacturing.* ISRN Mechanical Engineering, 2012. **2012**.

28. Murray, A.K., et al., *Two-component additive manufacturing of nanothermite structures via reactive inkjet printing.* Journal of Applied Physics, 2017. **122**(18): p. 184901.

29. Fleck, T.J., et al., *Additive manufacturing of multifunctional reactive materials.* Additive Manufacturing, 2017. **17**: p. 176-182.

30. Wang, H., et al., *Electrospray formation and combustion characteristics of iodine-containing Al/CuO nanothermite microparticles.* Combustion and Flame, 2015. **162**(7): p. 2823-2829.

31. Wang, H., et al., *Assembly and reactive properties of Al/CuO based nanothermite microparticles.* Combustion and Flame, 2014. **161**(8): p. 2203-2208.

32. Huang, C., et al., *Electrospray deposition of energetic polymer nanocomposites with high mass particle loadings: a prelude to 3D printing of rocket motors.* Advanced Engineering Materials, 2015. **17**(1): p. 95-101.

33. Ihnen, A.C., et al., *Ink jet printing and patterning of explosive materials*. 2016, Stevens Institute of Technology, US Secretary of Army: United States.

34. Ruz-Nuglo, F., L. Groven, and J.A. Puszynski, *Additive manufacturing for energetic components and materials*, in *50th AIAA/ASME/SAE/ASEE Joint Propulsion Conference*. 2014. p. 3894.

35. Tappan, A.S., J.P. Ball, and J.W. Colovos, *Inkjet Printing of Energetic Materials: Sub-Micron Al/MoO3 and Al/Bi2O3 Thermite*. 2012, Sandia National Lab.(SNL-NM), Albuquerque, NM (United States).

36. Chrisey, D.B., *The power of direct writing.* Science, 2000. **289**(5481): p. 879-881.

37. Lewis, J.A. and G.M. Gratson, *Direct writing in three dimensions.* Materials today, 2004. **7**(7-8): p. 32-39.

38. Stansbury, J.W. and M.J. Idacavage, *3D printing with polymers: Challenges among expanding options and opportunities.* Dental Materials, 2016. **32**(1): p. 54-64.

39. Oropallo, W. and L.A. Piegl, *Ten challenges in 3D printing.* Engineering with Computers, 2016. **32**(1): p. 135-148.

40. McClain, M., I. Gunduz, and S. Son, *Additive manufacturing of ammonium perchlorate composite propellant with high solids loadings.* Proceedings of the Combustion Institute, 2019. **37**(3): p. 3135-3142.

41. Lewis, J.A., *Direct ink writing of 3D functional materials.* Advanced Functional Materials, 2006. **16**(17): p. 2193-2204.

42. Lee, C., et al., *Measurement of anisotropic compressive strength of rapid prototyping parts.* Journal of materials processing technology, 2007. **187**: p. 627-630.

43. Ahn, S.-H., et al., *Anisotropic material properties of fused deposition modeling ABS.* Rapid prototyping journal, 2002. **8**(4): p. 248-257.

44. Mueller, A., et al., *Diameter effects on the directional anisotropic detonation behavior of strand structured additively manufactured explosives.* Bulletin of the American Physical Society, 2019. **64**(8): p. 63.

45. O'Grady, C., et al., *Investigating Typical Additive Manufacturing Defect Geometries using Physical Vapor Deposition Explosives as a Model System.* Bulletin of the American Physical Society, 2019. **64**(8): p. 63.

46. Barua, A., et al., *Prediction of probabilistic ignition behavior of polymer-bonded explosives from microstructural stochasticity.* Journal of Applied Physics, 2013. **113**(18): p. 184907.

47. Keyhani, A., et al., *Energy dissipation in polymer-bonded explosives with various levels of constituent plasticity and internal friction.* Computational Materials Science, 2019. **159**: p. 136-149.

48. Wu, Y. and F. Huang, *A micromechanical model for predicting combined damage of particles and interface debonding in PBX explosives.* Mechanics of Materials, 2009. **41**(1): p. 27-47.

49. Mas, E.M., et al., *Finite Element Method Calculations on Statistically Consistent Microstructures of PBX 9501.* AIP Conference Proceedings, 2006. **845**(1): p. 487-490.

50. Benson, D.J. and P. Conley, *Eulerian finite-element simulations of experimentally acquired HMX microstructures.* Modelling and Simulation in Materials Science and Engineering, 1999. **7**(3): p. 333.

51. Menikoff, R. and T.D. Sewell, *Constituent properties of HMX needed for mesoscale simulations.* Combustion theory and modelling, 2002. **6**(1): p. 103-125.

52. Green, L., A. Weston, and J. Van Velkinburg, *MECHANICAL AND FRICTIONAL BEHAVIOR OF SKID TEST HEMISPHERICAL BILLETS.* 1971, California Univ., Livermore. Lawrence Livermore Lab.

53. Dickson, P., et al. *Frictional heating and ignition of energetic materials*. in *AIP Conference Proceedings*. 2006. AIP.

54. Kapahi, A. and H. Udaykumar, *Three-dimensional simulations of dynamics of void collapse in energetic materials.* Shock Waves, 2015. **25**(2): p. 177-187.

55. Barton, N.R., N.W. Winter, and J.E. Reaugh, *Defect evolution and pore collapse in crystalline energetic materials.* Modelling and Simulation in Materials Science and Engineering, 2009. **17**(3): p. 035003.

56. Tran, L. and H. Udaykumar, *Simulation of void collapse in an energetic material, Part 2: reactive case.* Journal of propulsion and power, 2006. **22**(5): p. 959-974.

57. Austin, R.A., et al., *Direct numerical simulation of shear localization and decomposition reactions in shock-loaded HMX crystal.* Journal of Applied Physics, 2015. **117**(18): p. 185902.

58. Yarrington, C.D., R.R. Wixom, and D.L. Damm, *Shock interactions with heterogeneous energetic materials.* Journal of Applied Physics, 2018. **123**(10): p. 105901.

59. Rai, N.K. and H.S. Udaykumar, *Three-dimensional simulations of void collapse in energetic materials.* Physical Review Fluids, 2018. **3**(3): p. 033201.

60. Mas, E.M., et al., *A Viscoelastic Model for PBX Binders.* AIP Conference Proceedings, 2002. **620**(1): p. 661-664.

61. Zhou, M., A. Needleman, and R.J. Clifton, *Finite element simulations of shear localization in plate impact.* Journal of the Mechanics and Physics of Solids, 1994. **42**(3): p. 423-458.

62. Landerville, A.C., et al., *Equations of state for energetic materials from density functional theory with van der Waals, thermal, and zero-point energy corrections.* Applied Physics Letters, 2010. **97**(25): p. 251908.

63. Zhai, J., V. Tomar, and M. Zhou, *Micromechanical simulation of dynamic fracture using the cohesive finite element method.* Transactions-American society of mechanical engineers Journal of Engineering Materials and Technology, 2004. **126**(2): p. 179-191.

64. Terao, K., *Irreversible Phenomena: Ignitions, Combustion, and Detonation Waves*. 2007: Springer.

65. Rae, P., et al. *Quasi–static studies of the deformation and failure of PBX 9501*. in *Proceedings of the Royal Society of London A: Mathematical, Physical and Engineering Sciences*. 2002. The Royal Society.

66. Gray, G.T., et al., *Influence of temperature on the high-strain-rate mechanical behavior of PBX 9501.* AIP Conference Proceedings, 1998. **429**(1): p. 583-586.

67. Keyhani, A., R. Yang, and M. Zhou, *Novel Capability for Microscale In-situ Imaging of Temperature and Deformation Fields under Dynamic Loading.* Experimental Mechanics, 2019. **59**(5): p. 775-790.

68. Ravindran, S., A. Tessema, and A. Kidane, *Multiscale damage evolution in polymer bonded sugar under dynamic loading.* Mechanics of Materials, 2017. **114**: p. 97-106.

69. Bloomquist, D. and S. Sheffield, *Shock-compression temperature rise in polymethyl methacrylate determined from resistivity of embedded copper foils.* Applied Physics Letters, 1981. **38**(3): p. 185-187.

70. Bloomquist, D. and S. Sheffield, *Thermocouple temperature measurements in shock-compressed solids.* Journal of Applied Physics, 1980. **51**(10): p. 5260-5266.

71. Boboridis, K. and A.W. Obst. *A High-Speed Four-Channel Infrared Pyrometer*. in *AIP Conference Proceedings*. 2003. AIP.

72. Long, D.A. and D. Long, *Raman spectroscopy*. Vol. 276. 1977: McGraw-Hill New York.

73. Yuan, V., et al., *Shock temperature measurement using neutron resonance spectroscopy.* Physical review letters, 2005. **94**(12): p. 125504.

74. Dolan, D.H., T. Ao, and C.T. Seagle. *Reflectance thermometry in dynamic compression experiments*. in *AIP Conference Proceedings*. 2013. AIP.

75. Dolan, D.H., C.T. Seagle, and T. Ao, *Dynamic temperature measurements with embedded optical sensors.* SANDIA Report No. SAND2013-8203, 2013.

76. Coffey, C. and S. Jacobs, *Detection of local heating in impact or shock experiments with thermally sensitive films.* Journal of Applied Physics, 1981. **52**(11): p. 6991-6993.

77. Zehnder, A.T. and A.J. Rosakis, *On the temperature distribution at the vicinity of dynamically propagating cracks in 4340 steel.* Journal of the Mechanics and Physics of Solids, 1991. **39**(3): p. 385-415.

78. Zhou, M., G. Ravichandran, and A.J. Rosakis, *Dynamically propagating shear bands in impact-loaded prenotched plates—II. Numerical simulations.* Journal of the Mechanics and Physics of Solids, 1996. **44**(6): p. 1007-1032.

79. Costin, L., et al., *On the localisation of plastic flow in mild steel tubes under dynamic torsional loading.* Proc. 2 nd Conf. Mechanical Properties of Materials at High Rates of Strain, Oxford, England, 1980: p. 90-100.

80. Soudre-Bau, L., et al., *Combined Temperature and Deformation Measurement During Glass Forming in a Real Scale Setup.* Experimental Mechanics, 2013. **53**(9): p. 1773-1781.

81. Bodelot, L., et al., *Experimental study of heterogeneities in strain and temperature fields at the microstructural level of polycrystalline metals through fully-coupled full-field measurements by Digital Image Correlation and Infrared Thermography.* Mechanics of Materials, 2011. **43**(11): p. 654-670.

82. Bodelot, L., et al., *Experimental setup for fully coupled kinematic and thermal measurements at the microstructure scale of an AISI 316L steel.* Materials Science and Engineering: A, 2009. **501**(1): p. 52-60.

83. Bertram Hopkinson, F.R.S., *A method of measuring the pressure produced in the detonation of high, explosives or by the impact of bullets.* Philosophical Transactions of the Royal Society of London, 1914. **213**(497-508): p. 437-456.

84. Kolsky, H., *An investigation of the mechanical properties of materials at very high rates of loading.* Proceedings of the physical society. Section B, 1949. **62**(11): p. 676.

85. Davies, E.D.H. and S.C. Hunter, *The dynamic compression testing of solids by the method of the split Hopkinson pressure bar.* Journal of the Mechanics and Physics of Solids, 1963. **11**(3): p. 155-179.

86. Staab, G.H. and A. Gilat, *A direct-tension split Hopkinson bar for high strain-rate testing.* Experimental Mechanics, 1991. **31**(3): p. 232-235.

87. Gilat, A. and C.-S. Cheng, *Torsional split Hopkinson bar tests at strain rates above 104s−1.* Experimental Mechanics, 2000. **40**(1): p. 54-59.

88. Hartley, K., J. Duffy, and R. Hawley, *The torsional Kolsky (split-Hopkinson) bar.* ASM metals handbook, 1985. **8**: p. 218-228.

89. Wang, Q.Z., W. Li, and H.P. Xie, *Dynamic split tensile test of Flattened Brazilian Disc of rock with SHPB setup.* Mechanics of Materials, 2009. **41**(3): p. 252-260.

90. Grantham, S.G., et al., *High-strain rate Brazilian testing of an explosive simulant using speckle metrology.* Measurement Science and Technology, 2004. **15**(9): p. 1867.

91. Jiang, F. and K.S. Vecchio, *Hopkinson Bar Loaded Fracture Experimental Technique: A Critical Review of Dynamic Fracture Toughness Tests.* Applied Mechanics Reviews, 2009. **62**(6): p. 060802-060802-39.

92. Chen, R., et al., *Determination of dynamic fracture parameters using a semi-circular bend technique in split Hopkinson pressure bar testing.* Engineering Fracture Mechanics, 2009. **76**(9): p. 1268-1276.

93. Wang, Q.Z., et al., *Measurement of mode I and mode II rock dynamic fracture toughness with cracked straight through flattened Brazilian disc impacted by split Hopkinson pressure bar.* Engineering Fracture Mechanics, 2011. **78**(12): p. 2455-2469.

94. Zhao, H. and G. Gary, *A new method for the separation of waves. Application to the SHPB technique for an unlimited duration of measurement.* Journal of the Mechanics and Physics of Solids, 1997. **45**(7): p. 1185-1202.

95. Bacon, C., *An experimental method for considering dispersion and attenuation in a viscoelastic Hopkinson bar.* Experimental Mechanics, 1998. **38**(4): p. 242-249.

96. Bacon, C., *Separation of waves propagating in an elastic or viscoelastic Hopkinson pressure bar with three-dimensional effects.* International Journal of Impact Engineering, 1999. **22**(1): p. 55-69.

97. Frew, D., M.J. Forrestal, and W. Chen, *A split Hopkinson pressure bar technique to determine compressive stress-strain data for rock materials.* Experimental mechanics, 2001. **41**(1): p. 40-46.

98. Song, B. and W. Chen, *Dynamic stress equilibration in split Hopkinson pressure bar tests on soft materials.* Experimental Mechanics, 2004. **44**(3): p. 300-312.

99. Othman, R. The Kolsky-Hopkinson Bar Machine: Selected Topics, ed. R. Othman. 2018, Cham: Springer International Publishing.

100. Lindholm, U.S., *Some experiments with the split hopkinson pressure bar∗.* Journal of the Mechanics and Physics of Solids, 1964. **12**(5): p. 317-335.

101. Noble, J.P., et al., *The use of the Hopkinson bar to validate constitutive relations at high rates of strain.* Journal of the Mechanics and Physics of Solids, 1999. **47**(5): p. 1187-1206.

102. Chen, J.J., et al., *Dynamic Brazilian Test of Brittle Materials Using the Split Hopkinson Pressure Bar and Digital Image Correlation.* Strain, 2014. **50**(6): p. 563-570.

103. Hudspeth, M., et al., *High speed synchrotron x-ray phase contrast imaging of dynamic material response to split Hopkinson bar loading.* Review of Scientific Instruments, 2013. **84**(2): p. 025102.

104. Yeager, J.D., et al., *Development of inert density mock materials for HMX*. Journal of Energetic Materials, 2018. **36**(3): p. 253-265.

105. Ramos, K. and D. Bahr, *Mechanical behavior assessment of sucrose using nanoindentation.* Journal of materials research, 2007. **22**(7): p. 2037-2045.

106. Hardman, J. and B. Lilley, *Deformation of particles during briquetting.* Nature, 1970. **228**(5269): p. 353.

107. Huffine, C.L., *A study of the bonding and cohesion achieved in the compression of particulate materials*. 1953, Columbia University: New York City, New York.

108. Bridgman, P.W., *Physics of high pressure.* 1952.

109. Blaber, J., B. Adair, and A. Antoniou, *Ncorr: Open-Source 2D Digital Image Correlation Matlab Software*. Experimental Mechanics, 2015. **55**(6): p. 1105-1122.

110. Pan, B., *Reliability-guided digital image correlation for image deformation measurement.* Applied Optics, 2009. **48**(8): p. 1535-1542.

111. Pan, B., et al., *Full-field strain measurement using a two-dimensional Savitzky-Golay digital differentiator in digital image correlation.* Optical Engineering, 2007. **46**(3).

112. Rubino, V., A.J. Rosakis, and N. Lapusta, *Understanding dynamic friction through spontaneously evolving laboratory earthquakes.* Nature Communications, 2017. **8**: p. 15991.

113. Forsberg, F. and C.R. Siviour, *3D deformation and strain analysis in compacted sugar using x-ray microtomography and digital volume correlation.* Measurement Science and Technology, 2009. **20**(9): p. 095703.

114. Hong, S.Y., et al., *Experimental investigation of mechanical properties of UV-Curable 3D printing materials.* Polymer, 2018. **145**: p. 88-94.

115. Arruda, E.M. and M.C. Boyce, *A three-dimensional constitutive model for the large stretch behavior of rubber elastic materials.* Journal of the Mechanics and Physics of Solids, 1993. **41**(2): p. 389-412.

116. Zhang, P. and A.C. To, *Transversely isotropic hyperelastic-viscoplastic model for glassy polymers with application to additive manufactured photopolymers.* International Journal of Plasticity, 2016. **80**: p. 56-74.

117. Sutton, M.A., J.J. Orteu, and H. Schreier, *Image correlation for shape, motion and deformation measurements: basic concepts, theory and applications*. 2009: Springer Science & Business Media.

118. Wagner, K.B., et al., *High-speed X-ray Phase Contrast Imaging and Digital Image Correlation Analysis of Microscale Shock Response of an Additively Manufactured Energetic Material Simulant.* Journal of Applied Physics, 2020. **127**.

119. Qu, J. and M. Cherkaoui, *Bounds for Effective Moduli*, in *Fundamentals of Micromechanics of Solids*. 2006. p. 120-153.

120. Keyhani, A. and M. Zhou, *Thermo-Mechanical Response of an Additively Manufactured Energetic Material Simulant to Dynamic Loading.* Submitted for publication, 2020.

121. Drucker, D., *Plasticity theory strength-differential (SD) phenomenon, and volume expansion in metals and plastics.* Metallurgical Transactions, 1973. **4**(3): p. 667.

122. Seltzer, R., et al., *Determination of the Drucker–Prager parameters of polymers exhibiting pressure-sensitive plastic behaviour by depth-sensing indentation.* International Journal of Mechanical Sciences, 2011. **53**(6): p. 471-478.

123. Hooputra, H., et al., *A comprehensive failure model for crashworthiness simulation of aluminium extrusions.* International Journal of Crashworthiness, 2004. **9**(5): p. 449-463.

124. Pijaudier-Cabot, G. and Z.P. Bazant, *Nonlocal Damage Theory.* Journal of Engineering Mechanics, 1987. **113**(10): p. 1512-1533.

125. Comi, C., *A non-local model with tension and compression damage mechanisms.* European Journal of Mechanics a-Solids, 2001. **20**(1): p. 1-22.

126. Taylor, R.L., P.J. Beresford, and E.L. Wilson, *A non-conforming element for stress analysis.* International Journal for numerical methods in Engineering, 1976. **10**(6): p. 1211-1219.

127. Jensen, B., et al., *Ultrafast, high resolution, phase contrast imaging of impact response with synchrotron radiation.* AIP Advances, 2012. **2**(1): p. 012170.

128. Jensen, B., et al., *Impact system for ultrafast synchrotron experiments.* Review of Scientific Instruments, 2013. **84**(1): p. 013904.

129. Mayo, S.C., A.W. Stevenson, and S.W. Wilkins, *In-Line Phase-Contrast X-ray Imaging and Tomography for Materials Science.* Materials, 2012. **5**(5): p. 937-965.

130. Stevenson, A., et al., *Phase-contrast X-ray imaging with synchrotron radiation for materials science applications.* Nuclear Instruments and Methods in Physics Research B, 2003. **199**: p. 427-435.

131. Wilkins, S., et al., *Phase-contrast imaging using polychromatic hard X-rays.* Nature, 1996. **384**(6607): p. 335.

132. Crum, R., et al., *In situ X-ray imaging of heterogeneity in dynamic compaction of granular media.* Journal of Applied Physics, 2019. **125**(2): p. 025902.

133. Parab, N., et al., *High speed X-ray phase contrast imaging of energetic composites under dynamic compression.* Applied Physics Letters, 2016. **109**(13): p. 131903.

134. Mares, J., et al., *In-situ X-ray observations of ultrasound-induced explosive decomposition.* Applied Materials Today, 2019. **15**: p. 286-294.

135. Branch, B., et al., *Controlling shockwave dynamics using architecture in periodic porous materials.* Journal of Applied Physics, 2017. **121**(13): p. 135102.

136. Pan, B., et al., *Two-dimensional digital image correlation for in-plane displacement and strain measurement: a review.* Measurement science and technology, 2009. **20**(6): p. 062001.

137. Huang, J.Y., et al., *Origin of compression-induced failure in brittle solids under shock loading.* Physical Review B, 2015. **92**(14): p. 144101.

138. Ravindran, S., et al., *Weak-shock wave propagation in polymer-based particulate composites.* Journal of Applied Physics, 2019. **125**(14): p. 145104.

139. Proud, W.G., et al., *Diagnostic techniques in deflagration and detonation studies.* Chemistry Central Journal, 2015. **9**(1): p. 52.

140. Lu, L., et al., *Note: dynamic strain field mapping with synchrotron X-ray digital image correlation.* Review of Scientific Instruments, 2014. **85**(7): p. 076101.

141. Jensen, B., et al., *Examining Material Response Using X-Ray Phase Contrast Imaging*, in *2018 Annual Conference on Experimental and Applied Mechanics*, J. Kimberley, L.E. Lamberson, and S. Mates, Editors. 2019. p. 89-93.

142. Bay, H., et al., *Speeded-up robust features (SURF).* Computer vision and image understanding, 2008. **110**(3): p. 346-359.

143. Malvern, L.E., *Introduction to the mechanics of a continuous medium*. 1969: Prentice-Hall.

144. Parab, N., et al., *Fracture mechanisms of glass particles under dynamic compression.* International Journal of Impact Engineering, 2017. **106**: p. 146-154.